

DEVELOPMENT, FABRICATION AND CHARACTERIZATION OF GRAPHENE
AND BISMUTH HALL SENSORS FOR SCANNING HALL PROBE MICROSCOPY

by

SELDA SONUŞEN

Submitted to the Graduate School of Engineering and Natural Sciences

in partial fulfillment of

the requirements for the degree of

Doctor of Philosophy

Sabanci University

January 2015

DEVELOPMENT, FABRICATION AND CHARACTERIZATION OF GRAPHENE
AND BISMUTH HALL SENSORS FOR SCANNING HALL PROBE MICROSCOPY

APPROVED BY:

Prof. Dr. Ahmet Oral
(Dissertation Supervisor)

Prof. Dr. Yuda Yürüm

Assoc. Prof. Dr İnanç Adagideli

Assoc. Prof. Dr Selmiye Alkan Gürsel

Assoc. Prof. Dr Özgür Özer

DATE OF APPROVAL:

© Selda Sonuŝen 2015
All Rights Reserved

DEVELOPMENT, FABRICATION AND CHARACTERIZATION OF GRAPHENE
AND BISMUTH HALL SENSORS FOR SCANNING HALL PROBE MICROSCOPY

Selda Sonuŝen

Physics, PhD Thesis, 2015

Thesis Supervisor: Prof. Ahmet Oral

Keywords: Graphene Hall Sensor, Bismuth Hall Sensor, Scanning Hall Probe
Microscopy (SHPM), Quartz Tuning Fork (QTF), Graphene Growth by Chemically
Vapor Deposition (CVD), Magnetic Imaging

ABSTRACT

Scanning Hall Probe Microscopy (SHPM) is a powerful magnetic imaging technique which provides high magnetic field and spatial resolution, simultaneously with the topography of magnetic and superconducting materials. It is a quantitative method which can be operated under high magnetic fields and a wide temperature range. The Hall sensor which is sensitive to the perpendicular component of the magnetic field emanating from the specimen determines resolution. In this work, single layer Graphene Hall Probes (GHP) were fabricated using Chemical Vapor Deposition (CVD) grown graphene on copper foils, transferred to Silicon wafers. The Hall coefficient and field sensitivity of GHPs were measured to be $0.18 \Omega/\text{G}$ and $0.20 \text{ G}/\sqrt{\text{Hz}}$, respectively, for a $3 \mu\text{A}$ drive current at room temperature. For the first time, GHP is successfully used for magnetic imaging in 3–300 K range in SHPM with quartz crystal Atomic Force Microscopy (AFM) feedback. This study has demonstrated that graphene is an alternative material to be used for magnetic imaging in SHPM. Alternatively, Bismuth based Hall probes are also fabricated by advanced lithographic techniques. Since Bismuth is a semimetal with low carrier concentration, it has been considered as a promising Hall sensor material. For the first time, SHPM images of NdFeB demagnetized magnet were acquired using Bi hall sensor fabricated by Electron Beam Lithography (EBL) with quartz crystal AFM feedback.

TARAMALI HALL AYGITI MİKROSKOPLARI İÇİN GRAFEN VE BİZMUT
HALL ALGILAYICI GELİŞTİRİLMESİ, ÜRETİMİ VE KARAKTERİZASYONU

Selda Sonuşen

Fizik, Doktora Tezi, 2015

Tez Danışmanı: Prof. Dr. Ahmet Oral

Anahtar Kelimeler: Grafen Hall Aygıtı, Bizmut Hall Aygıtı, Taramalı Hall Aygıtı
Mikroskobu, Kuvartz Kristal Çatal, Kimyasal Buhar Biriktirme Yöntemi ile Grafen
Üretimi,

ÖZET

Taramalı Hall Aygıtı Mikroskobu (THAM) manyetik ve süperiletken malzemelerin yüksek manyetik ve uzaysal çözünürlükle çalışan bir görüntüleme tekniğidir. THAM yüksek manyetik alan altında ve geniş sıcaklık aralığında da çalıştırılabilen nitel bir metoddur. İncelenen numuneden gelen manyetik alanın dik bileşenine hassas olan Hall aygıtı, çözünürlüğü ve hassasiyeti belirler. Bu çalışmada, kimyasal buhar biriktirme yöntemi ile elde edilen tek tabakalı grafenden üretilen, Grafen Hall aygıtının oda sıcaklığında ve 3 μ A akım değeri için, Hall katsayısı ve alan hassasiyeti sırası ile 0.18 Ω /G and 0.20 G/ \sqrt Hz olarak ölçüldü. Grafen Hall aygıtı dünyada ilk kez 3–300 K sıcaklık aralığında manyetik görüntüleme, kuvars kristalli Atomik Kuvvet Mikroskobu (AKM) geribeslemesi ile çalışan THAM ile başarılı olarak kullanıldı ve de-manyetize edilmiş NdFeB mıknatısın görüntüleri elde edildi. Bu çalışma, grafenin THAM da kullanılmak üzere alternatif bir malzeme olduğunu gösterdi. Eş zamanlı olarak, bizmut Hall aygıtı ileri litografi teknikleri kullanılarak üretildi. Bizmut düşük taşıyıcı yoğunluğuna sahip bir yarımetal olduğu için bizmut da gelecek vaat eden hall aygıtı malzemesi olarak değerlendirilir. Elektron demeti lithografisi ile üretilmiş Bizmut Hall aygıtı ilk kez THAM da de-manyetize edilmiş NdFeB mıknatısın görüntülenmesinde kullanıldı.

To Ayten Sonuŝen and Hasan Sonuŝen

ACKNOWLEDGEMENTS

First of all, I would like to extend my deepest gratitude to my thesis supervisor and greatest mentor to Prof. Dr. Ahmet Oral for his unfailing support throughout my Ph.D studies. This thesis would not have been possible without his outstanding supervision.

I would like to thank to Prof. Dr. Yuda Yürüm, Assoc. Prof. Dr İnanç Adagideli, Assoc. Prof. Dr Selmiye Alkan Gürsel, and Assoc. Prof. Dr Özgür Özer for being on my thesis committee.

I am indebted to Asst. Prof Dr. Seda Aksoy for helping me with the fabrication and characterization of graphene Hall sensor. I am deeply grateful to Özgür Karcı and Dr. Münir Dede for sharing their experience with me and for generating the magnetic imaging in SHPM. I would like to thank to the entire staff of NanoMagnetics Instruments Ltd. for their support during my training in this company. I am also thankful to Assoc. Prof. Dr Hidayet Çetin sharing his experience on graphene.

I am grateful to Dr. Anıl Günay Demirkol , the ultimate polymath, both for her friendship and mentorship. I am thankful to Cenk Yanık for making life easier, bearable, and enjoyable for me all the time. I would also like to thank to Süleyman Çelik for his rare competence in performing fine work. Hasan Özkaya and Dr. Sibel Kasapare to be mentioned for their great support. I would like to acknowledge my previous and current group members, Derya Gemici, Nihan Özkan Aytekin, Dr. Musa Mutlu Can, Hüsnü Aslan, Dr. Shumaila Karamat, Yiğit Uysallı, and Ekin Özgönül.

My greatest thanks go to my friends at Sabancı University, especially to Naime Kınalı, Senem Avaz, Bahriye Karakaş, Utku Seven, Raghu Sharma Mokkapati, Ezgi Uzun, Ines Karmous and Damla Arifoğlu for their all unforgettable support during my thesis writing process. I would not have been able to finalize this thesis without their constant encouragement. I would like also like to thank to my dear friends, Billur, Umut, Emre, Nurdan, and Gülhis for their friendship.

Finally; no word describes my deepest feelings to my dad, Hasan Sonuŝen, and my mom, Ayten Sonuŝen. If there were a hundred million words to describe my feelings to them in my native language, I would not cease to use these words of indebtedness to them every single day. My sister; Seda Ibas, the other half of my soul, and Doruk Ibas, the bringer of luck, happiness and the joy for all of us, are at the top of my gratitude list. I am also thankful to Arda Ibas for being a part of our family.

TABLE OF CONTENTS

1	INTRODUCTION	1
1.1	Context and Motivation	1
1.2	Structure of the Thesis	3
2	SCANNING PROBE MICROSCOPY AND MAGNETIC IMAGING	5
2.1	Scanning Probe Microscopy	5
2.1.1	Scanning Tunneling Microscopy	5
2.1.2	Atomic Force Microscopy.....	7
2.1.3	Magnetic Imaging techniques	8
2.1.3.1	Magnetic Force Microscopy.....	8
2.1.3.2	Scanning Hall Probe Microscopy.....	9
3	SCANNING HALL PROBE MICROSCOPY	13
3.1	Introduction.....	13
3.2	Scanning Hall Probe Microscopy	15
3.2.1	The Microscope Design and Operation.....	15
3.2.2	LT-SHPM Electronics	22
3.2.3	LT-SHPM Software.....	23
3.3	Scan Modes of LT-SHPM.....	23
3.3.1	Lift-off Mode.....	23
3.3.2	Real Time Mode.....	24
3.3.3	AFM/STM tracking mode.....	25
3.4	Quartz Tuning Fork Force Sensor for AFM Tracking Mode in SHPM....	29
4	FABRICATION OF THE HALL SENSOR AND CONVENTIONAL FABRICATION METHODS	37
4.1	Introduction.....	37
4.2	Nanofabrication Techniques	38
4.2.1	Substrate Preparation.....	38
4.2.2	Optical lithography.....	39
4.2.3	Electron Beam Lithography	44

4.2.4 Etching Process	55
4.2.4.1 Wet Etching	55
4.2.4.2 Dry etching	58
4.2.5 Thermal Evaporation.....	62
4.2.6 Dicing and Wire Bonding	63
5 GRAPHENE HALL SENSORS for SHPM	65
5.1 Introduction	65
5.2 Mechanic and Electronic Properties of Graphene	67
5.3 Graphene Fabrication Methods	68
5.4 Characterization Methods of Graphene	71
5.5 Graphene Hall sensor	73
5.5.1 Fabrication of GHP	74
5.5.2 Characterization of GHP	78
5.5.3 Imaging NdFeB Demagnetized Magnet by GHP.....	83
5.6 Conclusion and Discussion	85
6 BISMUTH HALL SENSORS for SHPM.....	88
6.1 Introduction	88
6.2 Bismuth Hall sensor	90
6.2.1 Fabrication of Bismuth Hall sensor.....	90
6.2.2 Characterization of Bismuth Hall Sensor.....	94
6.2.3 Imaging NdFeB Demagnetized Magnet by Bismuth Hall Sensor .	96
6.3 Conclusion.....	99
7 CONCLUSION AND FUTURE WORK	100
8 BIBLIOGRAPHY	102

LIST OF FIGURES

Figure 1.1:	Schematic layout of the Scanning Probe Microscope.....	2
Figure 2.1:	The principle of Scanning Tunneling Microscopy.....	6
Figure 2.2:	STM topographic image of Si (111) under ultra high vacuum.	7
Figure 2.3:	Force as a function of distance between tip and sample	8
Figure 2.4:	Hall effect.....	9
Figure 2.5:	Schematic layout of the Scanning Hall Probe Microscope.....	12
Figure 3.1:	Comparison of magnetic field sensitivity and spatial resolution of the different imaging techniques.....	14
Figure 3.2:	Photograph of LT-SHPM used in the experiments	15
Figure 3.3:	Detailed photograph of LT-SHPM.....	16
Figure 3.4:	V_{Hall} Out vs Time graph of a 500 nm Bismuth Hall probe for $-10 \mu A$ Hall current.....	17
Figure 3.5:	(a) The illustration shows the Hall sensor and the sample mounted on the slider puck while alignment process is carried out under optical microscope (b) and tilted Hall sensor with respect to the sample surface from different views	19
Figure 3.6:	Photograph of scanner and slider piezos in SHPM.....	21
Figure 3.7:	SHPM images of Bismuth substituted iron garnet thin film taken by using real time scanning mode. Values above images represent applied perpendicular magnetic field to bismuth substituted iron garnet thin film.	25
Figure 3.8:	Optical microscope image of the Hall sensor designed and fabricated for STM tracking mode.....	26
Figure 3.9:	(a) SEM images of the Hall sensor integrated AFM tip apex for different magnifications. (b) High magnification SEM image of Hall cross located at the end of the silicon cantilever (c) and (d) topography and magnetic image of 40 MB computer hard disk respectively.	28
Figure 3.10:	(a) The schematic illustrates top and side view of the cantilever which consists of two sensors for both topography and magnetic imaging. (b) SEM image of the fabricated sensor. Surface topography (c) and SHPM image of array of NiFe rectangles.	28

Figure 3.11:	AFM image of Si (111) under ultra high vacuum by using a sharp tip attached to QTF.....	30
Figure 3.12:	The pictures show process steps of fabrication of Hall sensor for AFM tracking mode by using QTF. (a) Before (top) and after (bottom) QTF is removed from its metal can. (b) The picture of PCB used throughout measurements during this study. (c) and (d) pictures of QTF which is glued on the top of PCB and Hall sensor attached to QTF respectively. (e) Dedicatedly designed boxes for Hall sensor storage.	32
Figure 3.13:	Picture of dialog box in SPM software for central frequency, quality factor and maximum phase calculation.....	34
Figure 3.14:	Resonance curve of QTF before (a) and (b) after Hall sensor attached to QTF in ambient condition respectively.....	35
Figure 3.15:	Resonance frequency curve of QTF attached GaN Hall sensor for one prong free and both prongs free situations and for two different sizes of quartz tubes.	36
Figure 4.1:	The entire mask design which is used for Hall sensor fabrication.....	40
Figure 4.2:	Process flow of the photolithography for both negative and positive resist	41
Figure 4.3:	Process flow of the photolithography for both negative and positive resist	42
Figure 4.4:	Process flow of the EBL for both negative and positive resist tone.	47
Figure 4.5:	Schematic illustration of fabrication steps for bilayer system.	48
Figure 4.6:	(a) Screenshot of Hall sensor array designed in DesignCAD program. (b) SEM image of hall sensor patterns after lift-off process.....	50
Figure 4.7:	(a) SEM image of hall sensor patterns arrayed by Run File Editor (b) after lift-off process.	51
Figure 4.8:	(a) Screenshot of 100 nm Hall sensor designed in DesignCAD program (b) SEM image of fabricated 100nm Hall sensor pattern.	51
Figure 4.9:	(a) The optical microscope image of 50 nm Hall sensor after development (b) Simulation of Hall cross pattern after implemented by PEC.....	53
Figure 4.10:	(a) and (b) the SEM images of 50 nm Hall sensor at different magnifications after 5nm Cr/30 nm Au evaporation and lift-off in acetone.....	54

Figure 4.11:	The SEM image of 21 nm sized Hall cross by using 950 K PMMA–C2.	54
Figure 4.12:	(a), (b) The optical microscope and (c), (d) the SEM images of recess formation.	57
Figure 4.13:	SEM image of mesa formation on Bismuth Hall sensor.	58
Figure 4.14:	(a) and (b) SEM image of Bismuth Hall sensor without and with oxygen plasma application before e–beam resist coating respectively.	59
Figure 4.15:	The optical microscope image of GHP after mesa formation.	60
Figure 4.16:	The SEM images of Bismuth Hall sensor after mesa formation.	61
Figure 4.17:	The SEM images of 50 nm Bismuth Hall sensor (a) with and (b) without evaporation of Cr as adhesion layer before Bismuth metal.	63
Figure 4.18:	Diced Bismuth Hall sensor fabricated on GaAs substrate.	64
Figure 4.19:	The SEM image of diced and bonded Bismuth Hall sensor.	64
Figure 5.1:	The energy dispersion of graphene and the Dirac cone.	68
Figure 5.2:	(a), (b) and (c) Graphene fabrication steps and (d) single and multi layer graphene sheets produced by this method.	69
Figure 5.3:	Calculated optical contrast variation of graphene with changes in SiO ₂ thickness and of wavelength of light.	71
Figure 5.4:	(a) Optical microscope image of graphene sheets produced via mechanical exfoliation method. Raman spectrum of (b) single and (c) multi layer graphene film. (d) AFM topography of single layer graphene sheet.	73
Figure 5.5:	The optical microscope images of (a) mechanical exfoliated graphene (b) after contact pad metallization, (c) O ₂ plasma etching of graphene (d) taking contact from graphene to contact pads by implementing EBL and (e) mesa step formation	75
Figure 5.6:	The optical microscope images of after (a) Hall cross definition by implementing positive photolithography and (b) after O ₂ plasma process and removing photoresist	76
Figure 5.7:	The optical microscope images (a) of the developed sample with AZ726MIF after positive photolithography by using recess mask pattern (b) after contact pads metallization	77

Figure 5.8:	Optical microscope images of GHP. (a) After mesa formation by etching 830 nm SiO ₂ /Si layer. (b) Side view of Hall sensor glued on 1 × 1 cm PCB	77
Figure 5.9:	(a) The optical microscope images of as received CVD growth graphene on 285 nm SiO ₂ /Si wafers. (b) The Raman spectrum of as received CVD growth graphene from different three points.....	78
Figure 5.10:	Optical microscope image of GHP (left).Raman map of ($I_{2D}/I_G \geq 2$) intensity ratio measured in a 14 μm × 14 μm area of GHP (right–top). Single Raman spectrum taken from center of the GHP (right–bottom)..	79
Figure 5.11:	Hall voltage response of GHP to applied magnetic field at room temperature.....	80
Figure 5.12:	(a) B_{min} for different drive current as a function of frequency at 300 K. (b) B_{min} for different temperature as a function of frequency for 5 μA Hall current.....	81
Figure 5.13:	Comparison of B_{min} in vacuum and in Helium exchange gas for different current values. (d) Serial resistance of two arms of Hall crosses as a function of temperature	82
Figure 5.14:	The variations of R_{Hall} as a function of temperature for ± 2 μA driving current.....	83
Figure 5.15:	Measured resonance frequency at 300 K (a) before and (b) after GHP was glued on QTF.	83
Figure 5.16:	(a) and (c) magnetic images of NdFeB demagnetized magnet by using GHP at 300 K. (b) and (d) magnetic field variations along the line drawn on images	84
Figure 5.17:	(a) Topographic image of NdFeB. (b) 50 μm × 50μm LT–SHPM magnetic image of NdFeB at 126 K. 14 μm × 14 μm LT–SHPM magnetic image of the same sample for (c) $I_{Hall} = +2 \mu A$ (d) $I_{Hall} = -2 \mu A$ at 3 K.....	85
Figure 5.18:	SEM image of as received CVD graphene sheet which shows cracks and discontinuity on the graphene film surface	86
Figure 6.1:	The SEM images of 50 nm × 50 nm nano-Bismuth hall probe. SHPM image of crystalline Bismuth substituted iron garnet thin film taken by fabricated 50 nm Bismuth Hall sensor at room temperature.....	89
Figure 6.2:	The optical microscope image of (a) symmetric (b) asymmetric ohmic contacts after 10 nm Cr and 100 nm Au evaporation and lift–off process	90
Figure 6.3:	Then SEM images of 50 nm Bismuth Hall cross at different magnifications	92

Figure 6.4:	(a)The optical microscope images after the first time EBL is employed for connection problem (b), (c) and (d) show SEM images after third EBL process applied at different magnifications and different points of view	93
Figure 6.5:	The SEM images of 50 nm Bismuth Hall sensor after mesa formation.....	94
Figure 6.6:	(a) The SEM image of 500 nm Bismuth Hall sensor. B_{\min} as a function of driving current at different temperature values (b) 300 K (c) 77 K and (d) 4 K The SEM images of 50 nm Bismuth Hall sensor after mesa formation	95
Figure 6.7:	(a) The SEM image of 200 nm Bismuth Hall sensor B_{\min} a function of driving current at different temperature values (b) 300 K (c) 77 K and (d) 4 K.....	95
Figure 6.8:	SHPM images of NdFeB demagnetized magnet at (a) 300 K, (b) 77 K, (c) 4 K taken by using 500nm Bismuth Hall sensor for 50 μ A driving current and at (d) 4 K for -50μ A driving current.	96
Figure 6.9:	SHPM images of NdFeB demagnetized magnet at 300 K (left) by using 200 nm Bismuth Hall sensor for 500 μ A drive current and graph of cross sections (right top and bottom).	97
Figure 6.10:	(a) Topography and (b) SHPM image of NdFeB sample at 77 K by using 200 nm Bismuth Hall sensor for 500 μ A drive current.....	97
Figure 6.11:	(a) Topography and (b) SHPM image of NdFeB sample at 4 K by using 200 nm Bismuth Hall sensor for 500 μ A drive current.....	98
Figure 6.12:	(a) SHPM image of NdFeB sample at 300 K by using 100 nm Bismuth Hall sensor for 500 μ A drive current. (b) Magnetic field variations along the line drawn on images.....	99

LIST OF TABLES

Table 4.1:	Summary of the positive lithography process parameters optimized for two different mask aligner systems are given	43
Table 4.2:	Summary of image reversal process parameters optimized for two different mask aligner systems are given	43
Table 5.1:	Summary of data measured from InSb, epitaxial graphene and CVD graphene sensor for 5 μm Hall cross size.....	66

LIST OF ABBREVIATIONS

MO	: Magneto Optics
QTF	: Quartz Tuning Fork
ADC	: Analog to Digital Converter
VTI	: Variable Temperature Insert
PCB	: Printed Circuit Board
CBT	: Cantilever Beam Theory
SHM	: Simple Harmonic Motion
EBL	: Electron Beam Lithography
CD	: Critical Dimension
ACE	: Acetone
IPA	: Isopropyl Alcohol
DI	: Deionized
PAC	: Photoactive Compound
UV	: Ultraviolet
SEM	: Scanning Electron Microscopy
PMMA	: Polymethyl Methacrylate
HSQ	: Hydrogen Silsesqioxane
Fox 12	: Flowable Oxide
MIBK	: Methyl Isobutyl Ketone
NPGS	: Navity Pattern Generation System
EHT	: Extra High Tension
PEC	: Proximity Effect Correction
PSF	: Point Spread Function
RIE	: Reactive Ion Etching

GHP	: Graphene Hall Probe
SHPM	: Scanning Hall Probe Microscopy
SPM	: Scanning Probe Microscope
LT-SHPM	: Low Temperature Scanning Hall Probe Microscopy
FET	: Field Effect Transistor
LEED	: Low-Energy Electron Diffraction
TEM	: Transmission Electron Microscope
ICP-RIE	: Inductively Coupled Plasma Reactive Ion Etching

CHAPTER 1

INTRODUCTION

1.1 Context and Motivation

The development of Scanning Probe Microscopy (SPM), which can achieve atomic scale resolution, has been pioneered by the invention of Scanning Tunnelling Microscopy (STM) in 1981 by Binnig & Rohrer ¹. In STM we use an atomically sharp tip which is kept at very close proximity of the surface by regulating the distance to keep a constant tunnel current, in the nA range. The image is formed by scanning the tip across the surface by means of piezoelectric scanners, as we record the tip height as shown in Figure x. The basic working principle of all members of SPM family is similar to each other. In short we scan a probe at close proximity of the specimen surface, while we measure the interaction between the tip and sample: this interaction can be chemical force, magnetic force, electric current etc. One can obtain information on various properties of samples like surface morphology, topography, magnetic properties etc, by utilizing different interaction modes between the sample and the tip. The Scanning Hall Probe Microscopy (SHPM) uses a micro or nano Hall sensor to image the z-component of local magnetic flux density, \mathbf{B}_z , down to 50nm resolution. The main content of this thesis covers development of new graphene and Bismuth micro and nano Hall sensors for SHPM.

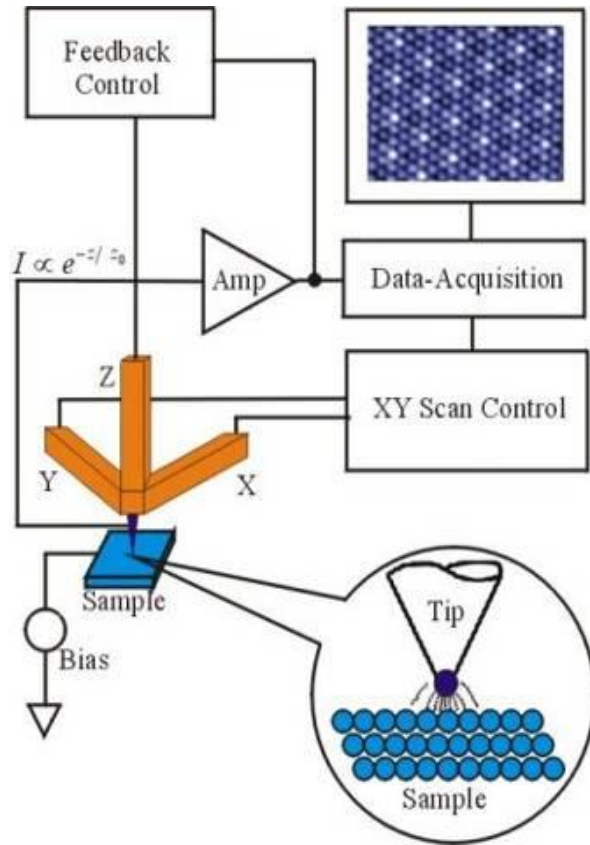


Figure 1.1: Schematic layout of the Scanning Probe Microscope.

The basic operating principle of SHPM is to provide information on magnetic properties of materials by measuring classical Hall effect. The resolution of SHPM is determined by the Hall sensor which is manufactured using advanced microfabrication techniques. Based on the necessities, the probe of the Hall sensor can be fabricated at different sizes, from different materials. In order to increase the magnetic field resolution, high mobility materials with low charge carrier concentrations are preferred². Moreover, the spatial resolution of the microscope is defined by the physical dimensions the Hall sensor³. Various materials have been utilized for the fabrication of Hall sensors for different applications and temperatures, so far such as InSb, GaAs/AlGaAs, Silicon-on Insulator, AlGaN/GaN etc^{4,5}. In addition to these materials, the experimental isolation of graphene made it a new candidate for fabricating high sensitivity Hall sensors. Graphene is a promising material thanks to its extraordinary mechanical and electrical properties⁶. In literature it has been indicated that minimum detectable magnetic field of epitaxial-grown graphene is better than InSb Hall sensor; which has been shown as a low noise and high

performance Hall probe at room temperatures⁷. This fact shaped the motivation of this thesis; to use graphene as Hall sensor material for magnetic imaging and also increase magnetic field resolution and hopefully decrease the size for smaller than 50 nm spatial resolution. In addition to graphene, bismuth is also an alternative material for SHPM application thanks to its low charge carrier concentration. Bismuth Hall sensor fabricated by using focused ion beam (FIB) system is damaged by Ga⁺ and this results in having hall sensor with poor performance^{8,9}. It is reported that minimum detectable magnetic field of Bismuth Hall sensor is improved further by implementing electron beam lithography in the fabrication process¹⁰. In this thesis work, we also attempted to reduce the Bismuth Hall sensor area, in order to obtain higher spatial resolution and implement electron beam lithography (EBL) in order to prevent damage arising from FIB technique.

1.2 Structure of the Thesis

In Chapter 1, motivations of this study are underlined. Chapter 2 presents a general introduction about scanning probe microscopy and provides detailed information on both theoretical aspects and working principles of different types of SPM, such as Atomic Force Microscopy (AFM), STM, Magnetic Force Microscopy(MFM) and SHPM. In particular, this chapter addresses the well-known phenomena called as classical Hall effect and its utilization in SHPM applications.

Chapter 3 covers the basic principles of SHPM and its components, microscope design, electronics, operation principles and explain the types of scanning modes that we used. Among the scanning modes, extra effort was spent to explain the quartz tuning fork AFM tracking mode.

In Chapter 4, we mainly discuss fabrication of Hall probes which is the most crucial part that determines the resolution of SHPM. Fabrication techniques used for Hall sensor production, problems encountered during fabrication process and their solutions are presented with using SEM and optical microscope images.

In Chapter 5 and Chapter 6 present fabrication, characterization, and magnetic imaging of NdFeB demagnetized magnet by using Graphene Hall sensor and Bismuth Hall sensor respectively. In chapter 7, we discussed our results and future work.

CHAPTER 2

SCANNING PROBE MICROSCOPY AND MAGNETIC IMAGING

2.1 Scanning Probe Microscopy

Scanning probe microscopy (SPM) is a commonly used imaging technique which provides local properties of an investigated sample surface down to atomic scale. Most SPMs use an extremely sharp tip which is brought into close proximity of a sample in order to measure interaction between tip and sample. These interactions are used as a feedback signal and define type of SPM. Sample is typically scanned by piezoelectric crystals; which also controls tip–sample distance with high precision. There are various types of SPM. In the following sections, first STM and AFM will be presented and then, working principle of the most prominent magnetic imaging techniques and SHPM will be covered.

2.1.1 Scanning Tunneling Microscopy

SPM has provided scientists to characterize surface of a sample at atomic scale. Before the 1980's, it was not possible to image of a material in the atomic scale. However, in 1981 Gerd Binnig and Heinrich Rohrer invented STM, which could image single atoms, at IBM Laboratories in Switzerland ¹. This invention brought Nobel Prize in 1986 to its inventors and contributed to the development of SPM.

In STM, sharp conductive tip, having a single atom at its closest point of surface, is brought into close proximity with the conductive sample surface. Although tip and sample are very close to each other, they are not in physical contact. When a voltage is

applied between tip and sample, electrons start tunneling from sample to tip or the other way around depending on the polarity of voltage; which determine the direction of tunneling current. Electron tunneling is at the heart of STM which is one of the fundamental phenomena in quantum mechanics. In classical physics, it is not possible for a particle to penetrate a potential barrier if the total energy of the particle is less than the barrier height. However, in quantum mechanics, this particle can go through the potential barrier and this is known as quantum mechanical tunneling¹¹. The tunneling current is an exponential function of distance and it is given by

$$I_{\text{Tunneling}} \propto \frac{V_{\text{Bias}}}{z} e^{-2kz} . \quad (2.1)$$

$$k = \sqrt{2m\phi}/\hbar . \quad (2.2)$$

where m is the electron mass, ϕ is the average work function of the tip and sample, \hbar is the Planck's constant, V_{Bias} is the applied bias voltage between tip and specimen and z is the tip-sample distance (Figure 2.1)^{12, 13}.

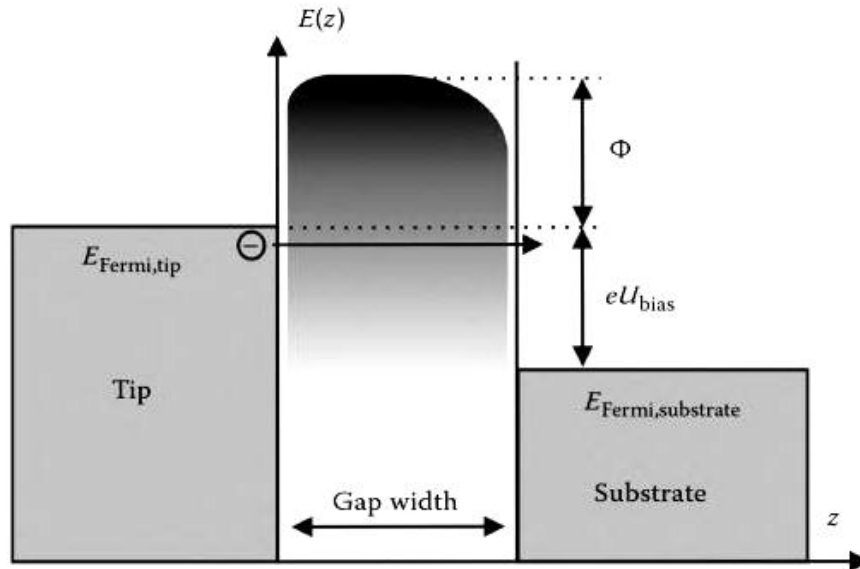


Figure 2.1: The principle of Scanning Tunneling Microscopy¹³.

Distance between tip and sample can be controlled by measuring tunneling current and if tunneling current is fed to a control circuit, it enables to obtain topographical image of a conductive sample with atomic resolution.

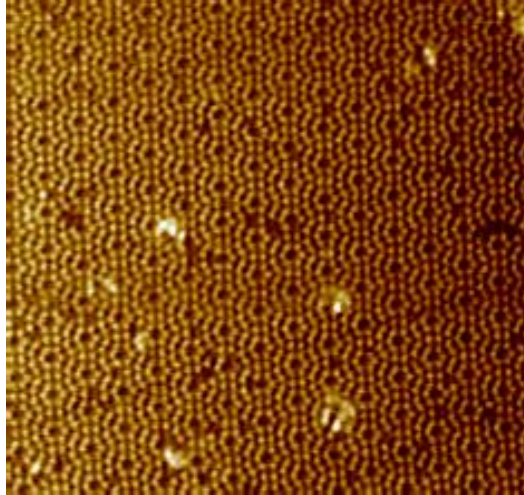


Figure 2.2: STM topographic image of Si (111) under ultra high vacuum.

2.1.2 Atomic Force Microscopy

Even though STM provides high resolution imaging, it only allows us to examine conductive samples. AFM was developed by Binnig et al in 1986¹⁴ to overcome this drawback. One of the most important advantages of AFM is that it enables to analyze insulator samples as well as conductive materials .

AFM is sensitive to interaction between an extremely sharp tip at the end of the micro-fabricated AFM cantilever and the atoms located on the sample surface. There are basically two types of tip-sample interactions known as attractive and repulsive forces. van der Waals interaction, chemical force, capillary and electrostatic forces are considered as attractive forces while repulsive forces are hard sphere repulsion, Pauli exclusion interaction and electron-electron Coulomb interaction¹⁵. Force as a function of distance between the tip and sample is shown in Figure 2.3¹⁶. As is seen from the figure, when tip approaches toward the sample, first of all, attractive forces are dominated. At large distance, main component of attractive forces is the van der Waals interactions. These forces result from fluctuations in electric dipoles of atoms and molecules¹⁷.

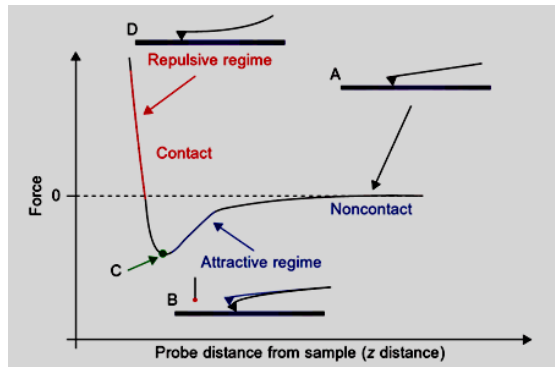


Figure 2.3: Force as a function of distance between tip and sample ¹⁶.

When the surface topography of sample changes, interatomic forces between tip and the sample surface also differ and thus result in cantilever deflection. By monitoring the deflection of cantilever with optical detection system, topographic images of both conductive and nonconductive samples are obtained.

2.1.3 Magnetic Imaging Techniques

2.1.3.1 Magnetic Force Microscopy

Different than Atomic force microscopy, Magnetic force microscope (MFM) uses a sharp magnetic tip to scan a sample with magnetic domains and provides information regarding its magnetic structure. Attractive or repulsive magnetic forces between the sample and magnetic tip attached to a flexible microcantilever are measured to obtain magnetic domains on the specimen. The basic principles of MFM to obtain an image are as follows:

- Magnetic tip is first used in tapping mode to map the topography of sample's surface.
- Surface is tracked from a certain distance above the surface in lift mode.
- Image is produced by the interactions between sample's surface magnetic field and magnetic AFM tip.

MFM measures the vertical gradient of magnetic force that is established between magnetic tip and the sample surface. Derivative of the vertical component can either be measured by slope or modulations in frequency. Sensitivity of MFM therefore mainly depends on minimum detectable force gradient ¹⁸.

Although MFM's resolution is dependent on various factors, among them the most important ones are perhaps the tip size & geometry and sample tip spacing. Today's MFM devices are capable to resolve magnetic features up to 10–50 nm depending on the environmental conditions ¹⁹. However, the demand for improved MFM resolutions is still attracting researchers to be able to resolve smaller features. For instance, Han *et al.* Fabricated a dual–synthetic MFM tip to improve spatial resolution and compared the images with those obtained by conventional MESP tip and confirmed superior performance of dual–synthetic tips. The samples were scanned on a 10 μm \times 10 μm area under ambient conditions in tapping/lift mode ²⁰.

2.1.3.2 Scanning Hall Probe Microscopy

Scanning Hall Probe Microscopy (SHPM) is based on Hall effect principle which was discovered by Edwin Herbert Hall in 1879. He has found that if a current carrying conductor or semiconductor is placed in a magnetic field at right angles, a voltage is created in the perpendicular direction to both to direction of current and the magnetic field. In Hall Effect, as shown in Figure 2.4, a semiconductor material with dimension $\ell \times w \times d$ is subjected to an electric current in the positive x direction.

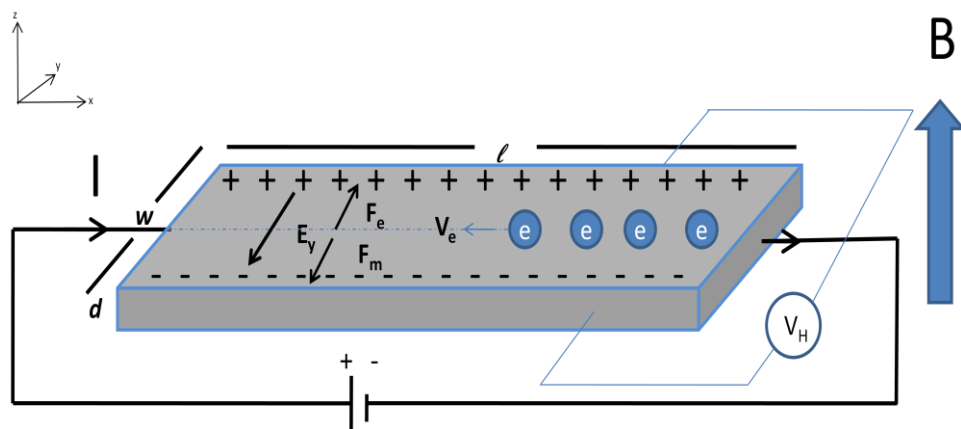


Figure 2.4: Hall effect.

If a material is n type semiconductor, the great part of charge carriers will be electrons which move opposite direction of applied electric current. In the presence of external magnetic field, electrons with drift velocity V_e experience Lorentz force given by the equation;

$$\vec{F}_m = q(\vec{V}_e \times \vec{B}). \quad (3.2)$$

Under influence of Lorentz force, moving electrons are deflected in negative y direction which makes lower edge of semiconductor negatively charged while upper edge becomes positively charged. Thus, electric field E_y is generated in the semiconductor and this field applies a force on electrons given by,

$$\vec{F}_e = q\vec{E}_y. \quad (3.2)$$

When the system reaches the equilibrium, the electric force becomes equal to the magnetic force,

$$\vec{F}_e = \vec{F}_m \quad (3.3)$$

$$q\vec{E}_y = q(\vec{V}_x \times \vec{B}) \quad (3.4)$$

Thus, the electric field can be found by using equation 3.4,

$$E_y = V_x B_z \quad (3.5)$$

If total charge in this slab is Q, then free carrier density n is given by,

$$n = -\frac{Q}{wldq} \quad (3.6)$$

Moreover, current is defined as the amount of charge that flows per unit time. By combining equation 3.6 with current, one can find current as,

$$I = \frac{Q}{T} = -\frac{nqwld}{T} = -nqV_x wd \quad (3.7)$$

If we rearrange equation 3.7 and substitute drift velocity in equation 3.5, electric field is given by,

$$E_y = -\frac{IB}{nqwd} \quad (3.8)$$

It is also possible to write electric field in terms of hall voltage,

$$E_y = \frac{V_H}{w} \quad (3.9)$$

By combing equation 3.8 and 3.9, Hall voltage V_H is given by,

$$V_H = -\frac{IB}{nqd} = \frac{R_H IB}{d} \quad (3.10)$$

where R_H is equals to $-\frac{1}{nq}$ and it is called as Hall coefficient. If charge carriers in semiconductor are holes, Hall coefficient R_H is given by $R_H = \frac{1}{nq}$. In SHPM, by measuring Hall voltage, knowing applied current and external magnetic field, Hall coefficient can be calculated easily. Moreover, since sign of Hall coefficient changes according to the sign of current carrying charges, this enable to determine the type of semiconductor used in the experiment. On the other hand, if current is through a semiconductor whose Hall coefficient is already known, magnetic field coming from this material can be determined by measuring Hall voltage.

In SHPM, distance between hall probe and surface of a sample is a critical parameter. Since magnetic field decreases with distance, distance between hall probe and surface must be very close to each other in order to measure small magnetic field²¹. When a hall probe is brought proximity of a sample and applied a current through two arms of hall probe, a fabricated Hall probe being a sensitive to perpendicular component of stray magnetic field produced by sample creates a Hall voltage. This Hall voltage is measured from other two arms of the Hall sensor. Therefore, unknown magnetic field coming from sample can be determined. Resolution of this magnetic field is limited dominantly by Johnson noise due to thermal agitation³.

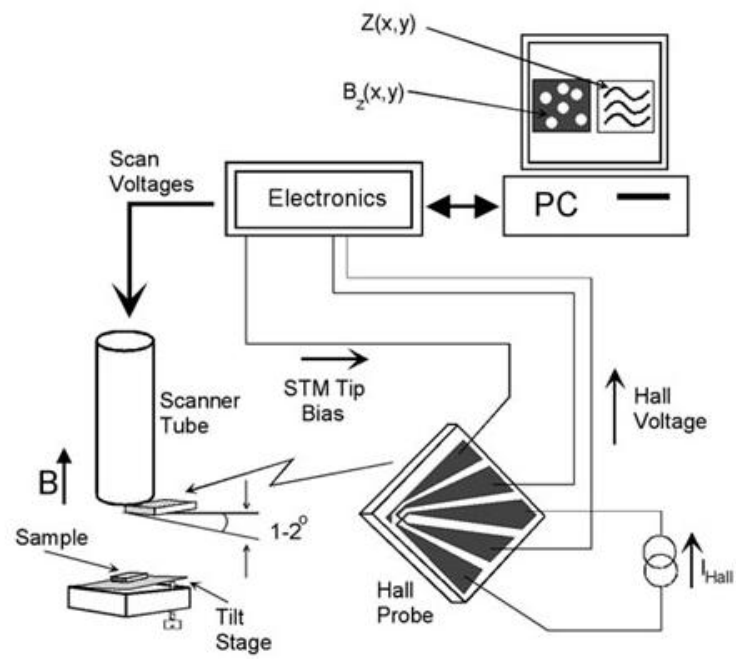


Figure 2.5: Schematic layout of the Scanning Hall Probe Microscope².

CHAPTER 3

SCANNING HALL PROBE MICROSCOPE

3.1 Introduction

Magnetic domain is a small region of magnetic moments where all magnetic moments are aligned in the same direction. Magnetic domains structure plays a very important role in development of magnetic storage technology. Each domain corresponds to a bit and recorded in a magnetic medium. Size of the bit determines the storage capacity and it needs to be decreased in order to increase density of recording. Size and various properties of magnetic domain structure can be investigated and well understood by using different imaging methods at nano-scale such as MFM, Magneto Optics (MO), SQUID, and SHPM. Besides, these techniques are not only used for observation of magnetic domains in magnetic recording media but also vortices in superconductive materials or any other magnetic properties in magnetic materials. Some of the common important features of magnetic imaging methods can be listed as follows: quantitative measurements, fast scan speed, high magnetic field sensitivity and high spatial resolution.

Both magnetic field sensitivity and spatial resolution are the most critical parameters for magnetic imaging application and Figure 3.1 illustrates the comparison of these parameters for different magnetic imaging tools²². As seen from this figure, the highest magnetic field sensitivity can be obtained by SQUID despite the fact that its spatial resolution is limited around 5–10 μm . On the other hand, MFM provides higher

spatial resolution than SQUID and it can be performed at different measurement condition such as in vacuum condition, which can further improve the sensitivity and at ambient temperature as well as low temperature²³. Together with its benefits, MFM has much poorer magnetic field sensitivity as it is compared to SQUID and SHPM. Among them, SHPM offers reasonable spatial resolution and magnetic sensitivity at the same time. By using SHPM, it is also possible to get topographic image of investigated sample simultaneously. Last but not least, it yields quantitative measurements without damaging sample surface at both room and low temperature.

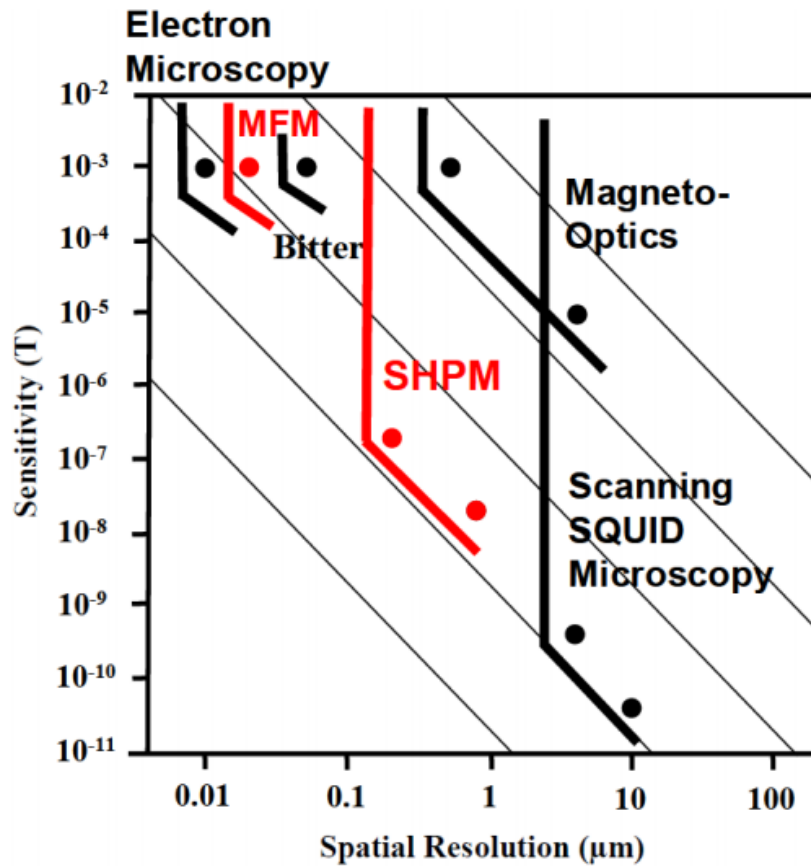


Figure 3.1: Comparison of magnetic field sensitivity and spatial resolution of the different imaging techniques²².

In this chapter, all mechanical and electrical components of SHPM will be discussed in detail. Two cryostat systems are used in order to obtain local magnetic measurement of a sample and electrical characterization of the fabricated hall sensor in a wide range of temperature during this work will be also introduced. In the third part of

this chapter, all scanning modes of SHPM are explained. Last but not least, theoretical and experimental aspects of Quartz Tuning Fork (QTF) as force sensor are presented

3.2 Scanning Hall Probe Microscopy

3.2.1 The Microscope Design and Operation

As with other SPM, SHPM is composed of five main parts; the probe, approaching system, scanning system, electronic controller unit and the software³. Figure 3.2 shows the LT-SHPM system manufactured by NanoMagnetics Instruments Ltd. The microscope insert consists of the LT-SHPM head, the flange and radiation baffles. All the electrical wires coming from the SPM electronic pass through the cylindrical tube and they transmit signal from electronic unit to the sensor. Length of the microscope is adjusted so as to bring the sensor at the center of magnetic field when it is inserted to the cryostat. Furthermore, there are 6 radiation shields at certain distances surrounded the microscope body, which reduces heat load coming from top part of the microscope.

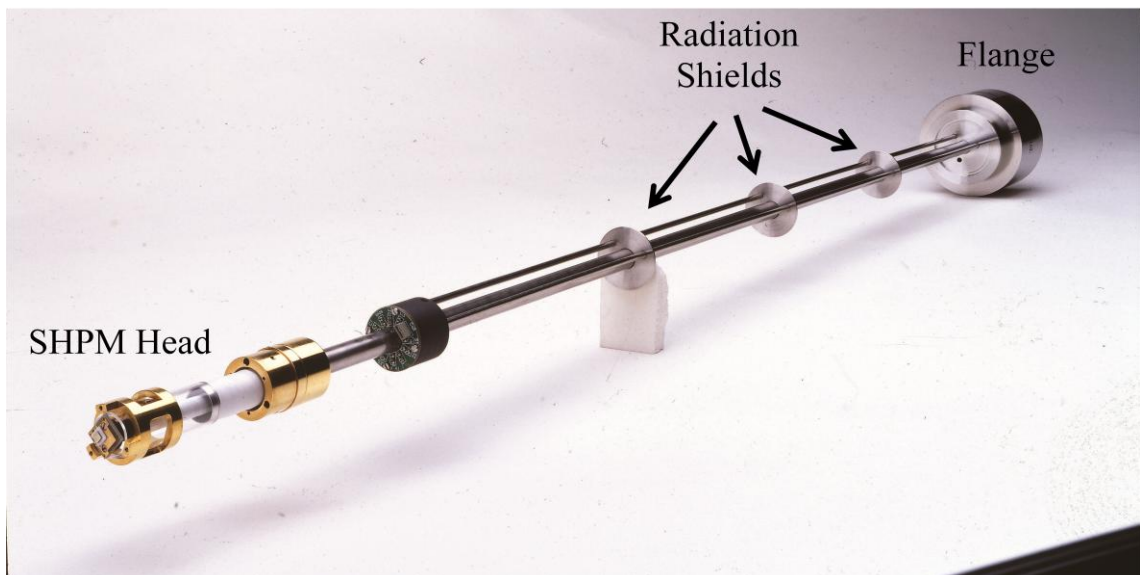


Figure 3.2: Photograph of LT-SHPM used in the experiments²⁴.

The microscope shield shown in Figure 3.3 protects the SHPM head and its components from mechanical damages and it also maintains temperature uniformity. After making sure that the sensor works properly, the shield can be fixed to the head of SHPM and the microscope can be loaded the cryostat safely. Moreover, a coil which can apply a constant small magnetic field can be integrated the shield. It allows quick measurement of the Hall coefficient of the sensor and gives an idea about performance of the sensor used before the microscope is loaded to a cryostat.

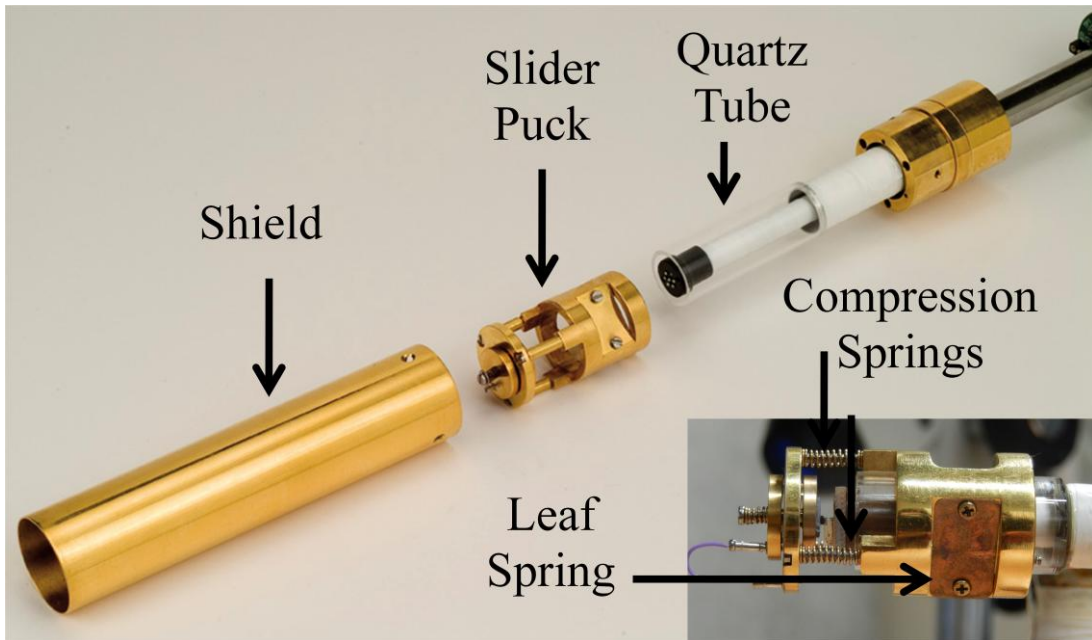


Figure 3.3: Detailed photograph of LT-SHPM ²⁴.

Checking whether the fabricated hall sensor works properly or not is highly recommended before mounting the sample to the microscope or before making any further steps. For this, the Hall sensor is driven by a constant Hall current value and nulled by using SPM software in order to reduce offset voltage in the absence of the magnetic field. Then, a permanent magnet is approached to the sensor. Therefore, increase or decrease in Hall voltage output ($V_{\text{Hall Out}}$) signal can be observed in the SPM software by connecting it to one of the channel located in the spare Analog to Digital Converter (ADC). If opposite magnet field direction is applied to the Hall sensor, $V_{\text{Hall Out}}$ signal is reversed. In addition to this, opposite direction of current result in changing polarity of $V_{\text{Hall Out}}$ signal as well for the proper working Hall sensor. $V_{\text{Hall Out}}$ signal of 500 nm Bismuth Hall probe versus time for $-10 \mu\text{A}$ current is

shown in Figure 3.4. There is offset voltage after nulling the sensor. When the magnet is approached initially to the sensor, V_{Hall} out is increased as seen from this figure. Since the polarity of magnet is reversed around the fifth second, V_{Hall} is increased in the opposite direction with almost same magnitude on the graph.

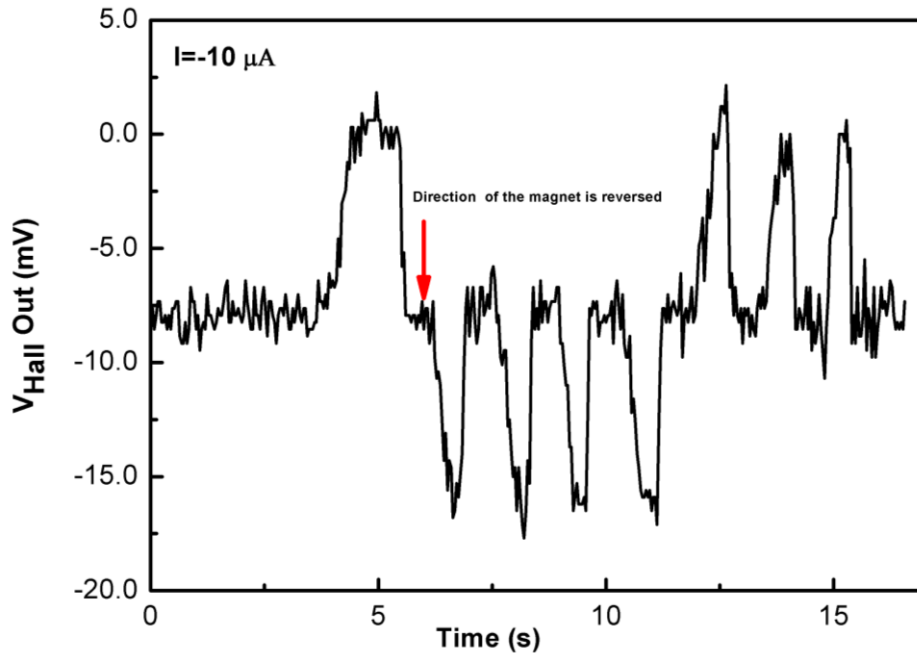


Figure 3.4: V_{Hall} Out vs Time graph of a 500 nm Bismuth Hall probe for $-10 \mu\text{A}$ Hall current.

The sample to be measured must be as clean as possible to obtain better experimental data. For STM feedback the sample must be conductive. On the other hand, both conductive and non conductive sample can be measured by using AFM tracking mode. Silver paint is used in order to glue the sample on the sample holder. After gluing the sample, the holder is attached to the slider puck. There are three quartz hemispheres on the XY slider. They decrease the friction and therefore they provide easier movements of the sample holder. After the sample and the sensor are attached properly to the microscope, the slider puck is mounted to the quartz glass tube by using a leaf spring and two screws as seen from Figure 3.3. Mounting the sample slider puck to the quartz tube is a crucial step. Excessive force should not be applied in order to avoid damaging to the glass tube and the leaf spring must be tightening at right amount. On the other hand, if the screws on the leaf spring are too loose the puck can fall down.

Piezoelectric materials are commonly used in nanotechnology. In particular, they are fundamental tools in SPM technology due to its precise movement of both scanning and tip-sample approaching mechanism. Furthermore, piezoelectric materials are suitable for low temperature applications which expand their area of usage. They basically convert the mechanical energy to electrical energy or vice versa. When a voltage is applied to a piezoelectric material, it changes its size by extending or contraction according to polarity of applied voltage. Piezoelectric materials are widely preferred for approaching system due to its accurate movement. Since they move in micron scale, an approach mechanism which provides greater steps is required for course approach process. In SHPM, the sample is approached to the sensor by using stick/slip coarse approach mechanism, after the sample and the sensor are fixed on the microscope. In this mechanism, first a voltage with slow ramp is applied to slider piezo which results in slow movement of the slider puck in forward direction together with the piezo tube then this voltage value is turned back to its initial value very fast, which causes to move quartz tube in opposite direction while the slider puck stays stationary. Consequently, the slider puck is moved in desired direction. Moreover, this saw-tooth voltage signal applied to the piezo tube can be set up to 400 V. Step size of movements can be adjusted by changing voltage values although step size are not reproducible for the same voltage value at each approaching application ³.

After the sensor is brought to the sample surface close enough, first of all the sample is aligned parallel with respect to the Hall Sensor by using three compression springs under a light microscope. Alignment is carried out at a safe distance and it is completed when the Hall sensor and its reflection on the sample surface is exactly parallel to each other. Alignment accuracy of the sample can be easily understood by bringing the Hall sensor very close to the sample and checking it from different sides by using bottom illumination of the optical microscope. Next, one of the compression springs located back side of the sensor is loosen around one and a half tour so that edge of the sensor becomes closest point to the investigated sample. Angle between edge of the Hall sensor and the sample surface should be between 1–1.5° for precise and high resolution data acquisition. Small number of step sizes has to be used while the piezo tube is moved in z direction. Besides, before the sample is tilted, the sensor must be retracted to a few hundred microns away in order to avoid the Hall sensor crashing into

the sample surface. The picture of the hall sensor and the sample mounted on the slider puck during these processes is presented in Figure 3.5 (a). Figure 3.5 (b) and (c) illustrates tilted Hall sensor with respect to the sample surface from different views.

After the sample is tilted around 1.5° with respect to the Hall sensor, the sample is ready to approach. For this, generally automatic approach is preferred. When the automatic approach is used to bring the sensor close the sample surface, at each step piezo first fully retracted and check the set interaction value which can be either tunneling current or frequency shift depending on feedback mechanism used and then the piezo is extended to a few steps. Automatic approach process continues until interaction value reaches the set value.

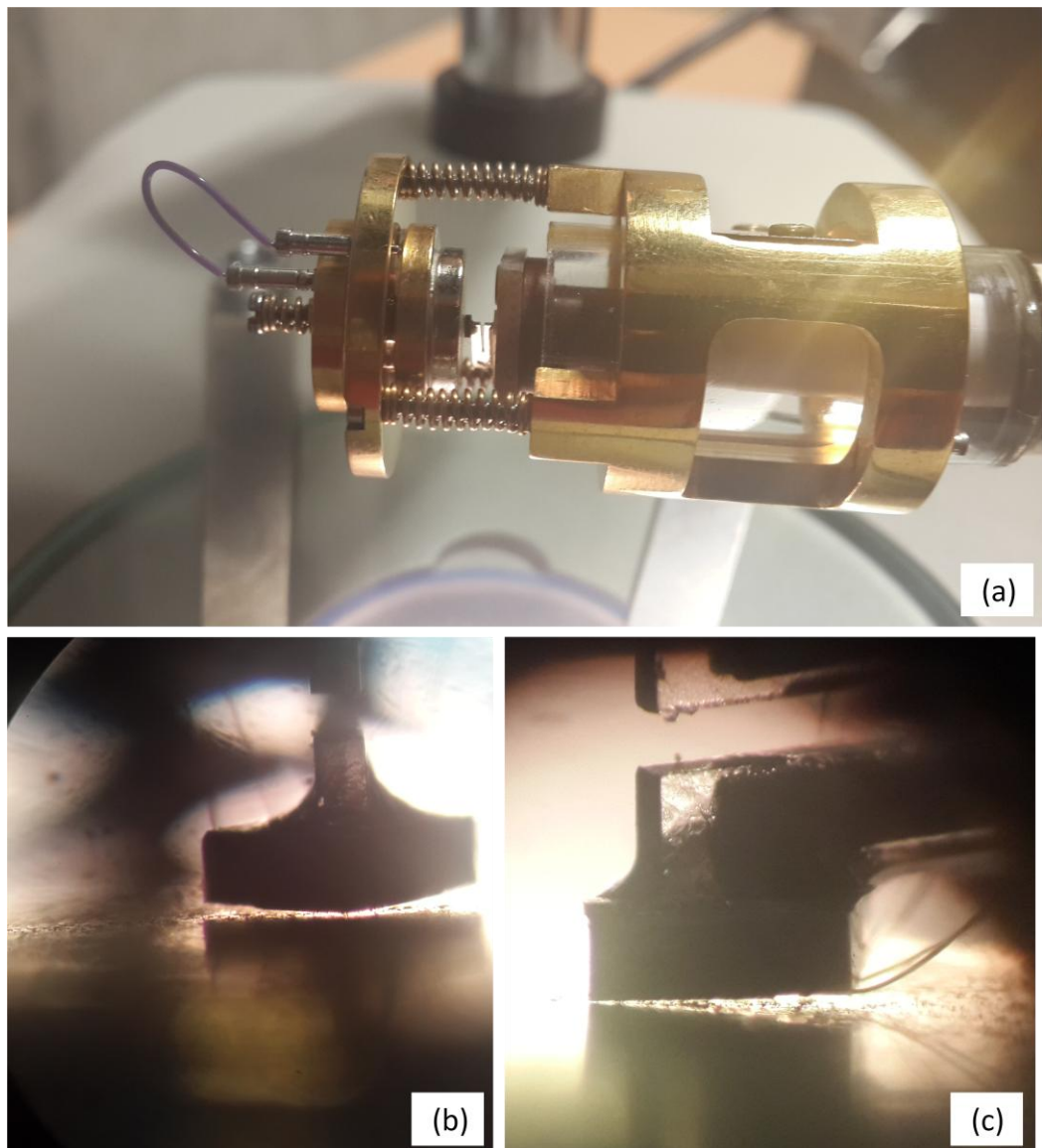


Figure 3.5: (a) The illustration shows the Hall sensor and the sample mounted on the slider puck while alignment process is carried out under optical microscope (b) and tilted Hall sensor with respect to the sample surface from different views front and (c) side.

There are three piezos fixed on the microscope. The first one, slider tube piezo, is used for approaching as it is mentioned above and the second piezo is used for scanning called as scanner piezo. Piezo tube consists of distinct electrodes which allows movement in three direction x, y and z with high precision. Expansion or contraction in desired direction is achieved by giving voltage to the appropriate electrodes. Voltage values and thus movement of the scanner is well controlled by using SPM software and electronics in SHPM. Different piezos respond differently to the applied voltage based on its sensitivity. The sensitivity of piezoelectric material is defined by displacement of the piezo per applied voltage and it is directly affected by thickness of piezo tube, temperature condition etc. Furthermore, piezoelectric materials exhibit hysteresis effect. It means that there is a nonlinear relationship between applied voltage and output displacement. This can result in image distortion. In addition to hysteresis and sensitivity, another important issue to be considered is behavior of piezoelectric materials at cryogenic temperature. Electronic properties of the Hall sensor such as mobility, conductivity or charge carrier concentration depends on temperature and also field sensitivity of the Hall probe varies with changing temperature. Therefore, low temperature measurements play important role in magnetic imaging. Temperature dependency of both hardware and software components of the microscope have to be taken into account. For instance, calibrated piezo constants should be entered the SPM software control according to temperature value before the measurements take place, because the piezo coefficients are dependent directly on the temperature. They decrease as the temperature is lowered. If the piezo coefficients are not entered the software correctly, the size of scan area or step size as the sample is approached to the Hall sensor differs from their actual value. Maximum scan range is also having temperature dependency and it is extended with increasing temperature. For the microscope we used, the maximum scan range at room temperature is $108 \times 108 \mu\text{m}^2$ while this value is $18 \times 18 \mu\text{m}^2$ area at 4 K. Scan speed, size of scan area and number of scans are adjustable parameters. Scanning is initiated from SPM software program and it can be stopped

whenever it is required. Scanning modes and feedback mechanism will be discussed later in this chapter.

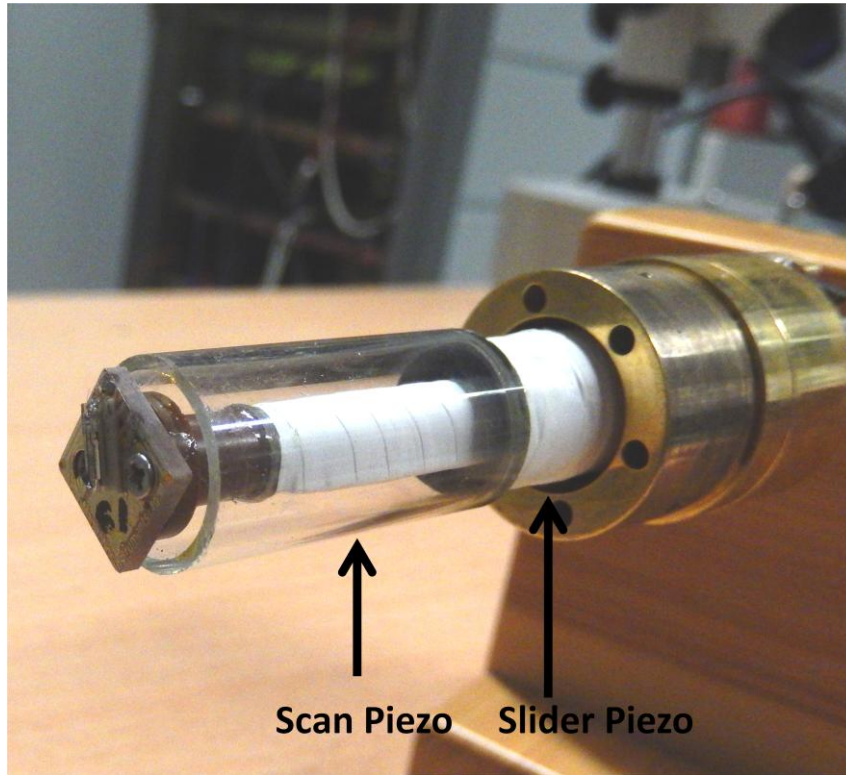


Figure 3.6: Picture of scanner and slider piezos in SHPM.

We used two different commercially available cryostats for the low temperature measurement and high magnetic field application during this study. One of them is, Teslatron PT, manufactured by Oxford Instruments Nanoscience and located in SUNUM at Sabancı University. It is a cryogen free system whose temperature can be controlled between 1.5–300 K. A superconductive magnet integrated the system generates high magnetic field in both direction up to 8 T with maximum field ramp rate 0.207 T/min. Besides, the other cryostat system, supplied by Cryogenic Limited, located at NanoMagnetics Instruments Ltd., is used mostly for magnetic imaging and characterization of the fabricated Hall probes. It is also a closed cycle cryogen free cryostat and any temperature between 1.6 K and 300 K can be stabilized easily. Although the systems specification allows changing the sample rod at any temperature, the microscope must be loaded or removed from the cryostat when the temperature of the variable temperature insert (VTI) sample space is at 300 K to prevent the

microscope from thermal shocks. The rate of temperature must be adjusted between 2–3 K/min in order to protect components of the microscope from mechanical damage when it is cooling down or warming up to a desired temperature. Furthermore, not only measurements can be obtained in He exchange gas; but also the sample space can be pumped up to 10^{-5} mbar vacuum level by turbo pump and magnetic imaging or electrical characterization can be performed in vacuum environment. This comes into prominence when working with the graphene hall sensor.

Last but not least, performance of the fabricated sensor is determined initially with the help of a test station manufactured by NanoMagnetics Instruments Ltd. Since it does not include essential mechanical components for scanning such as scanner and slider piezo, it is not suitable for magnetic imaging. However, it is designed to measure Hall voltage response, Hall coefficient and noise spectrum of the sensors one after another by connecting to head amplifier to the appropriate test station head as it is possible to mount two or three sensors to test station at the same time. The benefit of using the test station is achieved by that it enables to select the most promising sensor according to electrical characterization results among the mounted sensors before scanning step. Besides, it also allows doing measurements in vacuum environment and in a wide range temperature including cryogenic temperature.

3.2.2 LT–SHPM Electronics

There are various electronic cards which are used for different purpose and operation in the LT–SHPM control electronics. Some basic properties of these cards are given as following:

- a) POWER SUPPLY CARD
- b) DAC CARD
- c) CONTROLLER CARD
- d) SLIDER CARD
- e) HEAD AMPLIFIER
- f) PHASE LOCKED LOOP CARD
- g) SPARE ADC
- h) SCAN DACS

- i) HIGH VOLTAGE AMPLIFIER
- j) CONTROLLER CARD
- k) HALL PROBE AMPLIFIER CARD
- l) MICRO CONTROLLER AD CARD

3.2.3 LT-SHPM Software

NMI SPM program (version 2.0.16) written by Nanomagnetics Instruments Ltd is used in LT-SHPM measurement in order to adjust related parameters with the experiments. Before performing scanning or any other steps, suitable scanning mode must be selected and other commands like approaching, scanning or finding resonance frequency of cantilever is set in this program. Besides, the software makes it possible that the collected data can be edited. For example; obtained images can be corrected by using plane or line correction. In addition, basic process like cropping image, measuring distance between two features and measuring roughness can be done via NMI SPM. Various filtering are available in this program such as mean, median, Gaussian or parametric low pass filter. There are also another program written by NanoMagnetics Instruments Ltd exists for data editing called NMI SPM which allows the processing of collected images.

3.3 Scan Modes of LT-SHPM

LT-SHPM can be operated with different modes by mounting appropriate tip to microscope according to type of modes. Scanning mode of SHPM is preferred by considering the sample type, required resolution or image acquisition time. There are three different scanning modes of SHPM: tracking mode with STM or AFM feedback, lift-off mode, real time mode. Each mode has some advantages and disadvantages on its way. Details of these modes will be discussed in the following subsections.

3.3.1 Lift-off Mode

Lift-off mode is widely used method in SHPM due to its several advantageous. The greatest benefit of the lift-off mode is being very fast since it does not use any feedback mechanism. Scan speed of this mode is approximately 4s/frame². Moreover,

with this mode flicker noise ($1/f$ noise) can be reduced by taking average of images obtained ³.

For the lift-off mode operation, first of all the sample-sensor angle is adjusted and then the sample is approached to the sensor by using STM feedback control. As the desired tunneling current is established, approaching stops and initially area which will be scanned must be checked to be sure that it has free of contaminations. For this purpose, the sensor is lifted off a few microns away from the sample surface and the sensor is moved to four edges of the scan area to confirm that there is no tunneling current between the sample and the corner of Hall sensor. If the tunneling current is observed in any corner, it means there is an obstacle on the sample surface and lift-off distance must be increased in order to avoid crushing the sensor to the sample surface. In this case, after increasing distance between the sample and the sensor, corner checking process should be repeated. When ascertained that there is no contamination in the scanning area, scanning is performed at certain height from the sample surface. One of the drawbacks of this mode is that only magnetic imaging can be obtained, since there is no feedback mechanism it is not possible to get topography image in this mode. Besides this, as distance between the sample and the Hall sensor is a bit much compared the other modes such as AFM or STM tracking modes, both spatial and magnetic resolution are slightly decreased ^{3, 21}.

3.3.2 Real Time Mode

Another mode used in SHPM application is known as real time scanning mode. Real time scanning mode does not use any feedback mechanism as in the case of lift-off mode and scanning is completed with very fast scanning speed. The scan speed of the real time is reported as 1 s/frame. The major difference between lift off and real time mode is that obtained image is displayed once scanning is finished ³. Figure 3.7 shows magnetic images of bismuth substituted iron garnet thin film under different external magnetic field by using real time scanning mode in SHPM ²⁵. It is reported that these images are taken less than 10 s with this mode.

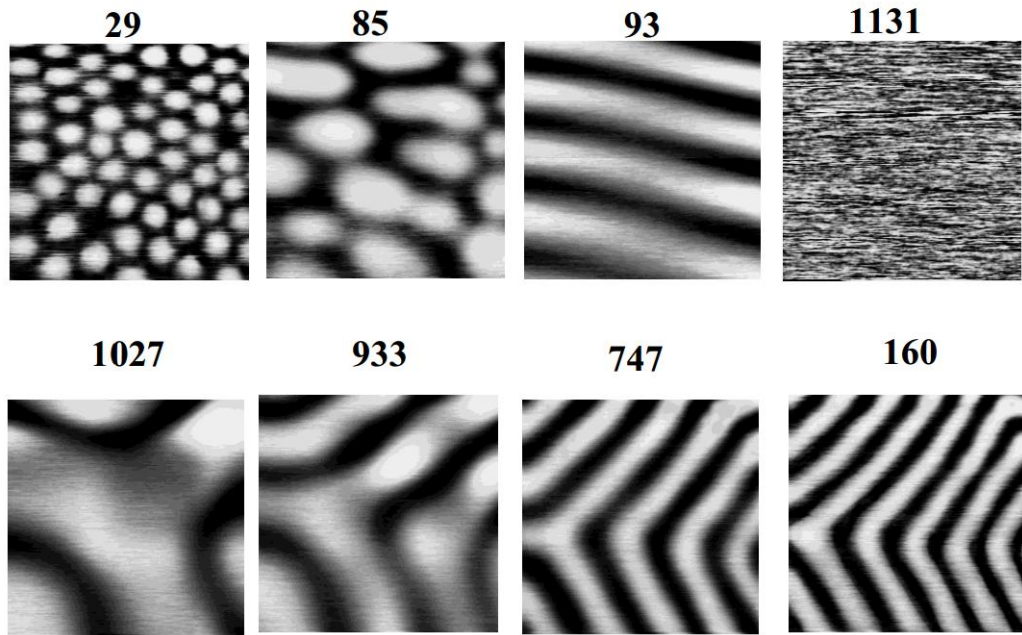


Figure 3.7: SHPM images of Bismuth substituted iron garnet thin film taken by using real time scanning mode. Values above images represent applied perpendicular magnetic field to bismuth substituted iron garnet thin film ²⁵.

3.3.3 AFM/STM Tracking Mode

In STM tracking mode, firstly tilted sample is approached to the sensor via stick–slip approach mechanism until the desired tunneling current flows between the sample and the sensor. Tunneling current is measured at individual points on scanning area and this current value is then sent to the SPM electronics as feedback so that the distance between sensor and the sample is maintained at certain height throughout scanning process ³. Typical tunneling current value used in STM tracking mode is around 0.1nA.

In the fabrication process of the Hall sensor, a metal structure (mostly gold is preferred for metallization) is defined by optical lithography which will be used later as STM tip for STM tracking mode. Figure 3.8 shows optical microscope image of the Hall sensor which is patterned by photolithography and STM tip located left side of the Hall cross ².

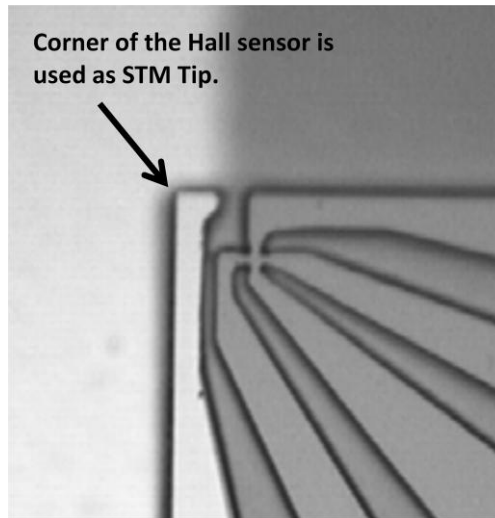


Figure 3.8: Optical microscope image of the Hall sensor designed and fabricated for STM tracking mode².

In STM tracking mode, both topography and magnetic image can be obtained simultaneously by choosing related image channel from SPM software. Distance between the sample and the sensor is reduced in this mode and therefore high magnetic field resolution can be obtained. One of the disadvantages of this mode is that only conductive samples can be measured. Moreover, scanning speed is much slower in this mode as compared the lift-off or real time mode since feedback mechanism is active during scanning.

The other scanning method which uses feedback mechanism is AFM tracking mode. The major benefit of this mode is that not only conductive samples but also non-conductive samples can be investigated. It also provides high magnetic field resolution as in the case of STM tracking mode since the tip can be brought very close to the sample surface. In this mode, force between tip and sample can be measured with various detection methods such as optical and piezoresistive detection systems. Therefore, tip-sample separation can be precisely controlled²⁶.

Operation of AFM tracking mode is very similar to that of STM tracking mode with some exceptions. In AFM tracking mode, the sample is aligned parallel with respect to Hall sensor as in the STM tracking. Then, it is pulled back to a safe distance

in order to not to crush the sample to the sensor when the sample is tilted. As tilted sample is approached to the sensor with stick–slip mechanism, resonance frequency of the sensor shifts because of the tip–sample interactions and shift in the resonance frequency is used as feedback instead of tunneling current in this mode.

There are two ways to produce sensor for AFM tracking mode. In the first way, an AFM tip and Hall cross are fabricated in a single cantilever with different designs^{27, 28, 29}. Figure 3.9 (a) and (b) show the SEM images of such cantilever. In this work, they fabricate the Hall cross on an AFM tip apex as is shown in bottom and left view in same Figure³⁰. They begin fabrication with defining 20 μm high pyramid of the cantilever by wet etching process and then they deposited silicon nitride by using plasma–enhanced CVD in order to provide electrical isolation between silicon and Hall cross region. Finally, they patterned 400 nm Bismuth Hall cross structure on the center of the pyramid by EBL and lift off process. Resonance frequency of this cantilever is measured as 157 Hz. Figure 3.9 (c) and (d) show surface topography and magnetic imaging results taken by using this cantilever³⁰.

Alternatively, piezoelectric materials can be used for designing sensors which have both magnetic sensing and distance control elements in a single cantilever. However, piezoelectric material with a large piezoelectric coefficient and high mobility should be preferred for better scanning results of topography and magnetic imaging. For this purpose, $n\text{-Al}_{0.4}\text{Ga}_{0.6}\text{As}$ is used in a few of the experimental works^{29, 31}. Al component in this alloy ensures that material have a higher piezoelectric coefficient. Side and top views of such a cantilever is illustrated in Figure 3.10 (a)³¹. As is clearly seen from SEM image, Hall cross and sharp AFM tip with 2–2.5 μm height is a few micron away from each other in this cantilever (Figure 3.10 (b)). In this work, they reported longitudinal piezoelectric coefficient of the material in [011] direction is $1.35 \times 10^{-9} \text{ Pa}^{-1}$ at room temperature. They also measured quality factor and resonance frequency of the sensor between 300–500 and 18–21 kHz respectively in environment condition while quality factor increased to over 10,000 under a vacuum of approximately 10^{-5} mBar . Besides, spatial resolution of the sensor is less than 1.5 μm and Hall coefficient is measured as $3 \times 10^3 \text{ } \Omega/\text{T}$. Magnetic imaging and topography of NiFe rectangles taken by this cantilever are given in Figure 3.10 (c) and (d)³¹.

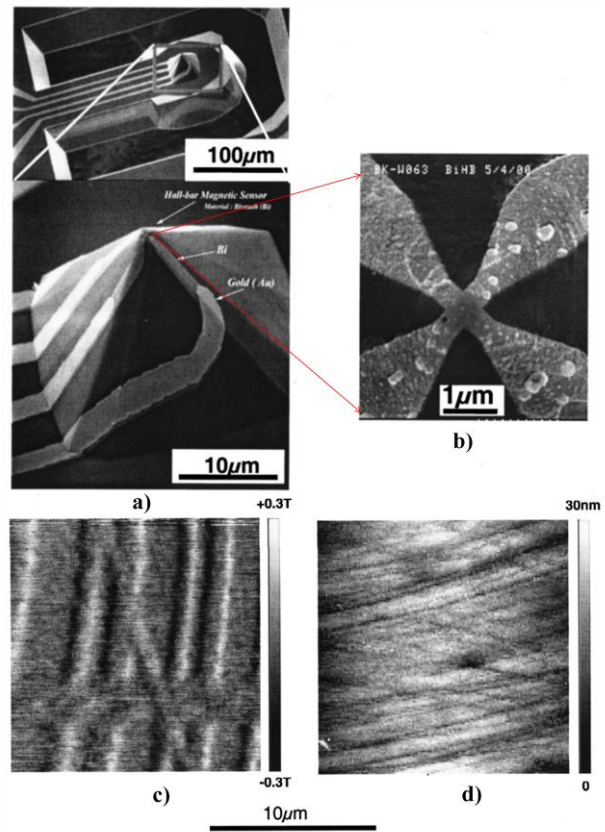


Figure 3.9: (a) SEM images of the Hall sensor integrated AFM tip apex for different magnifications. (b) High magnification SEM image of Hall cross located at the end of the silicon cantilever (c) and (d) topography and magnetic image of 40 MB computer hard disk respectively³⁰.

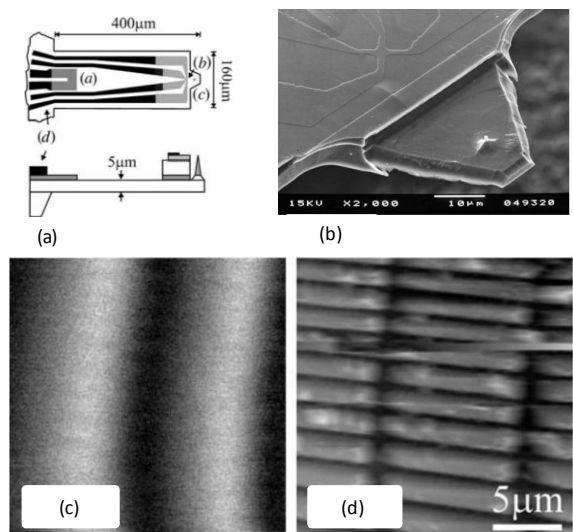


Figure 3.10: (a) The schematic illustrates top and side view of the cantilever which consists of two sensors for both topography and magnetic imaging. (b) SEM image of the fabricated sensor. Surface topography (c) and SHPM image of array of NiFe rectangles ³¹.

There are different designs and fabrication ways for combined cantilevers in literature. Although having additional component for distance control is not necessary and advantageous for the sensors produced with this way, it is not only high costly and but also difficult method to fabricate. QTF is used as an alternative method in SHPM for AFM tracking mode. For this purpose, the Hall sensor is mounted on top of the commercially available QTF which is used as a force sensor for approaching mechanism and control tip–sensor separation during scanning process in SHPM application. In the following section, details of the theoretical and experimental aspects of QTF as force sensor will be presented.

3.4 Quartz Tuning Fork Force Sensor for AFM Tracking Mode in SHPM

Piezoelectric effect is a property of some materials that can generate electrical energy when they are subjected to mechanical pressure. After this phenomenon is discovered by Jacques and Pierre Curie, they reported piezoelectricity in their first paper in 1880 ³². They also designed piezoelectric quartz electrometer which is capable of measuring very small amounts of current values with high precision. Since then, piezoelectric materials have been widely used either in engineering or in daily life such as motors, lighter, musical instruments, keyboards, actuators or various kinds of sensors.

Nowadays, piezoelectric materials exist naturally as well as they can be manufactured in any desired sizes and shapes. Quartz, tourmaline and Rochelle salt are some of the examples of natural piezoelectric materials whilst lead zirconate–titanate, barium titanate and silicon selenite are examples of synthetic ones ³³. Among them, the most abundant natural piezoelectric material is known as quartz which is one of the crystalline forms of silicon dioxide (SiO₂). Quartz crystals have been employed in various applications due to their unique properties such as high young modulus, high mechanical stress and lack of hysteresis and pyroelectric effect ³⁴. One of the important

and well known applications of quartz crystal is Quartz Tuning Fork(QTF). QTF can be used in various fields. Most widely, the watch industry uses them since it is not only low-priced and but also more precise than balance wheel. Besides, they have been used in spectroscopic gas sensor which enables analyzing of samples with volume of 1 mm^3 ³⁵. QTF is first implemented successfully in scanning probe microscopy by Günther *et. al.* in 1989. They achieved $3 \text{ }\mu\text{m}$ lateral resolution and 5 nm vertical resolution of a grating sample with $8 \text{ }\mu\text{m}$ periodicity by Scanning near-Field Acoustic Microscopy (SNAM)³⁶. Later, it has been applied to scanning near field optical microscope (SNOM) for distance control and measuring shear force quantitatively³⁷. It can be also used in MFM in both room temperature and low temperature applications^{38, 39}. In addition to this, AFM takes advantage of QTF owing to its high quality factor and stable resonance frequency. Using QTF in AFM both shear force and normal force can be measured by attaching tip either perpendicular or parallel to oscillation direction respectively. 100 nm lateral resolution has been reported in the earlier study by attaching a tip with 150 nm apex to QTF⁴⁰. One of the prominent studies by using QTF in AFM has been performed by Franz Giessibl in 2000. In this work, he glued one of the prongs of QTF to a substrate and mounted a sharp tungsten tip to the free prong. Then, he managed to obtain atomic resolution image of Si (111) under vacuum condition (Figure 3.11)⁴¹.

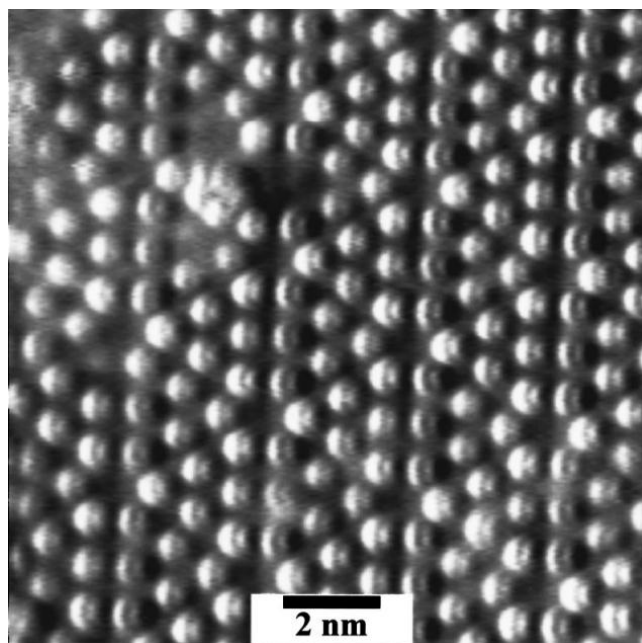


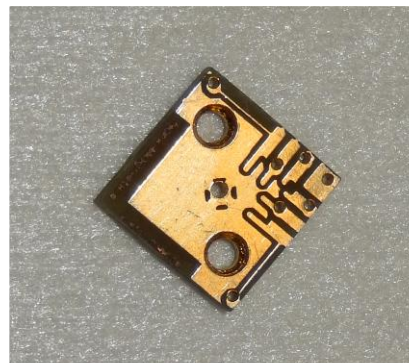
Figure 3.11: AFM image of Si (111) under vacuum by using a sharp tip attached to QTF⁴¹.

QTF works successfully in different condition such as low temperature, high magnetic field or vacuum. Furthermore, QTF is superior than Si cantilever in some respects. For example; it has high quality factor which allow measuring frequency shift with higher accuracy and it has high stiffness which avoids tip jump into contact with sample surface⁴². Therefore, it also took important place in SHPM application. In SHPM, conductive samples are easily measured by STM tracking mode but for nonconductive samples, AFM tracking mode has to be used. As previously mentioned, there are different ways to fabricate Hall sensors for AFM tracking mode. Since fabrication of Hall probe which includes both magnetic sensing and force sensing element in a single cantilever is so difficult, alternative method is developed by using QTF. In this method basically, fabricated Hall sensor is attached on top of QTF which has 32,768 Hz resonance frequency (Figure 3.12 (a)). The details of the fabrication of Hall sensor integrated QTF are as follows. First of all, electrical connections on printed circuit board (PCB) should be checked individually by multimeter in order to confirm that there is no short circuit between adjacent pads. Picture of PCB used in SHPM is given Figure 3.12 (b). Then, a thin rectangular ceramic sheet is glued on top of PCB by low temperature epoxy to provide electrical isolation between pads and QTF. Low temperature epoxy is prepared with hardener and adhesive by mixing them under the ratio of 1:2 in volume. The mixture should be applied to the desired pieces as soon as possible before it hardens. Then, pieces are baked at 100°C in an oven to accelerate drying for 20 minutes. Glued pieces can also be dried by leaving them at room temperature for 1 day. Once PCB and ceramic sheet is glued together, QTF can be prepared. Commercially available QTF is enclosed by metal shell under vacuum. QTF can be extracted from its cylindrical metal package with the aid of pliers. In this step, one should be very careful in order to inhibit damaging electrodes of QTF or break QTF itself as it is a delicate material. Legs of QTF are made up of magnetic material. Therefore, they need to be broken off by using soldering iron, because a magnetic material around the sensor affects the measurements and scanning results. If soldering iron touches to soldering joints and a magnet placed close enough to them, then legs are attracted by the magnet and they can be easily removed from QTF. Extracted QTF should be controlled under optical microscope before using it to ascertain that electrodes

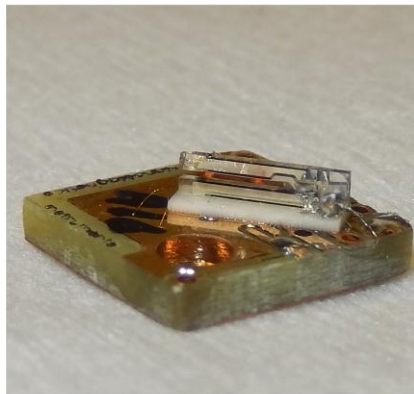
are not damaged. Then QTF is glued on ceramic sheet as flat possible by low temperature epoxy as shown in Figure 3.12(c). Once epoxy dried, electrical connections from QTF to PCB can be taken with thin non-magnetic wire by soldering. After all electrical connections are controlled by multimeter, PCB should be cleaned with ACE and IPA to remove contaminants on its pads and to provide maximum adhesion for the wire bonding step. Finally, according to application, sensor to be used has to be integrated on QTF. Sharp AFM tip is glued by metal epoxy while low temperature epoxy is used to attach the Hall sensor metal to QTF (Figure 3.12 (d)). Fabricated Hall sensor should be stored in a specially designed box as is shown Figure 3.12 (e).



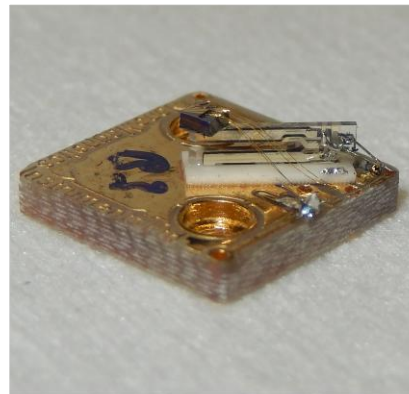
(a)



(b)



(c)



(d)



(e)

Figure 3.12: The pictures show process steps of fabrication of Hall sensor for AFM tracking mode by using QTF. (a) Before (top) and after (bottom) QTF is removed from its metal can. (b) The picture of PCB used throughout measurements during this study. (c) and (d) pictures of QTF which is glued on the top of PCB and Hall sensor attached to QTF respectively. (e) Dedicatedly designed boxes for Hall sensor storage.

Non-contact AFM technique was used to track the surface using a hall sensor that is mounted on a QTF. In AFM tracking mode by using QTF, first of all, resonance frequency of QTF is measured before it is approached to the surface. For this purpose, QTF is oscillated by dither piezo for a predetermined frequency interval and phase and amplitude of the signal is measured. Frequency value at which maximum amplitude occurs is called as resonance frequency. Once resonance frequency of QTF is found, PLL is locked to phase of the signal which comes from QTF. Since QTF is a piezoelectric material when it is vibrated by dither piezo, it produces an electric signal which is typically on the order of nano-Amperes. Generated AC current is amplified by amplifier and converted to the voltage by I-V converter. Therefore, an AC signal which corresponds to mechanical vibration is obtained. PLL is locked to input signal phase. PLL shifts the frequency to keep the phase constant. In non-contact mode AFM shifted frequency (Δf) signal is used as a feedback source. If the QTF is approached to the sample surface, resonance frequency of the QTF shifts due to short range and long range forces between tip and sample. Approaching is completed when Δf equals to the set value entered in the software^{3, 21}. Feedback loop keeps the Δf at that set point. Frequency shift is directly proportional to gradient of force between tip and sample and given by the equation⁴³:

$$\Delta f = \frac{f_0}{2k} \frac{\partial F}{\partial x} . \quad (3.1)$$

In this equation, k is the spring constant and f_0 is resonance frequency of QTF. Moreover, quality factor of QTF is calculated by equation 3.2⁴⁴:

$$Q = \frac{f_0}{FWHM} . \quad (3.2)$$

Here, Q is the quality factor, f_0 is resonance frequency and FWHM is full width half maximum of resonance curve.

Resonance frequency of as received QTF used during study is 32,768 Hz and resonance frequency of each QTF is measured by microscope and SPM software program. In this way, QTF which has higher quality factor can be selected for scanning application to obtain higher resolution as the SPM software calculates quality factor and maximum phase automatically. Figure 3.13 shows dialog box of the SPM software for QTF Auto tune. Once QTF with higher quality factor is distinguished, this sensor is glued on top of QTF. That causes reduction in resonance frequency because of additional mass coming from glue and Hall sensor on QTF. Resonance frequencies of QTFs in air before and after fabricated Hall sensor attached are given in Figure 3.14 (a) and (b) respectively. As is clearly seen from these graphs, central frequency is dropped from 31,857 Hz to 12, 662 Hz after Hall sensor attached to it.

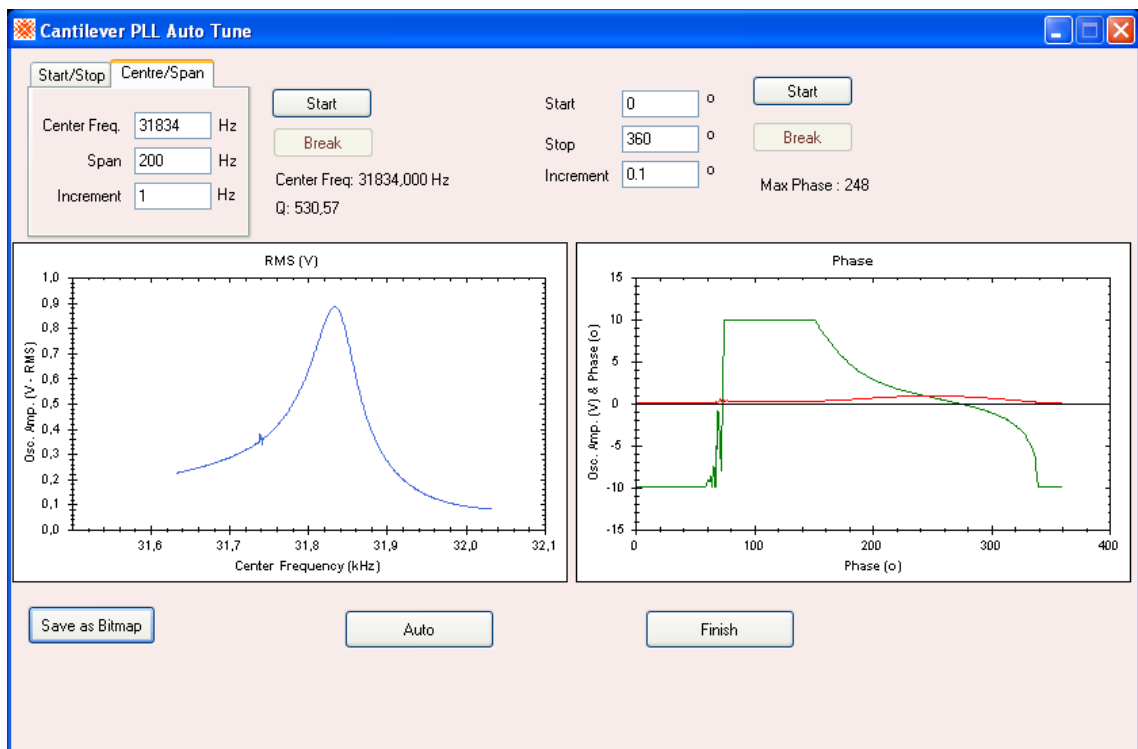


Figure 3.13: Picture of dialog box in SPM software for central frequency, quality factor and maximum phase calculation.

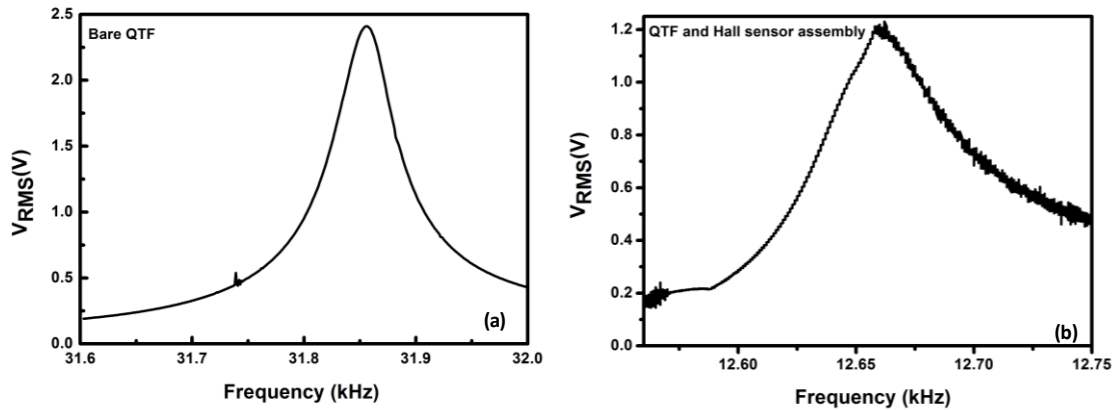


Figure 3.14: Resonance curve of QTF before (a) and (b) after Hall sensor attached to QTF in ambient condition respectively.

Dynamics of QTF are examined in detail by Akram *et. al*⁴⁵. For this purpose, they described motion of QTF as one dimensional driven damped oscillator and they have calculated resonance frequency of it by using both cantilever beam theory (CBT) and simple harmonic motion (SHM). They have found resonance frequency of QTF as 31.7 kHz according to SHO and it was found to be 21.2 kHz according to CBT for QTF whose mass is 2.13 mg with Hall sensor mass of 1.11 mg. In addition to this, they have used COMSOL simulation program in order to obtain resonance frequency and then they compared results with theoretical calculations. For this, they took into account two situations in their simulation: a) both prongs are free and b) one prong is fixed to relatively massive material with and without Hall sensor mounted. In the first situation (both prongs free), there are two eigenmodes including in-phase (symmetric) where both arms of QTF oscillate in the same direction and anti-phase (asymmetric) where both arms oscillate in opposite direction^{3, 45}. In the second situation (one prong free), there is only symmetric mode. Simulation results show that resonance frequency of symmetric mode is close to CBT while it is close to Simple Harmonic Oscillator (SHO) for asymmetric mode. Finally, they fabricated GaN Quantum Well hall sensor and mounted it on top of QTF. Figure 3.15 represents resonance frequency curve of QTF attached GaN Hall sensor for one prong free and both prongs free situations and for two different sizes of quartz tubes⁴⁵. As is seen from this figure, theoretical calculations and experimental results of resonance frequency agree with each other. Minor differences result from mass of glue and Hall sensor⁴⁵.

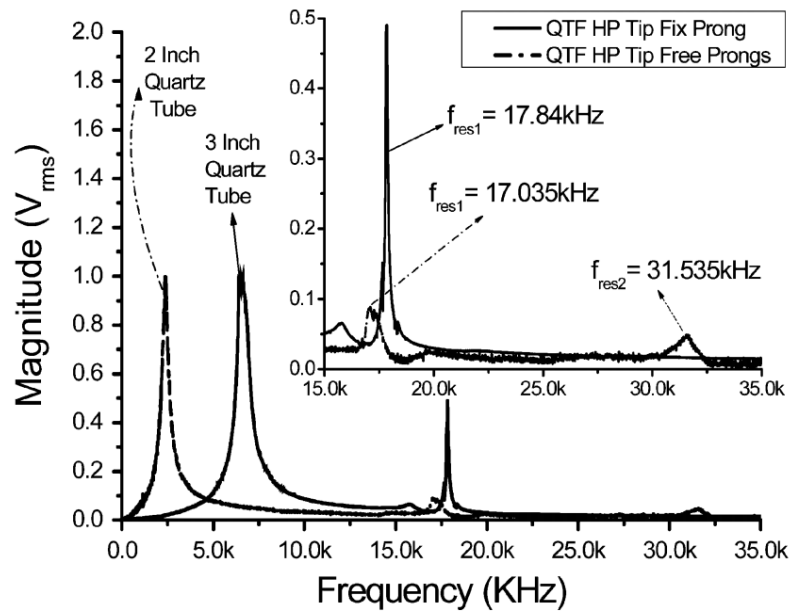


Figure 3.15: Resonance frequency curve of QTF attached GaN Hall sensor for one prong free and both prongs free situations and for two different sizes of quartz tubes ⁴⁵.

Last but not least, temperature dependency of QTF plays important role in SHPM since piezo coefficients, resonance frequency and quality factor of QTF changes with variations of temperature. It was reported that between 77 K and 300 K, resonance frequency increases till 250 K then it starts to decline ^{3,21}.

CHAPTER 4

FABRICATION OF THE HALL SENSOR AND CONVENTIONAL

FABRICATION METHODS

4.1 Introduction

Micro/nanofabrication allows manufacturing of devices with desired patterns on a substrate for engineering or research purpose. Techniques to be used are chosen according to features size, resolution, substrate type, reproducibility or speed of process. For example; for structures with large feature sized (approximately bigger than 1–2 μm) generally photolithography is preferred while electron beam lithography (EBL) can be implemented for smaller features (down to 6–7 nm). Besides, photolithography is more convenient and practical for mass production application. Each technique has its own advantages and disadvantages. However, shrinking dimension of feature size is one of the most prominent goals in all lithographic methods. According to Moore's law, number of components on a chip becomes two times more approximately every two years⁴⁶. This means that critical dimension (CD) produced on a substrate is reduced with new technology and process development every passing day.

In this chapter, conventional device fabrication methods used in Hall sensor production will be presented in detail. Device fabrication process consists of EBL, optical lithography, dry and wet etching, packaging etc will be discussed thoroughly.

Problems faced during fabrication and solutions developed are presented in this chapter. In addition to this, recipes implemented for fabrication of Hall sensor are also provided.

4.2 Nanofabrication Techniques

4.2.1 Substrate Preparation

Wafers to be used in device fabrication must be as clean as possible, since cleanness of the wafers directly affects production yield and performance of fabricated device. It is easier to clean the pieces after cutting the wafers. Therefore, a second cleaning is not needed for debris arising from cutting process.

In this work, we used 4 inch 285–300 nm dry chlorinated thermally grown SiO₂ on top of 500–550 μm thick Si (supplied by Nova Electronic Materials) for graphene Hall sensor and 3-inch semi-insulating GaAs (supplied by American Xtal Technology) wafers for Bismuth hall sensor. Surface orientation is [100] for both of these wafers. As stated above, the wafers are diced into 1.5 × 1.5 cm² or 2 × 2 cm² chips with a diamond scribe to be compatible with mask used in optical lithography, before cleaning procedure applied.

There is a number of different ways to clean the wafers and cleaning methods should be selected according to the type of contaminants on the wafer. After cutting the wafers into small pieces, we initially applied standard cleaning procedure which consists of three stages, since the samples are unprocessed yet. During cleaning process, different beakers are used for each chemical in order to avoid cross-contamination. In the first step, the samples are placed in a beaker filled with analytical grade of acetone (ACE) which solves most organic materials from the sample surface and kept in an ultrasonic cleaner for 5 minutes. Ultrasonic cleaning is required to remove particularly insoluble particulates. Secondly, the samples are soaked one after another in three different beakers of acetone for 30 seconds without allowing them drying when it is transferred from one beaker to another one. This process is repeated by using isopropyl alcohol (IPA). Finally, the samples are flushed with IPA and dried with nitrogen gas.

Completion of the sample cleaning with IPA provides to remove ACE residue from the sample surface.

The other conventional way to remove organic molecules from the sample surface is known as piranha cleaning. Even though there exist different mixture ratios for this solution, we prepare 3:1 ratio of H_2SO_4 (95–97% concentration) to H_2O_2 (37% concentration) mixture and pieces are kept in this solution for 5 minutes. Then, the samples are immersed in deionized water (DI) and this is followed by nitrogen blow dry. It must be noted that piranha solution is not generally used for GaAs cleaning, because it etches GaAs substrate. Moreover, piranha is not only used for the wafer cleaning but also it is widely used for photomask cleaning after repeatedly use of it in photolithography, which will be discussed in the next section.

4.2.2 Optical Lithography

Optical lithography also known as photolithography is a technique which enables transferring of desired patterns into a substrate by using ultraviolet light. Almost all device fabrication flow includes a photolithography step due to its several benefits. One the most significant advantageous of the photolithography is that many devices can be fabricated at a time. Additionally, it can produce micron sized or smaller structure on the sample even though it is relatively low-cost and easy to use method when you compare to the other lithography tools such as EBL.

Once the wafer is diced and cleaned as discussed in the previous section, pieces are initially baked at a temperature between 120–150° C in order to remove water molecule on the samples surface. This step is known as dehydration bake and it is necessary to get better adhesion between the substrate and photoresist film. After the dehydration baking, the substrates are coated with photosensitive material which is composed of resin, solvent and photoactive compound (PAC). Most of the solvent in the photoresist is evaporated during spin coating and soft baking steps and these results in reduction of photoresists film thickness. The soft baking is substantial because it not only solidifies the photoresist so that resist does not stick to an optical mask but also it enhances photoresist to substrate adhesion further. Next, the substrate is aligned with a photomask which contains chromium patterns on a quartz plate. In our experiment, we

used the 4×4 inch mask to be compatible with mask aligner machines in the facilities we used. Structures on the mask are designed with AutoCAD program and manufactured by ML&C GmbH. Figure 4.1 shows the entire photomask having 34 different layers of patterns for Hall sensor fabrication. After alignment of the physical mask, the substrate is illuminated by the ultraviolet (UV) light. There are several exposure modes in photolithography such as contact, proximity and projection. Among them, the best resolution approximately $0.07 \mu\text{m}$ is possible with projection mode; nevertheless it is very expensive system. For our experiment, contact printing system is used and we could achieve around $2\text{--}3 \mu\text{m}$ lithographic resolution. Disadvantage of this method is that the photomask can be easily damaged and it becomes dirty after almost every usage because the mask is in hard contact with the resist coated substrate. In order to remove the resist residue on the mask surface, it was cleaned with acetone in each usage and piranha cleaning was applied once every two or three months. Furthermore, having a gap between the photomask and the sample result in diffraction which limits the resolution of contact lithography. This problem generally arises from particles on the mask and presence of edge bead on the substrate. To avoid this, edges of the coated sample are scratched with scalpel or any other sharp material and the mask should be kept as clean as possible.

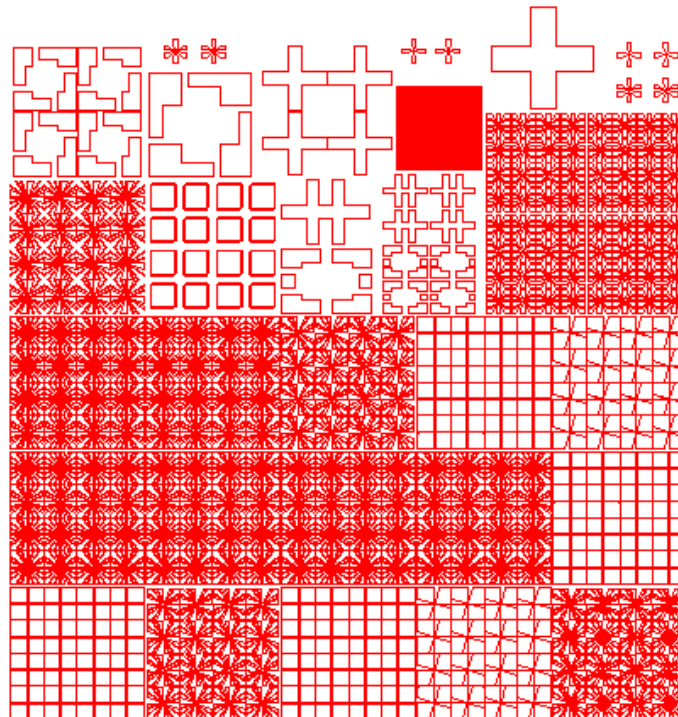


Figure 4.1: The entire mask design which is used for Hall sensor fabrication.

Photoresist being a polymer changes its structure during UV light exposure and it can be sorted into two groups: positive tone and negative tone resists. In positive resists, exposed regions become more soluble in a chemical developer because chain-scission occurs in polymer while areas under mask patterns remain insoluble. On the other hand, solubility of a negative resist decreases during exposure because polymer is cross-linked. Figure 4.2 illustrates comparison of the process flow for both negative and positive tone resists. There are various commercially available photoresist. Since each resist is required different amount of energy and consequently different exposure time, suggested exposure energy given in the technical data sheet for individual resist should be used initially to determine the optimum exposure time. Exposure time can be calculated by dividing exposure dose by a constant UV light intensity of the mask aligner system used. Two mask aligner systems are available at Sabancı University. The exposure intensity of Karl Suss MA6 located at faculty clean room is $1.6 \text{ mW} / \text{cm}^2$ whereas it varies up to $30 \text{ mW}/\text{cm}^2$ for Midas / MDA-60MS placed at Nanotechnology Research and Application Center (SUNUM). Light intensity of Midas mask aligner monitored by lamp power supply unit is set to $25 \text{ mW}/\text{cm}^2$ therefore; less exposure time is required with this equipment compared to Karl Suss. Figure 4.3 shows an optical microscope image of Hall sensor design after development by implementing positive lithography in order to show resolution limits of Midas machine.

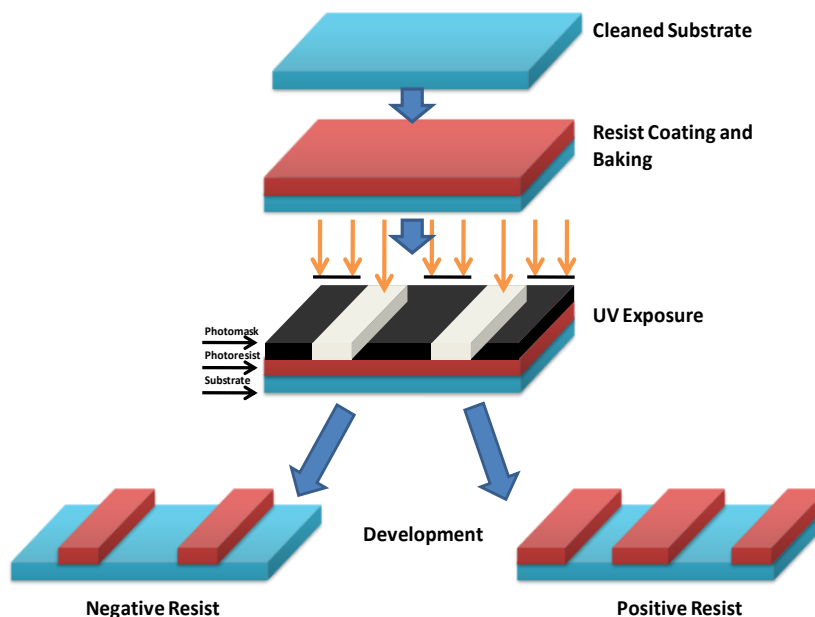


Figure 4.2: Process flow of the photolithography for both negative and positive resist.

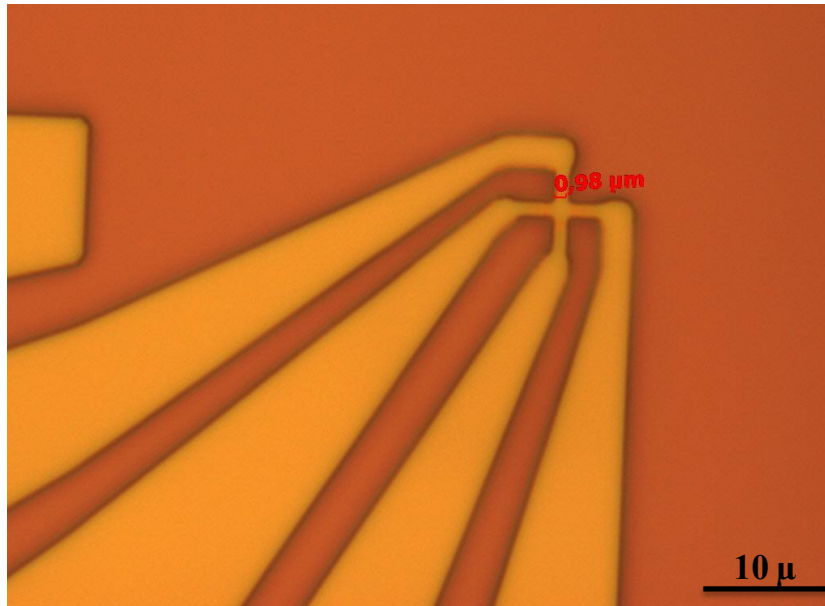


Figure 4.3: Process flow of the photolithography for both negative and positive resist.

AZ 5214E is preferred during all photolithography steps of hall sensor fabrication due to its numerous advantages. It is an image reversal resist which means that even though it is a positive tone resist, it enables to produce negative tone images. For this purpose, after standard mask exposure, the samples are baked at a temperature above 110°C known as post bake step. Later, the samples are exposed to the UV light without physical mask. This process is called as flood exposure. Flood exposure is required minimum 150 mJ/cm^2 doses for AZ 5214E photoresist but further optimization is done by changing the exposure time. Finally, the samples are developed with a compatible developer to AZ 5214E such as AZ 726 MIF, OPD 4280 or AZ 400K. AZ 726 MIF and OPD 4280 are ready-to-use developers while AZ 400K is diluted with 1:4 ratio before use it. Our procedure to determine the development time is as follows for image reversal lithography: first we dip the sample into the developer until the designed patterns on the sample can be seen by naked eye. Then, we wait for 10 s in order to obtain better undercut profile. Development is followed by a dip in DI water in order to stop development for 15 seconds and N_2 blow-dried. Image reversal process plays an important role in the optical lithography because it generates an undercut sidewall profile which is desirable especially for lift-off process. Parameters of both positive and

image reversal process for AZ 5214E photoresist are summarized in Table 4.1 and Table 4.2 respectively.

Table 4.1: Summary of the positive lithography process parameters optimized for two different mask aligner systems are given.

	Karl Suss MA6 (1.6 mW/cm ²)	Midas / MDA-60MS (25 mW/cm ²)
Dehydration Bake	120° C for 2 minutes	120° C for 2 minutes
Spin Coating	6,000 rpm for 45 s	6,000 rpm for 45 s
Prebake	100° C for 2 minutes	105° C for 1 minutes
Exposure	120 s	2 s
Development	AZ 726 MIF: 30 s	AZ 726 MIF: 50s OPD 4280: 30 s AZ 400K/DI (1:4): 30 s

Table 4.2: Summary of image reversal process parameters optimized for two different mask aligner systems are given.

	Karl Suss MA6 (1.6 mW/cm ²)	Midas / MDA-60MS (25 mW/cm ²)
Dehydration Bake	120° C for 2 minutes	120° C for 2 minutes
Spin Coating	6,000 rpm for 45 s	6,000 rpm for 45 s
Prebake	90 ° C for 2 minutes	90 ° C for 2 minutes
Exposure	20 seconds	2 s
Post Bake	115° C for 2 minutes	115° C for 2 minutes
Flood Exposure	180 seconds	11.6 s
Development	AZ 726 MIF: 90 s	AZ 726 MIF: 25 s OPD 4280: 20 s

4.2.3 Electron Beam Lithography

EBL is a prominent tool in device fabrication since it enables to fabricate structures with feature size as small as sub-10 nm. There are several advantageous of EBL over photolithography. For instance, resolution is not diffraction limited. Besides, no physical mask is required in order to transfer pattern onto the substrate surface, which makes this technique more flexible in arbitrary pattern designing.

The most remarkable property of EBL is its capability of generating high resolution nano-patterns. In photolithography, resolution of lithography is primarily limited by wavelength and it is given by Rayleigh equation ⁴⁷:

$$R = k_1 \frac{\lambda}{N_A}. \quad (4.1)$$

where k_1 is the constant between 0.4–0.8, λ is the wavelength of radiation and N_A is the numerical aperture of exposure system ⁴⁷. As is seen from the equation 4.1, the shorter wavelength is used, the better resolution can be achieved. The shortest wavelength of light used in optical lithography is 193 nm ⁴⁸. On the other hand, de Broglie wavelength of electron is 0.0086 nm for 20 keV electron energy, which is used generally in EBL system integrated to scanning electron microscopy (SEM). This shorter wavelength enables to get around 0.52 nm atomic resolution which makes it possible to obtain nanostructures with much higher resolution when you compare to the resolution achieved in photolithography ⁴⁹. By using high energetic electron beam, wavelength of electrons can be further reduced.

Process flow of EBL resembles in many aspects to photolithography except that a focused beam of electrons is used for exposure of the resist coated substrate instead of UV light. First of all, the samples are cleaned with the standard cleaning procedure as discussed previously and the cleaned samples are covered by resist which is sensitive to electron beam by using spin coating method. As in the photolithography, there are two different classes of resists for EBL application called as positive and negative resist. Polymethyl methacrylate (PMMA) is the most widely used positive EBL resist, since it is able to produce high resolution structures and it is suitable for lift-off process. When the positive resist is exposed by the electron beam, it becomes more soluble in the

developer and exposed area can be removed from the substrate surface. PMMA with different molecular weight is commercially available. However, PMMA having molecular weight of 495 K and 950 K are extensively used in EBL application. Sensitivity and contrast of e-beam resist depend on molecular weight. The lower molecular weight means that the resist is more sensitive but has lower contrast and provides lower resolution. Beside this, generally chlorobenzene and anisole are used as a solvent of PMMA. When concentration of solvent increases, the resist becomes more viscous. The final film thickness of PMMA in chlorobenzene is a bit thicker than PMMA in anisole for the same amount of solvent concentration. In addition, anisole is less harmful to environment and human body therefore, it is more preferably. On the other hand, a focused electron beam exposure of a negative e-beam resists result in cross-linking in the polymer chain. Consequently, negative e-beam resist becomes insoluble in the developer after exposure. HSQ (Hydrogen Silsesqioxane) is the most common negative resist because of the fact that it not only offers very high resolution less than 10 nm but also it is used for etch mask because of its high resistance to chemicals⁵⁰. It can be diluted with MIBK in order to obtain resist with different concentration and thickness. HSQ as Fox 12 (Flowable Oxide) is preferred as negative e-beam resist in this work. During this work, resist having different thickness, molecular weight and tone is used according to necessity. Thickness of e-beam resist can be measured by the surface profiler by scratching the baked samples with a sharp tweezers or a scalpel. Step height measurement of the PMMA and any other resist film thickness are measured by KLA-Tencor P6 surface profiler. Spin speed is another factor which directly affects the thickness of the resist and it is decreased by increasing spin speed. After coating the samples, they are baked at a recommended temperature in order to evaporate solvent in the resist and make the resist harder. HSQ is baked at two steps: first at 150° C for 2 min subsequently, 220° C for 5 min while PMMA is baked at 180 ° C for 1 hour. The samples become ready for electron beam exposure, after spin coating and baking.

When the electron beam is passed through the e-beam resist on top of the substrate, inelastic and elastic electrons scattering take place either in the resist or in the substrate which limits the resolution of EBL. These electrons scattering result in pearl-shaped volume in the resist. The volume of the pearl-shaped depends on mainly electron energy. When electrons are more the energetic, they will penetrate deeper.

Some of the incident electrons change their direction with small angle after they collide with resist electrons. They also transfer a portion of their energy (inelastic scattering) and this is called forward scattering. On the other hand, very few of the incident electrons collide with atoms in the substrate without losing their energy (elastic scattering). If they can get back to the resist from the substrate, they expose the resist additionally. In this case, they make wide angle scattering and this is called as back scattering. Undesired exposure of the resist due to back scattering of electrons is known as proximity effect. It results in getting different structure size and shape from the actual designed pattern size. In fact, it can cause irrecoverable lift-off problem on fabricated structures. Range of proximity effect depends directly on many parameters such as: the substrate type, accelerating voltage of electrons and resist thickness. Proximity effect becomes one of the challenges which users try to overcome this problem. Various solutions are developed to minimize the proximity effect. Some of them can be listed as follows:

- Increasing acceleration voltage.
- Preferring bi-layer resist process.
- Using dose modulation program which adjust dose for particularly large area dense patterns.

After exposing the resist, development process is carried out according to the resist tone. When the positive resist is used, regions exposed to electron beam become more soluble in the developer. For PMMA being a positive resist, different ratios of Methyl Isobutyl Ketone (MIBK) and IPA mixture can be used as the developer. The best resolution is obtained with 1:3 MIBK: IPA, even though sensitivity is low at this concentration. When the negative resist is exposed with focused electron beam, as a result of cross linking reactions in the e-beam resist, irradiated areas becomes insoluble in the develop. In this study, HSQ is preferred for negative lithography application and it is developed by using TMAH based developer. EBL process flow for positive and negative resist is shown Figure 4.4.

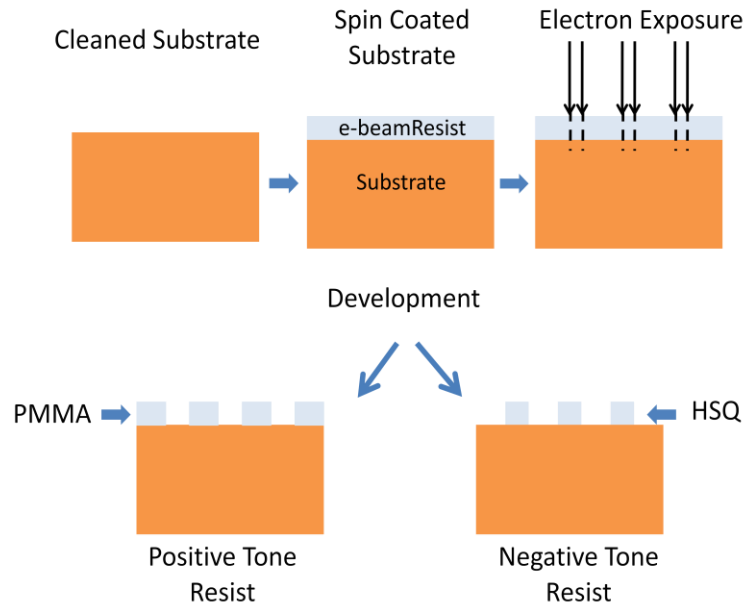


Figure 4.4: Process flow of the EBL for both negative and positive resist tone.

Well-defined undercut profile plays a major role in both photolithography and EBL particularly for lift-off process. Producing undercut profile in EBL is easier than photolithography since volume of electron interaction become larger in the deeper part of e-beam resist layer⁵¹. In EBL, the best method for this profile is achieved by bilayer lithographic process. In this process, a high molecular weight e-beam resist is spin coated on top of another e-beam resist which has lower molecular weight. As mentioned above, the resist with lower molecular weight is more sensitive and develops faster than higher molecular weight PMMA in the developer after e-beam exposure, which leads to create undercut shape. Two different recipes are used for bilayer process. In the first one, the substrate is spin coated with 495 K PMMA-C2 at 5,000 rpm (50 s) and baked at 180 ° C for 40 minutes. After the sample is cooled down, subsequently the second layer 950 K PMMA-A2 at 4,000 rpm (50 s) is coated and placed on a hot plate at 180 ° C for 40 minutes. The resist on the top is dropped to substrate when the spinner is working at very low speed (100 rpm for 2 second) in order to prevent intermixing of these two resist layers. This is the most critical step in the bilayer process as it can ruin final pattern structures. In the second recipe, PMMA and its copolymer MMA (8.5) EL11 is used in order to get undercut resist profile. In this case, in the beginning MMA is spin coated at 6,000 rpm for 45 s and baked for 5 minutes at 180° C. Later, A2 950 K PMMA-A2 is dropped the surface while spin coater is at 1,000 rpm for 4 second , as in

the previous transaction, and samples are baked for 5 minutes at 180° C. After coating is completed, the samples are developed 1:3 MIBK: IPA for 1 minute and followed by a dip IPA for 15 seconds to stop development. Finally, the samples are blow dried with N₂ and then metal evaporation can be performed. The Figure 4.5 illustrates fabrication procedure of undercut profile and lift-off process for bilayer system.

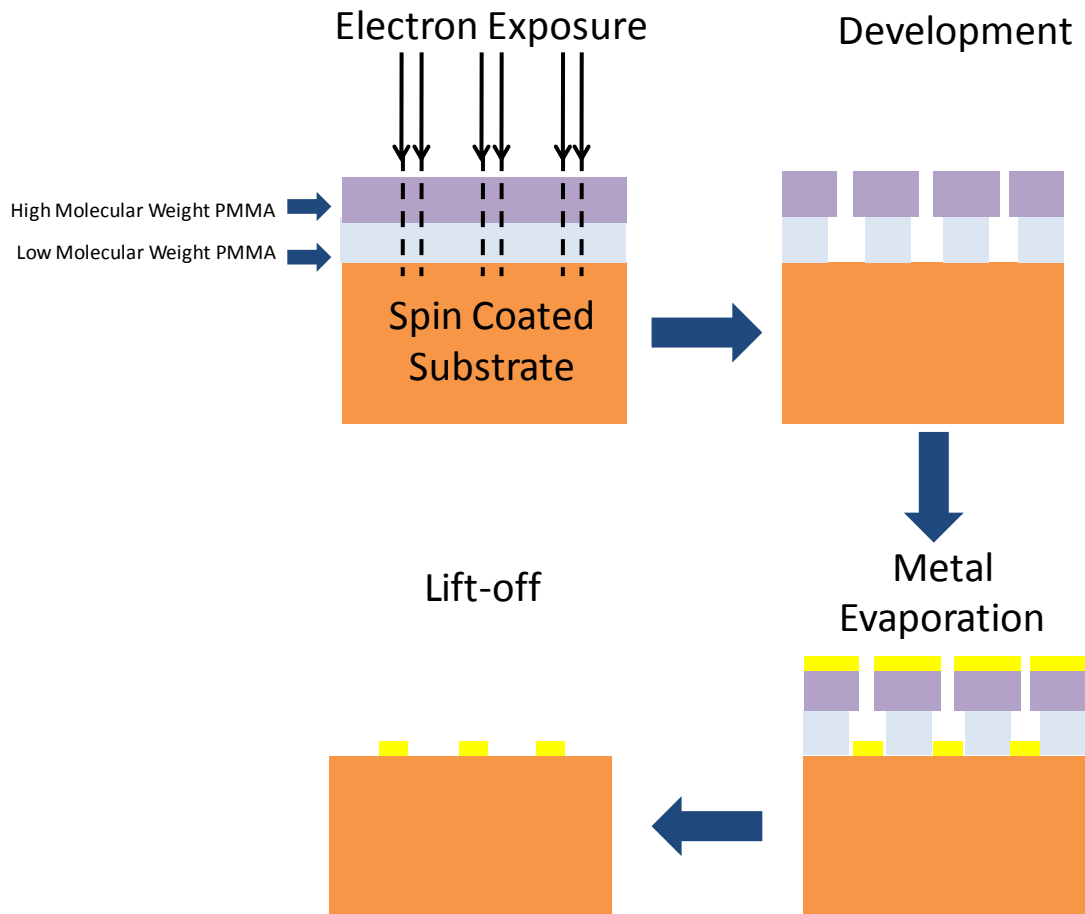


Figure 4.5: Schematic illustration of fabrication steps for bilayer system.

Exposure of the focused electron beam is the most crucial step in EBL. Electron beam exposure is performed with two different systems in this study. The first system is Nabyty Pattern Generation System (NPGS) which is integrated to field-emission SEM (Zeiss Leo Supra 35VP with Gemini column) located at Sabancı University. SEM machine and computer of NPGS communicate via Remcon32.exe interface software on the SEM computer. Process flow starts with spin coating independently from exposure system. Once the substrate is spin coated, resist residue on backside of the sample

should be cleaned with ACE so that the sample surface is in level as much as possible. Then, four corners of the samples are scratched by diamond scribe to obtain tiny particles on the sample surface which will be used for adjustments of focus and correction of astigmatism later. The electron beam has to be properly focused before EBL application for high resolution patterning. For this purpose, image of these small particles on the surface is initially acquired at low magnification and step by step magnification is increased up to 3,000k After all the calibration is finished, electron beam has to be moved to the center of the Faraday cup which is located on the sample holder in order to measure beam current. The gold electroplated sample holder consists of a lot of holes with 0.5 mm radius on it. Faraday cup is prepared by dripping liquid carbon paste on one out of these holes. Beam current depends directly on aperture sizes and it decreases with smaller aperture size. There are different aperture sizes ranging from 7.5 μm to 120 μm . But, only 10 μm aperture sized is used in all EBL processes. Beam current was measured around 30 pA for 30 kV and 20 pA for 15 kV EHT voltage. After measuring beam current, firstly x–y–focus should be accomplished in case there is tilt on the sample surface due to dusts on back side of the sample, inhomogeneities on resist surface etc. NPGS calculates working distance values and sent to microscope for each point on sample by using x–y–focus mode.

Prepared pattern file is inserted Run File Editor which allows defining writing conditions. Some of the parameters in the run file are as follows: center to center distance, line spacing, measure beam current, area (line or point) dose and magnification. Area dose given in the equation 4.2 is applied for filled polygon shapes for this study⁵². It is also possible to determine the entity type of the designed file in the run file editor such as array, alignment or pattern.

$$\text{Area Dose} = \frac{\text{Beam current} \times \text{Exposure Time}}{\text{Center to Center} \times \text{Line Spacing}} \quad (4.2)$$

Patterns are created according to resist tone in DesignCAD drawing program which is supplied by NPGS system. In DesignCAD program, patterns can be assigned to different layers which allow exposing the components in the same design file with different exposure parameters. It is always better to determine optimal dose for specific pattern. There are two ways to do this. In the first way, pattern is arrayed by using

DesignCAD program. Each element in the design file is assigned with different color and each color represents different exposure dose. However, when DesignCAD program was used for finding optimum dose of Hall sensor pattern (Figure 4.6 (a)), lift-off problem occurred. Figure 4.6 shows SEM image of Hall sensor after 3 nm chromium and 30 nm gold coated and lifted-off.

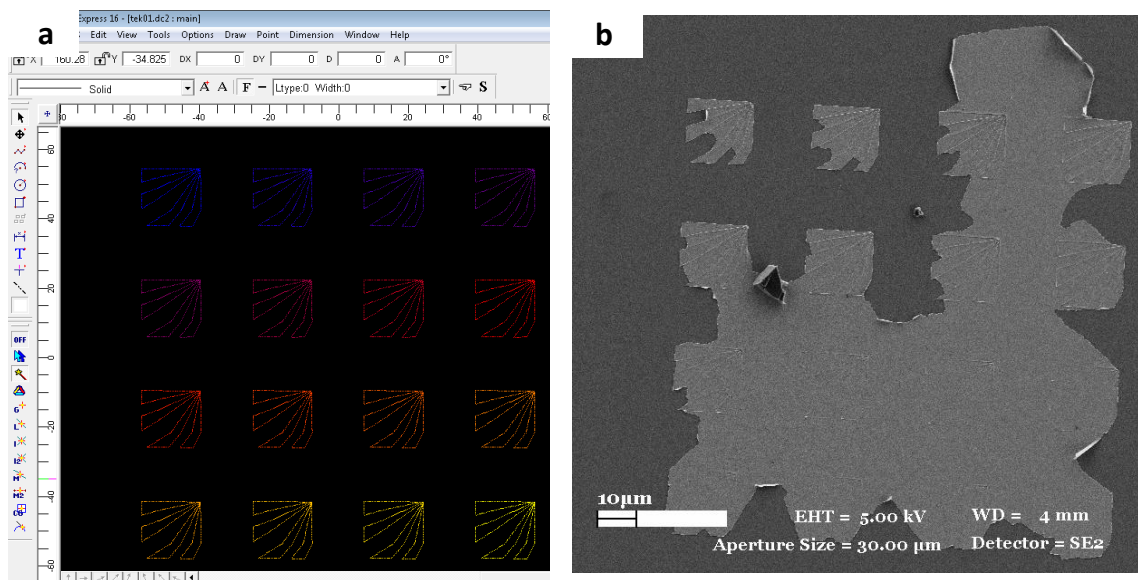


Figure 4.6: (a) Screenshot of Hall sensor array designed in DesignCAD program. (b) SEM image of hall sensor patterns after lift-off process.

Optimum dose can also be found by using array mode in Run File Editor. All parameters such as array spacing, number of rows and columns are entered in Run file Editor instead of making it in DesignCAD file. The software calculates required dwell time once beam current and exposure dose entered. In this case, designed pattern is exposed at a different dose one after another according to specified doses in editor. It is supposed that lift-off problem of Hall sensor is solved with this method due to the fact that Run File allows exposing patterns with smaller writing field and higher magnification (Figure 4.7 (a)). Applied exposure dose varies from $150 \mu\text{C}/\text{cm}^2$ to $550 \mu\text{C}/\text{cm}^2$ in this test and optimum dose for 100 nm Hall cross sized sensor is determined as approximately $230 \mu\text{C}/\text{cm}^2$ according to SEM image (Figure 4.7 (b)). As is seen from this image, although we overcome the lift-off problem, we came up with the difficulty of discontinuity at two junction legs on hall cross area. This problem is resolved by dividing Hall cross pattern into two parts as shown in Figure 4.8 (a). Since

Hall cross area has smaller feature and delicate, first Hall cross part is exposed and then legs of Hall sensor is exposed to electron beam separately. 200 nm overlap between Hall cross and legs was sufficient for desired design. SEM image of fabricated Hall sensor designed according to this is given in Figure 4.8 (b).

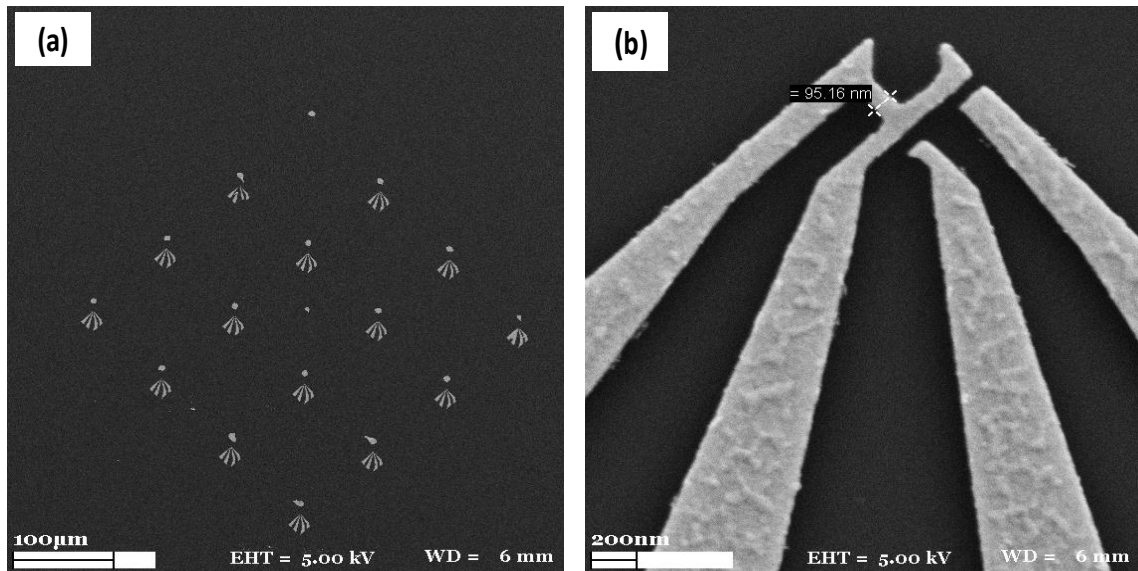


Figure 4.7: (a) SEM image of hall sensor patterns arrayed by Run File Editor (b) after lift-off process.

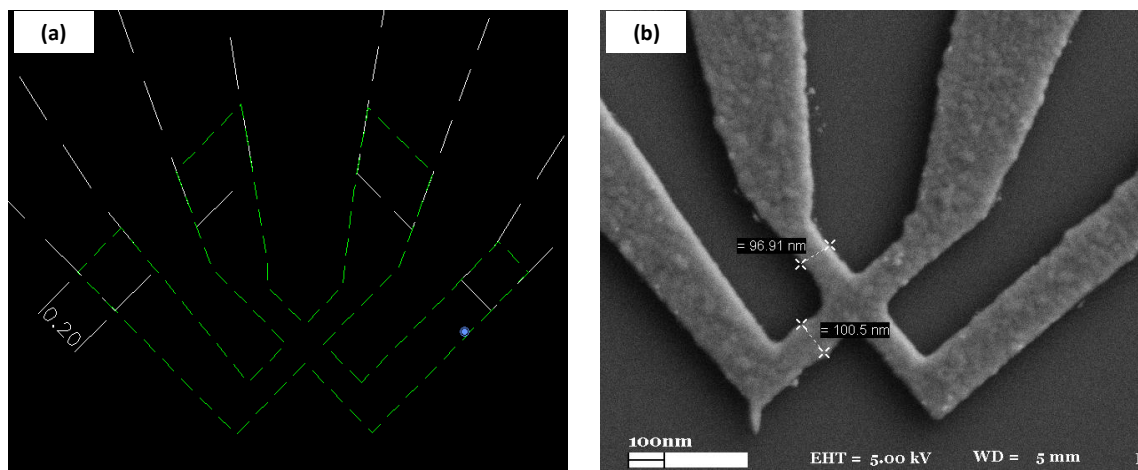


Figure 4.8: (a) Screenshot of 100 nm Hall sensor designed in DesignCAD program (b) SEM image of fabricated 100nm Hall sensor pattern.

Although NPGS is capable to produce various patterns with different electron energy and aperture sizes, there exist some restrictions in this system. One of them is that, specimen current is relatively low because of low high extra high tension (EHT) voltage, which causes longer exposure time. Also, alignment process takes considerable amount of time, since it is done one at a time manually. In addition to this, there is no proximity effect correction (PEC) algorithm embedded on the system. Therefore, proximity effect is a limiting factor for densely packed patterns. Advanced EBL systems may overcome these problems successfully. In this study, we have also used dedicated EBL instrument (EBPG 5000+ ES from Vistec). This system is superior to EBL integrated to SEM in many aspects. For instance; it has laser interferometer stage which provides very fast movement with high field stitching accuracy (± 15 nm at 100 μm .) Also, range of beam currents is not limited as in the case of SEM converted system. EBPG system offers successfully working beam current varies from 50 pA up to 150 nA, which is measured Faraday cup placed on substrate holder. Therefore, writing time can be reduced by using high beam current for large area patterns and low specimen current can be preferred for structures with smaller feature sizes to obtain higher resolution as spot size (diameter of electron beam) decreased. Although, this system can be operated with 50 keV and 100 keV electron beam energy, exposure with this machine was performed at 100 keV with several different doses. Moreover, it is possible to manufacture photomasks with this system since it provides not only high beam currents but also it is equipped with 5 inch mask holder.

AutoCAD program is preferred for pattern generation although patterns to be fabricated can be designed by various drawing software programs. Once design file is prepared, LayoutBEAMER supplied by GenISys is used to convert this file into a readable format in Vistec machine. It is user friendly software which allows not only fracturing patterns into subfield and but also editing designed file by rotating, extracting layers, biasing patterns, reversing tone etc. Converted file is loaded a graphical user interface called CJOB supplied by EBPG5000+ system. By using CJOB interface, one can set exposure dose, make array of designed patterns, define identifier and alignment marker etc.

One of the primary factors which significantly affect resolution of fabricated structure in EBL process is proximity effect. As it is mentioned above, using high EHT

voltage and PEC can minimize this problem. Particularly, densely packed patterns are suffering from proximity effect. PEC is provided by LayoutBEAMER program in Vistec machine. In this program, a computational technique called Monte Carlo simulation which models electron beam and substrate interaction is used. Monte Carlo simulation generates not only trajectory of each electron when electron beam penetrates a solid according to material type, thickness and electron energy but also calculates point spread function (PSF). Psf file generated for specific resist thickness, substrate type and electron energy are inserted in LayouBEAMER program for each pattern. Figure 4.9 (a) shows the optical microscope image of Hall sensor pattern (50 nm Hall cross size) after the sample developed without implementing PEC. The EBL parameters used in this work were 180 pA beam current, 1 nm step size and $750 \mu\text{C}/\text{cm}^2$ exposure dose (same dose is applied for whole pattern). It is clearly seen from this figure, regions between pads of Hall sensor are also reluctantly exposed which can cause shortcut problem after metallization, while tip of pattern seems properly exposed according to color contrast of the image. This problem is corrected by using PEC function. Hall cross pattern implemented by PEC is shown in figure 4.9 (b). Color scale shows dose factor of the layout and it varies from 0.5 to 2 for this layout. According to simulation, dose increases at the edge of pattern.

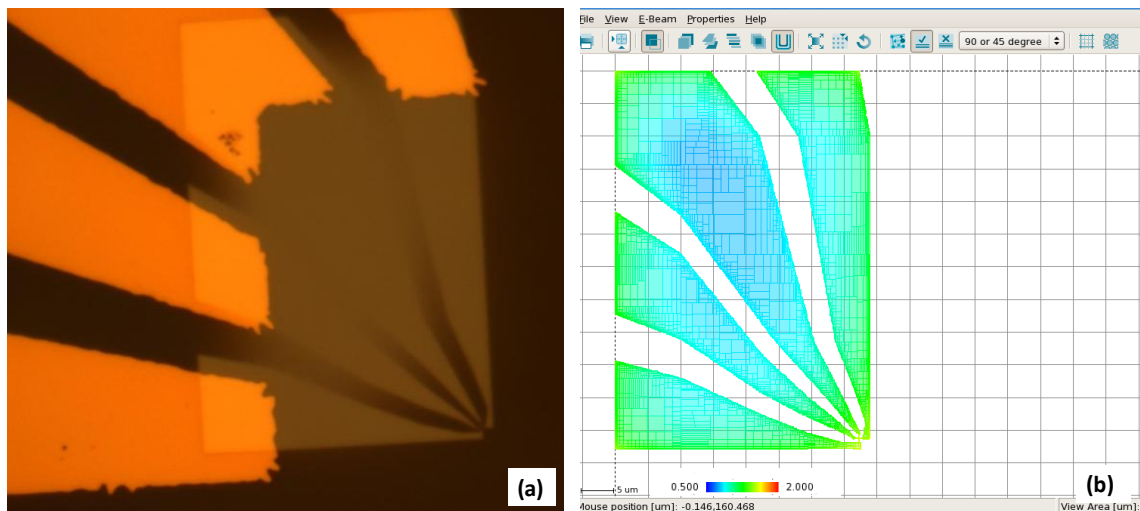


Figure 4.9: (a) The optical microscope image of 50 nm Hall sensor after development
(b) Simulation of Hall cross pattern after implemented by PEC.

Determining optimum dose for each pattern is required for also this system in order to obtain correct sized pattern without having any lift-off problem. For this purpose, we initially performed dose array which varies from $300 \mu\text{C}/\text{cm}^2$ to $1200 \mu\text{C}/\text{cm}^2$. From this test result, it is found that $800 \mu\text{C}/\text{cm}^2$ exposure dose was the closest value to get desired size. The SEM images of 50 nm Hall sensor at different magnifications after 5nm Cr/30 nm Au evaporation and lift-off in acetone are presented in Figure 4.10 (a) and (b). $500 \mu\text{C}/\text{cm}^2$ is used as base dose in this sample so that Hall cross area is exposed with around $800 \mu\text{C}/\text{cm}^2$ according to PEC simulation. Minimum Hall cross sized obtained with Vistec machine by using 950 K PMMA-C2 (100 nm thickness) was around 20 nm which is shown in Figure 4.11. Thinner resist could further reduce cross size.

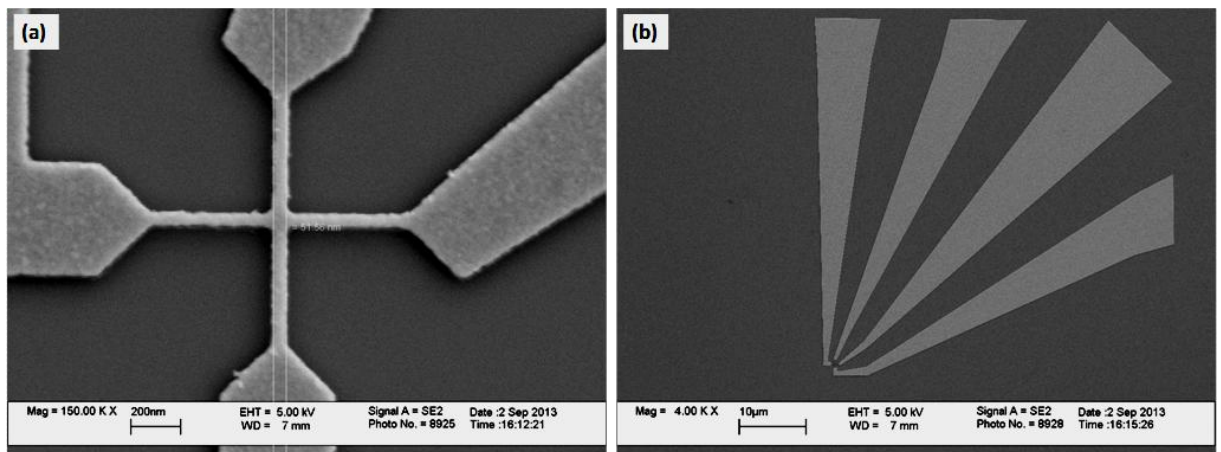


Figure 4.10: (a) and (b) the SEM images of 50 nm Hall sensor at different magnifications after 5nm Cr/30 nm Au evaporation and lift-off in acetone.

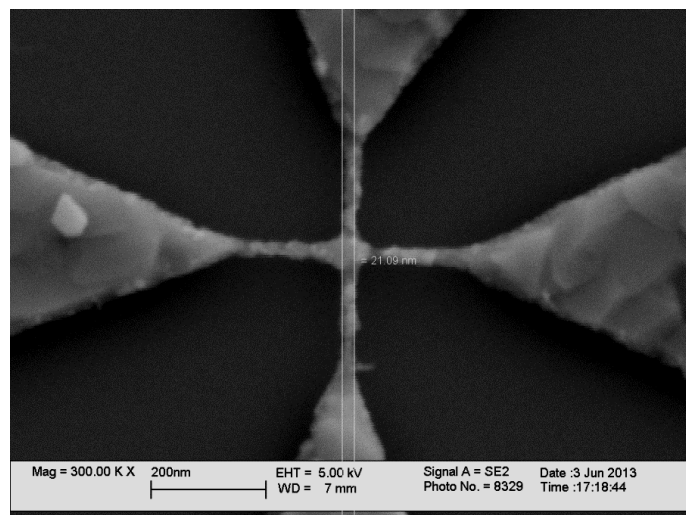


Figure 4.11: The SEM image of 21 nm sized Hall cross by using 950 K PMMA–C2.

Last but not least, alignment procedure is easier in Vistec machine than EBL system based on SEM. In this case, only three alignment markers are used for entire sample which significantly shorten alignment process time to a few minutes. Moreover, focus adjustment and astigmatism correction is not necessary and this makes the system easy to use.

Although it has several advantageous over photolithography, there are also some drawbacks of EBL. One of them is that they are high costly machines and maintenance is required regularly. Besides, evaporated film thickness must be thirty percent less than resist thickness which also limits application fields, since. In addition to this, proximity effect limits to obtain high resolution structure though there exists some solution to avoid it.

4.2.4 Etching Process

Etching process is frequently used micro/nanofabrication for removal of intended material. There are many fundamental parameters which should be taken into account for all etching process such as selectivity, uniformity, reproducibility, etching direction and etch rates. One of the most important parameter is etching profile. In isotropic etching, etching rates is same for all direction while horizontal etching rate and vertical etching rate are different to each other in anisotropic etching. Besides, etch rates should be determined before etching real samples in order to prevent over etching since it is irreversible process. Each material has different etching ratio for different etcher. This is called selectivity and generally highly selective etcher is preferred in order to obtain desired structures properly. Both dry etching and wet etching are used during fabrication of Hall sensor according to necessity. In the next subsection, detail of etching methods and recipes used in this study will be explained.

4.2.4.1 Wet etching

Wet etching is a liquid based etching method as name referred and it involves chemical reaction between solution and material to be etched. It gives generally isotropic profile with some exceptions. It is preferred frequently since it provides high selectivity and reproducibility. In addition, it is an inexpensive and simple technique compared to dry etching.

Hall sensor fabrication begins with cleaning of the substrates and recess etch. Recess etch is required in order to prevent shortcut between electrical connections of sensor and sample while the sensor is scanning the sample surface. For this purpose, end of contact pads are etched around 50–60 μm deep before contact pad formation. This step is very critical, since if undercut profile occur during optical lithography, this can cause discontinuity in contact pads. In this work, semi-insulating GaAs used as substrate is etched for recess formation. The sample is first spin coated with AZ 5214E by spinning 4,000 rpm for 40 s, which provides around 1.5 μm resist thickness. Then, prebake is done at 105 ° C for 1 minute. The sample is illuminated for 2 seconds by using Midas mask-aligner system and after exposure, development is performed by AZ 726 MIF for 50s. Developed samples are rinsed in DI water for a longer time in this case. Because of the fact that developer is a basic solution and if developer residue remains on the sample surface, after dipping in an acid solution, this creates salt on the sample surface which cannot be removed occasionally. Then samples are baked at 120 ° C for 2 minutes for hard bake process. Hard baking step also plays critical role for this progress, since it improves adhesion resist to substrate surface and makes resist more durable in chemical solution. Finally the sample is immersed in HCl:H₂O₂:H₂O solution at volume ratios of 4:7:55. Etch rate with this recipe is found as approximately 1 $\mu\text{m}/\text{minute}$. However, it is also observed that, etch rate decreases with passing time. Light microscope image of etched sample by using this recipe is given in Figure 4.12 (a) and (b) and etching profile is shown in Figure 4.12 (c) and (d).

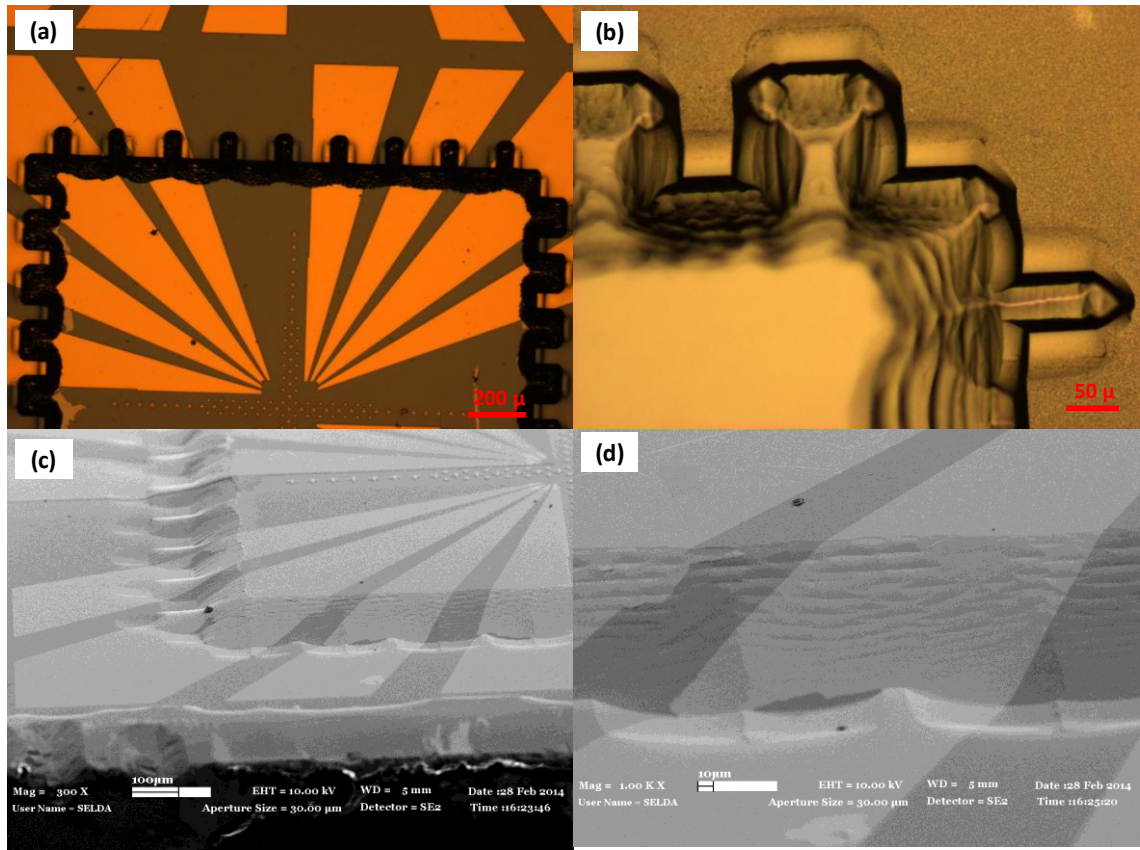


Figure 4.12: (a), (b) The optical microscope and (c), (d) the SEM images of recess formation.

Wet etching is also used in mesa step formation for fabrication of Hall sensor. It is necessary in order to bring tip of the sensor the closest to the sample surface. In this case, slow etch rate is required since 1.5–2 μm deep etching is fairly enough for our purpose. EBL is implemented for patterning, just because it ensures higher alignment accuracy than photolithography. We performed two different recipes. For the first one, 950 K PMMA–C2 which has 100 nm resist thickness by spinning 6,000 rpm for 45 s is used. Even though hard bake at is applied after EBL, all resist on the sample surface has been removed before desired etch thickness is achieved. This problem is solved by using bilayer process. The sample is spin coated by 950 K PMMA–A2 and its copolymer MMA (8.5) EL11 as explained in the previous section, which gives approximately 550 μm resist thickness. Next, the sample is exposed with 550 $\mu\text{C}/\text{cm}^2$ base dose by using PEC function. After development with 1:3 MIBK:IPA solution for 60 s, the sample is baked at 100 $^{\circ}\text{C}$ (post bake). Then, the sample is immersed in $\text{H}_2\text{S}_4\text{O}_4:\text{H}_2\text{O}_2:\text{H}_2\text{O}$ solution at volume ratios of 1:8:40 for 60 s, which gives around 1.5

μm etch thickness. Mesa step is generally done after Hall sensor pattern is defined, because it causes non-uniform resist coating for the next lithography steps if it is done beforehand. The SEM image of mesa formation performed by this recipe is shown in Figure 4.13. Dry etching is also implemented for mesa formation, but applications of dry etch decrease production yields of fabricated sensors which will be discussed in the next section.

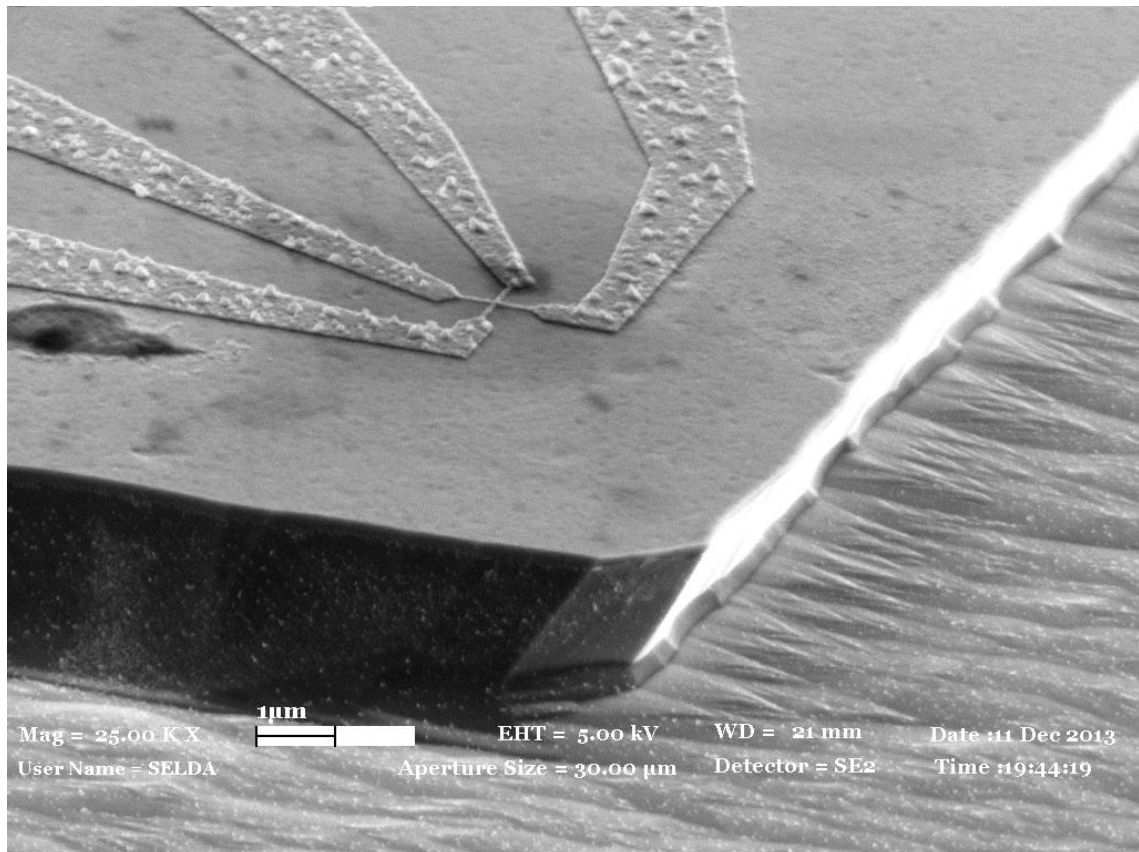


Figure 4.13: SEM image of mesa formation on Bismuth Hall sensor.

4.2.4.2 Dry etching

Dry etching is chemical or physical process where ions in gas introduced to the chamber interacts with a substrate to be etched⁵³. Both isotropic and anisotropic profile can be obtained with this method. Besides, etch profile and etch rate can be controlled by changing pressure, temperature, applied power and ratios of gas. Dry etching can be classified into three groups; physical etching, chemical etching and physical chemical

etching. In physical dry etch, highly energetic ions knock out atoms from sample surface. In chemical dry etch, chemical reactions result in etching.

There are two different reactive ion etching (RIE) systems available in SUNUM facility: chlorine based and fluorine based. F-based system is used for both oxygen plasma and SiO₂/Si etching. It is equipped with gas cylinder of O₂, C₄F₈, Ar and Sf₆. Oxygen plasma removes organic materials from the sample surface by chemical reaction and it is used in Hall sensor fabrication for several purposes. In Graphene Hall probe (GHP) fabrication, after Hall cross pattern is defined by positive optical lithography or EBL, oxygen plasma is used to etch unprotected graphene region with resist in order to pattern graphene layer. The process parameters are 20 sccm O₂ flow, in a 100 W RIE power, 37.5 mTorr pressure. It is determined that 9 second completely removes single-layer graphene by using given recipe. If oxygen plasma is applied longer than this length of time, it can also etch not only side wall of resist, since resist is also an organic material, but also graphene itself which results obtaining smaller pattern size than desired. Furthermore, oxygen plasma is also indispensable for Bismuth Hall sensor fabrication. In conventional Hall sensor fabrication, Hall cross is defined after a number of lithography steps, which leaves a few nm resist residue on the sample surface. Therefore, resist residue causes adhesion problem particularly for smaller size Hall sensor. We resolved this problem by applying oxygen plasma before spin coating with e-beam resist. Figure 4.14 (a) presents Bismuth Hall sensor which has not been applied oxygen plasma before spin coating with e-beam resist. As it is seen from the figure, there is no Hall cross defined by EBL due to adhesion problem whereas applying oxygen plasma before spin coating overcame this problem shown in Figure 4.14 (b).

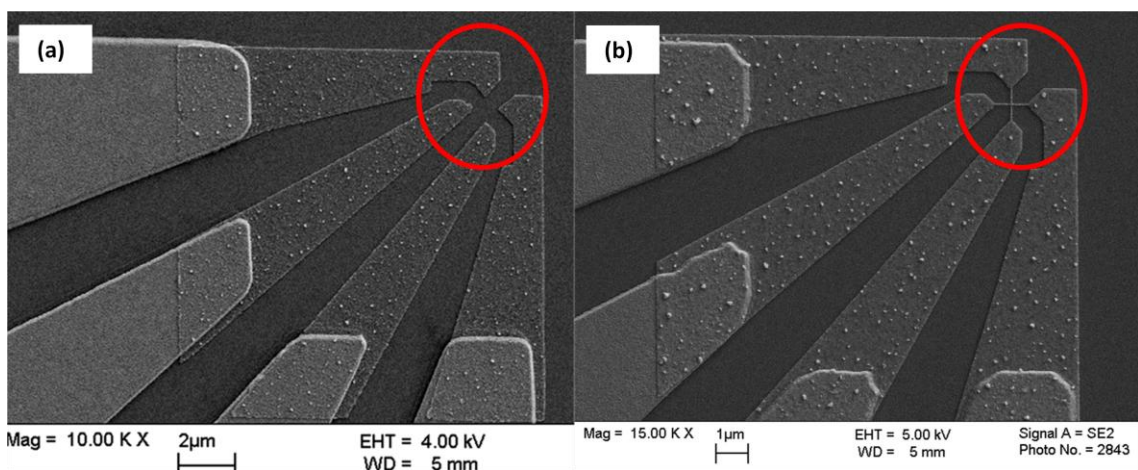


Figure 4.14: (a) and (b) SEM image of Bismuth Hall sensor without and with oxygen plasma application before e-beam resist coating respectively.

Oxygen plasma is also used for enhancing adhesion of contact pads to the substrate surface. For this purpose, after contact pads formation by photolithography, oxygen plasma is implemented for 8–9 s by provided recipe before metal evaporation. This step particularly plays very critical role in wire bonding of both GHP and Bismuth hall sensor.

F-based system is used also SiO_2/Si etching. The mesa which serves as AFM tip was obtained in GHP by etching SiO_2/Si wafer around 830 nm. 285 nm of SiO_2 layer was etched with $\text{C}_4\text{F}_8/\text{O}_2$: 50/5 sccm; ICP power: 1,750 W; RIE power: 100 W; pressure: 7 mTorr for 45 s and this is followed by 545 nm Si was etched with $\text{C}_4\text{F}_8/\text{SF}_6$:45/25sccm; ICP power: 1500 W; RIE power: 35 W; pressure: 15 mTorr for 3 minutes (Figure 4.15). After plasma etching, photoresist on the sample surface is removed with ACE and followed by N_2 blow dry. If there is still resist residue left on the sample surface, the sample can be immersed in AZ-100 remover which strips resist residue by either leaving it in this solution for one day at room temperature or 10 minutes at 80°C .

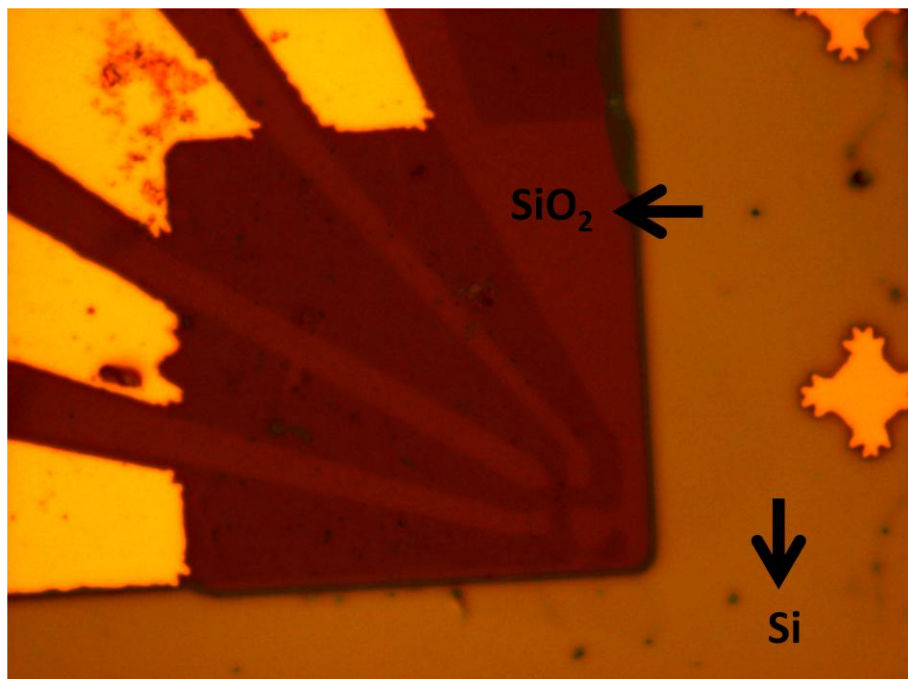


Figure 4.15: The optical microscope image of GHP after mesa formation.

In the early stage of this work, mesa step of Bismuth Hall sensor fabricated on GaAs substrate is performed by using RIE system located in Advanced Research Laboratory's clean room at Bilkent University. Process parameters are 25 sccm CCl_2F_2 flow, in a 100 W RF power and 0.4 mBar pressure for 15 minutes. The Figure 4.16 shows the (a) top view and (b) tilted SEM images of a Bismuth Hall sensor whose mesa step is performed by given recipe. As seen from these images, after resist removed from the sample by dipping it in ACE, Bismuth grains on Hall cross area are also peeled off which is observed almost all die and causes a big connection problem. In addition, photoresist residues remained on the surface particularly, near edge of the chip which significantly affects performance of Hall sensor. Then, Cl based RIE system which is located in SUNUM and is equipped with gas cylinder of BCl_3 , Cl_2 and Ar are used for same purpose. Process parameters are 30 sccm BCl_3 and 50 sccm Cl_2 flow, in a 100 W RF power, 800 W ICP power and 7 mTorr pressure. 45 seconds etch is performed in order to etch $1.5 \mu\text{m}$ GaAs (Figure 4.16 (c) and (d)). Although successful etching is performed with this recipe, since gas line of BCl_3 is easily clogged, we decided using wet etching for this step.

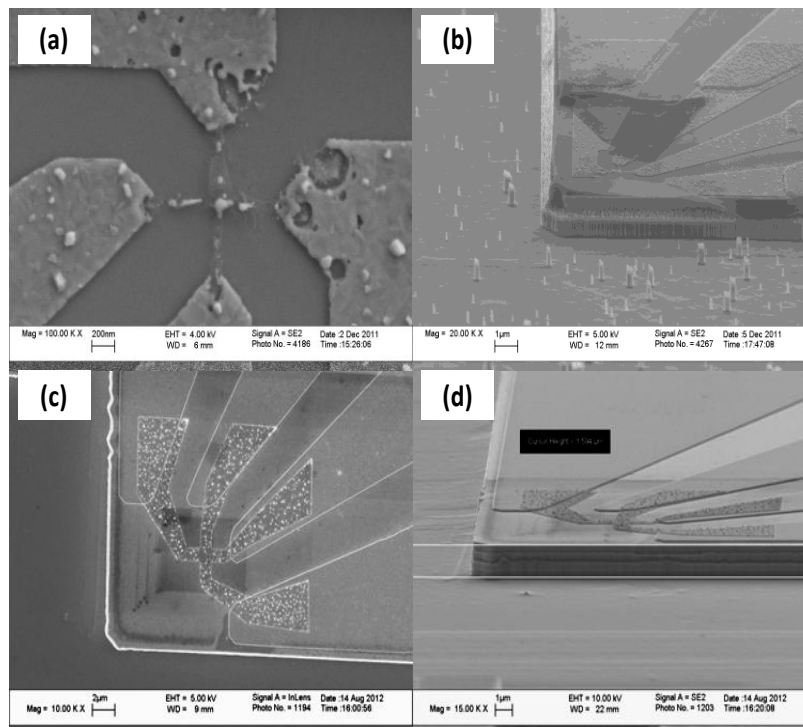


Figure 4.16: The SEM images of Bismuth Hall sensor after mesa formation.

4.2.5 Thermal Evaporation

Thermal evaporation is one of the most widely used for metal deposition in device fabrication. In this method, source material to be deposited is heated until it is evaporated or sublimated by applying high current under vacuum condition. In this study, two different box coaters are used. The first one is supplied by Nanovak and it is used for evaporation of Au, Cr, Ti and Bi. The second evaporation system is supplied by Torr International which is equipped with both e-beam and thermal evaporator part. In e-beam evaporation, high energetic electron beam cause evaporation of the source material to be deposited. One of the advantages of e-beam evaporation over thermal evaporation is that e-beam heats only the source material and this results obtaining thin film with higher purity.

In the fabrication of Hall sensor, after contacts pads which provides electrical connection from Hall cross area are patterned by image reversal optical lithography, 10 nm Cr and 200 nm Au are evaporated to the sample surface for metallization of contact pads of both GHP and Bismuth Hall probe. Next, the sample is immersed in ACE for lift-off process. Since adhesion of Au to the substrate surface is quite poor, Cr or Ti are used before Au evaporation as an adhesion layer. Otherwise, Au can peel off easily from the sample surface. Deposition rate during evaporation of contact pads is around 1 A/s for Cr while it is 5 A/s for Au. Besides, evaporation of Bismuth pellets used as Hall sensor material is performed at very slow evaporation rate approximately 0.1–0.2 A/s. Since surface of Bismuth pieces is oxidized quickly, Bismuth pellets are immersed 1:5 ratio of HCl : DI water solution in volume for 5 minutes before evaporation. In addition to this, we have not used Cr as adhesion layer for Bismuth evaporation. The SEM images of 50 nm Bismuth Hall sensor (a) with and (b) without Cr used as adhesion layer are given in Figure 4.17. As is seen from these figures, evaporation of Cr before Bismuth makes grain size of Bismuth much larger. It is also observed that even though EBL parameters are exactly same for both samples, size of Hall cross is around 20 nm

bigger when Cr is used before Bismuth evaporation. Therefore, we preferred to not to use adhesion layer for Bismuth Hall sensor.

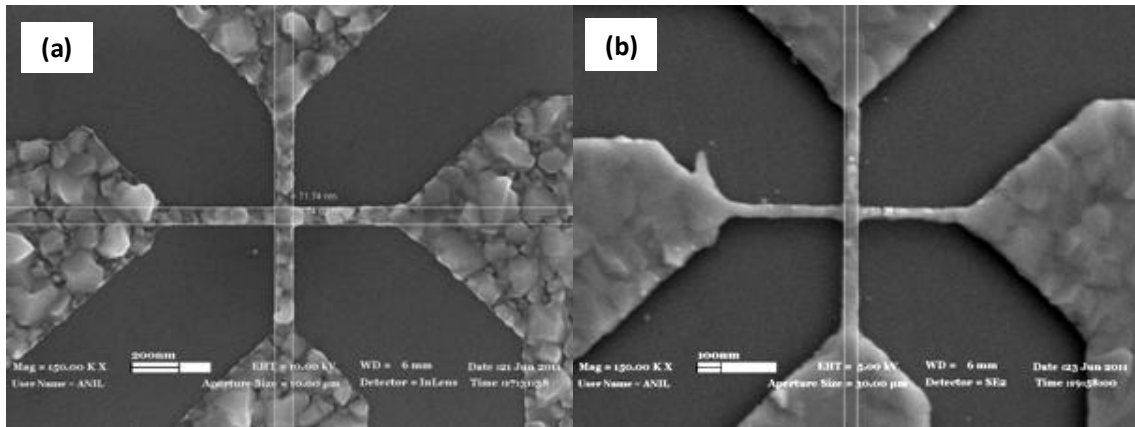


Figure 4.17: The SEM images of 50 nm Bismuth Hall sensor (a) with and (b) without evaporation of Cr as adhesion layer before Bismuth metal.

4.2.6 Dicing and Wire Bonding

Wafer to be used in device fabrication is cut by a scribe into pieces whereas once mesa formation of the samples is completed; the sample is diced into 64 pieces by automatic dicing saw supplied by Disco. Since distance between the sensors have been designed on mask to be 100 μ , it is compulsory to use dicer at the last step. Dicing blade is selected specifically for our mask design and substrate type used in device fabrication. Blade with 25–35 μ m kerf width which is thickness of the slot on the sample after dicing process is used in order to increase production yield of Hall devices. However, it is observed that after prolonged usage, kerf width becomes thicker (up to 70 μ , after 15–20 usage)

Dicing step starts with spin coating of the sample with AZ 5214E photoresist in order to protect devices from debris arising during cutting process and the sample is baked at 80° C on a hot plate to harden photoresist. Process parameters of dicing were same for both GHP and Bismuth Hall probe except feed speed. Feed speed for GaAs substrate has to be as much as slow and it was set 0.1 mm/ sn in order to decrease chipping defects whereas feed speed was set to 1 mm/s for SiO₂/Si substrate. The Figure 4.18 shows diced Bismuth Hall sensor fabricated on GaAs substrate.



Figure 4.18: Diced Bismuth Hall sensor fabricated on GaAs substrate

After dicing, resistance of each sensor is measured individually by using multimeter in the probe station (Cascade Microtech PM5 Probe Station). Then, sensors with resistance in the range of $k\Omega$ are selected and glued on top of QTF as is mentioned previously. Next, electrical connections from sensor to PCB are provided by Kulicke and Soffa wire bonder. Though it provides both ball and wedge bonding, wedge bonding is performed to take electrical connections from contact pads of Hall sensor to the pads of PCB with $25\ \mu\text{m}$ Au gold wire. The SEM image of diced and bonded Bismuth Hall sensor is given in Figure 4.19.

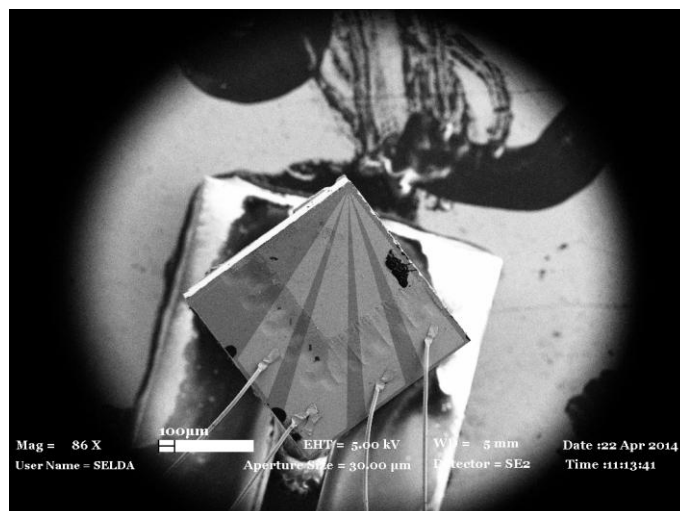


Figure 4.19: The SEM image of diced and bonded Bismuth Hall sensor.

CHAPTER 5

GRAPHENE HALL SENSOR for SHPM

5.1 Introduction

Scanning hall probe microscopy (SHPM) belongs to scanning probe microscope (SPM) family, which provides quantitative and non-invasive local magnetic field imaging of magnetic and superconducting materials⁵⁴. It provides high magnetic field and spatial resolution, simultaneously with the topography of the sample surface^{55, 9}. The most important element of SHPM is the Hall sensor which is sensitive to the perpendicular component of the magnetic field on the specimen. Hall sensors can be fabricated from various materials such as GaAs/AlGaAs heterostructure, Bi, InSb and graphene. GaAs/AlGaAs two-dimensional electron gas heterostructure is one of the most popular materials for Hall probe production. Even though it has high mobility which increases Hall coefficient, the minimum cross size is limited with this sensor because of surface depletion effect, which results in low spatial resolution⁵⁶. It is reported that GaAs/AlGaAs Hall sensor with 250 nm cross sized fabricated by implementing EBL has very high resistance which does not allow driving current at room temperature⁵⁷. In Bismuth Hall probes, the spatial resolution was decreased up to 50 nm, on the other hand minimum detectable magnetic field was increased due to low mobility of Bismuth film⁹. In order to overcome this problem, InSb has been used as sensing element. It has high mobility (55,500 cm²/Vs) at room temperature and low carrier concentration. It was reported that minimum detectable magnetic field was 6–10 mG/ $\sqrt{\text{Hz}}$ at 50 μA drive current in InSb Hall sensor with a size of 1.5 μm^2 .

After the discovery of high mobility in graphene, it is also considered to be a good candidate for Hall probe material ^{58, 59}. It has been demonstrated that minimum detectable magnetic field (B_{\min}) of epitaxial graphene Hall sensors was $3.9 \mu\text{T}\sqrt{\text{Hz}}$ which is better than with same sized InSb and CVD graphene Hall sensors. In table 5.1, some of data taken from InSb, epitaxial graphene and CVD graphene sensors are given for $5.0 \mu\text{m}$ Hall cross sized ⁷. They also demonstrated size dependency of B_{\min} and Hall coefficient (R_H) for epitaxial graphene Hall sensor and according to their results, B_{\min} increases exponentially with descending cross size for the same driven current applied ($I_{\text{Bias}}=10 \mu\text{A}$).

Table 5.1: Summary of data measured from InSb, epitaxial graphene and CVD graphene sensor for $5 \mu\text{m}$ Hall cross size ⁷.

	InSb Device	Epitaxial Graphene Device	CVD Graphene Device
R (kΩ)	12	22	100
R_H (Ω/T)	974	711	310
μ_c (cm²/Vs)	8322	2643	–
B_{min} ($\mu\text{T}\sqrt{\text{Hz}}$)	6.5 ($I_{\text{Bias}}=10 \mu\text{A}$)	3.9 ($I_{\text{Bias}}=10 \mu\text{A}$)	43.0 ($I_{\text{Bias}}=3 \mu\text{A}$)
S_n (nV/$\sqrt{\text{Hz}}$)	55.3 ($I_{\text{Bias}}=0 \mu\text{A}$)	19.9 ($I_{\text{Bias}}=0 \mu\text{A}$)	–

Materials used in Hall sensor fabrication are selected according to its electronic properties and ease to manufacture. For example; material having low carrier density results in obtaining higher Hall coefficient and thereby provides better field sensitivity. In graphene, carrier concentration decreases as Fermi level of graphene is brought to closer Dirac point by applying gate voltage. Tang *et. al* produced $5 \mu\text{m}$ sized Hall probes from CVD graphene and showed that Hall coefficient initially decreases when gate voltage is very close to Dirac point, then it starts to increase when it is moved away from Dirac point ⁶⁰. Therefore, as in the other areas, it has been a promising material for Hall probes in SHPM applications thanks to its commensurable

characteristics to conventional Hall Probes. However, utilization of GHP for magnetic imaging has not been shown in the literature yet.

In this chapter, we represent fabrication, characterization and performance of graphene based micro–Hall devices for Low Temperature Scanning Hall Probe Microscopy (LT–SHPM). Graphene produced by CVD method was preferred in order to increase the production yield of the fabricated Hall sensors. In this work, for the first time, we used GHP integrated with QTF for imaging localized magnetic field of NdFeB in a wide temperature range of 3–300K. This study is published as “Single Layer Graphene Hall Sensors for Scanning Hall Probe Microscopy (SHPM) in 3–300 K Temperature Range” S. Sonusen, O. Karci, M. Dede, S. Aksoy, and A. Oral, Applied Surface Science **308**, 414–418 (2014) ⁶¹.

5.2 Mechanic and Electronic Properties of Graphene

Graphene is a mono layer of sp^2 bonded carbon atoms packed into a two–dimensional (2D) honeycomb lattice. In graphene, zero band gap semiconductors also known as semi–metal, conduction and valance bands meet at a point called as Dirac point in which density of states is zero in an ideal graphene (Figure 5.1) ⁶². Furthermore, in graphene both electrons and holes have a linear energy–momentum relationship and it is given by ⁶³:

$$E = \pm | \hbar k | V_f \quad (5.1)$$

In this equation, V_f is Fermi velocity which is approximately 1.10^6 m/s ($V_f \cong c/300$) and positive sign represents electrons in this equation whereas negative sign corresponds to holes ⁶⁴. This linear energy–momentum dispersion relation enables us to describe charge carriers in graphene as massless Dirac fermions ⁶⁵.

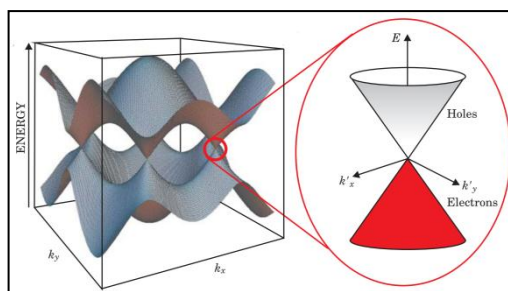


Figure 5.1: The energy dispersion of graphene and the Dirac cone ⁶².

One of the most striking properties of graphene is that it has very high carrier mobility even at room temperature due to zero effective mass of its charge carriers ⁶⁶. This property makes graphene promising material for electronic devices such as field effect transistor (FET) ⁶⁷. It was reported that mobility of mechanically exfoliated graphene on top of SiO₂ is mostly over 10,000 cm² V⁻¹ s⁻¹ at room temperature, while mobility of suspended graphene exceeded 200,000 cm² V⁻¹ s⁻¹ at low temperature ^{68,69}. ⁵⁸. Moreover, owing to high carrier mobility together with linear energy–momentum dispersion relationship, graphene permits for observation of quantum hall effect under high magnetic fields ⁶².

Graphene consists of carbon atoms arranged in a hexagonal pattern and each carbon atom has 4 valence electrons ⁷⁰. Three of these valence electrons form covalent bonds with its nearest neighbours and the fourth electron is delocalized which makes graphene conducts electricity ^{70,71}. Graphene sheets are held together by weak van der Waals force and distance between two neighbour sheets is between 3.35 Å and 3.4 Å ⁷². On the other hand, bond length for two carbons in plane is about 1.42 Å and this strong σ bonds allows graphene to exhibit superior mechanical properties ⁷¹. It is very strong material with high Young Modulus. It was reported that Young's modulus of single layer suspended graphene is 0.5 TPa whereas it is 1 TPa for graphite ⁷³.

5.3 Graphene Fabrication Methods

Since it was known that two dimensional crystals were thermodynamically unstable, it was believed that graphene didn't exist in the free state ⁶. However, graphene was first prepared via mechanical exfoliation of graphite crystals by Professor Andre

Geim's research group at the University of Manchester ⁵⁸. It has recently attracted attention of the research communities, because not only graphene has unique electrical and mechanical properties, but also the thinnest material ever fabricated

Graphene can be produced by various methods such as; mechanical exfoliation also known as mechanical cleavage, CVD, epitaxial growth, anodic bonding dry exfoliation and chemical synthesis ⁷⁴. In this study, mechanical exfoliation and CVD techniques are used.

The most popular and easiest way to produce graphene is mechanical exfoliation. It is basically repeated peeling of bulk graphite. Different sizes of graphite used during exfoliation process. However, it is observed that large-scale graphene is obtained with 3–10 mm sized graphite flake supplied by NGS Naturegraphit (India origin). Once graphite is peeled by using scotch tape, it is transferred to 285–300 nm dry chlorinated thermally grown SiO₂ on top of 500–550 μm thick Si pieces by using tweezers (Figure 5.2). Figure 5.2 (d) presents graphene sheets produced by this method.

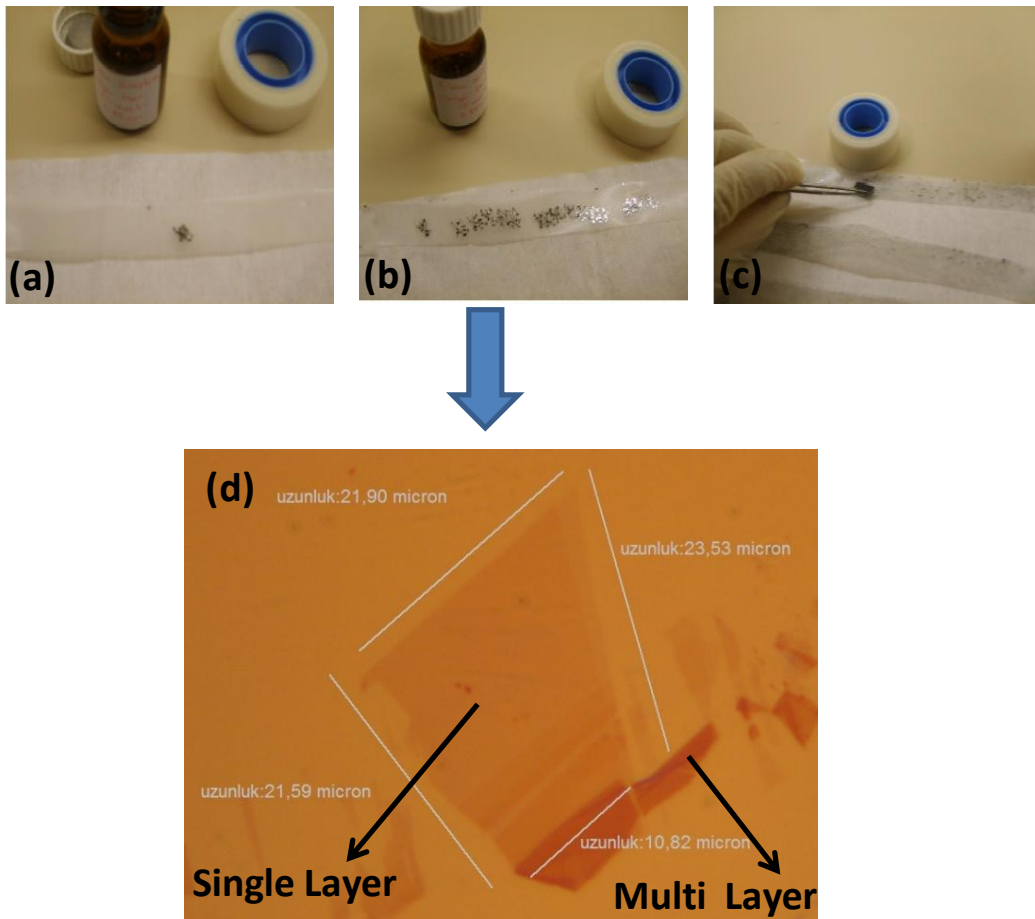


Figure 5.2: (a), (b) and (c) Graphene fabrication steps and (d) single and multi layer graphene sheets produced by this method.

Mechanical cleavage method is not only the simplest and cheapest way among the existing methods of graphene production, but also it provides obtaining graphene films with high mobility even at room temperature ⁷⁵. However, large area single crystal graphene is particularly desired for graphene based devices in order to increase yield of fabrication and this has led to development of different methods. One of them is CVD which is a promising method for production of continuous graphene film in large area. In CVD method, hydrocarbon gases such as methane (CH₄), acetylene (C₂H₂) or ethylene (C₂H₄) used as carbon source are introduced to quartz tube, either in vacuum or ambient condition, located in a furnace ⁷⁶. A transition metal such as copper, nickel or platinum is used as catalyst. When temperature is around 900°C–1100°C, hydrocarbon gases are decomposed on metal substrate, which results in formation of graphene lattice on metal substrate ⁷⁷. Once graphene is formed on the metal, graphene/metal surface is covered by protective layer (polymer). Then, the metal is etched using different etcher according to metal type. Next, floating graphene is transferred to desired substrate such as SiO₂/Si, glass or polymeric surface ⁷⁸. Finally, protective and supportive resist layer is removed from the substrate by a suitable solvent ⁷⁷. Although Cu and Ni substrate is widely used as metal substrate in CVD technique, Pt allows obtaining larger single crystal grain size than graphene grown on Cu. We used Pt as metal substrate. Experimental details of graphene growth on Pt and results will be discussed in the subsequent chapter.

Another widely used technique for large scale graphene production is epitaxial growth on silicon carbide ⁷⁹. This method includes two steps. For the first step, SiC has to be etched by hydrogen gas in order to prepare suitable SiC surface by removing scratches for epitaxial growth ⁸⁰. In this process, cleaned SiC samples are annealed in a chamber with %5 H₂ and %95 Ar gas flow. For the second step, SiC is heated in ultrahigh vacuum to temperatures around 1250–1350°C in order to sublimate Si and this results in formation of carbon rich surface ⁸¹.

5.4 Characterization Methods of Graphene

Distinguishing mono-layer and multilayer graphene, determining thickness, size and electronic properties of graphene film play very important role in fabrication of graphene based devices and their performance. There are several methods for electrical, surface morphology, optical characterization of graphene sheet such as low-energy electron diffraction (LEED), photon-electron spectroscopy, transmission electron microscope (TEM), Raman spectroscopy, optical microscopy, AFM and SEM. Among them, optical microscope is the simplest and nondestructive characterization tool. It is particularly practical for graphene films produced via mechanical exfoliation method in order to identify mono-layer and to locate graphene region for further measurement since initially entire substrate surface is scanned. Optical contrast provides to distinguish single and multi layer of graphene by naked eye under optical microscope. Blake *et al.* reported contrast dependency of graphene with respect to SiO₂ thickness and wavelength of light (Figure 5.3) by Fresnel diffraction law⁸². According to their result, contrast can be maximized by selecting specific SiO₂ thickness and using suitable filtering. Besides, the best visibility of graphene film on 280–300 nm SiO₂ thickness is provided by green light illumination as seen from Figure 5.3⁸².

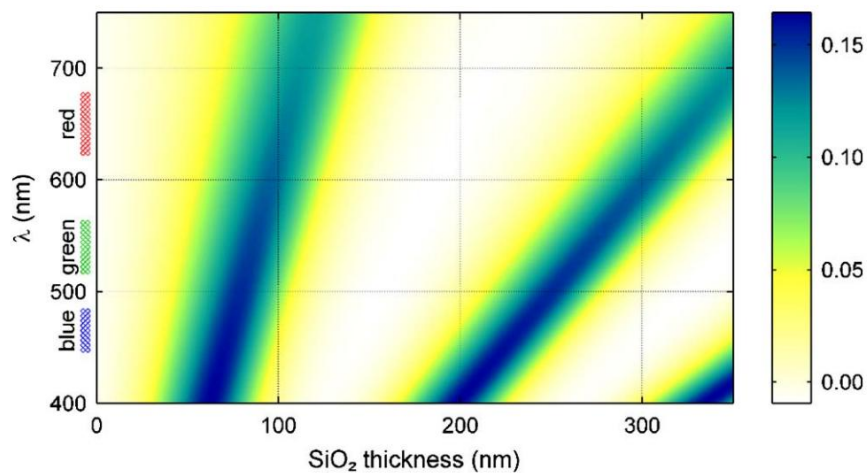


Figure 5.3: Optical contrast variation of graphene with changes in SiO₂ thickness and of wavelength of light⁸².

Even though optical microscope is the easiest way, it is not quantitative method. Raman spectroscopy is a powerful technique which provides quantitative and sensitive measurements for graphene characterization. By using Raman spectrum, number of graphene layers, defects and edge arrangement of graphene can be determined^{83,84}. In Raman spectroscopy measurements, intense monochromatic light is produced by laser to illuminates specimen and when a light interact with material, inelastic (Rayleigh) or elastic (Raman) light scattering occur⁸⁵. In inelastic scattering, frequency of a few amounts of incoming photons may alter, after scattering. This shift is generally associated with vibration frequency of the molecule and it results from absorption or emission energy from the molecule^{86,87}.

There are two main peaks, G and 2D, in carbon based materials. Single and multi-layer graphene are distinguished according to their intensities and shape of the peaks. In single layer graphene, sharp and narrow 2D peak which appears at around 2700 cm^{-1} is more intense than G peak which is 1580 cm^{-1} and this situation vice versa in graphite⁸³. In addition, D peak arises at 1350 cm^{-1} when there are defects on the film⁸³. Furthermore, Raman mapping gives information about uniformity of graphene over film surface. Last but not the least, Raman spectrum of monolayer graphene can be well distinguished also intensity ratio of I_{2D}/I_G . If this ratio is equal or bigger than 2, it refers to presence of single layer graphene while I_{2D}/I_G decreases with increasing number of graphene layer⁸⁸.

AFM is another quantitative method for graphene characterization which provides exact thickness of films even though it is slightly slow when it is compared to Raman spectroscopy and optical microscope. Even though interplanar spacing of graphene film is 0.34 nm , thickness of graphene is measured by AFM greater than this value due to species like nitrogen, oxygen, or water molecule between graphene layer and SiO_2 surface in air⁸⁹.

Figure 5.4 shows characterization results of graphene sheets produced via mechanical exfoliation method. It is clearly seen from optical microscope image, region marked as 1 is single layer graphene while region 2 is multilayer graphene sheet (Figure 5.4 (a)). During this study, Raman spectroscopy revealed these results. Raman spectrum and mapping are taken from Renishaw inVia Reflex Raman Microscope and Spectrometer with 532 nm laser excitation. Finally, Figure 5.4 (d) shows AFM (supplied by NanoMagnetics Instruments Ltd) measurements of the single layer graphene. As it is expected, thickness of graphene sheet is more than 0.34 nm since measurement is performed in air condition. Scanning is employed by AFM tapping mode with $5 \mu/s$.

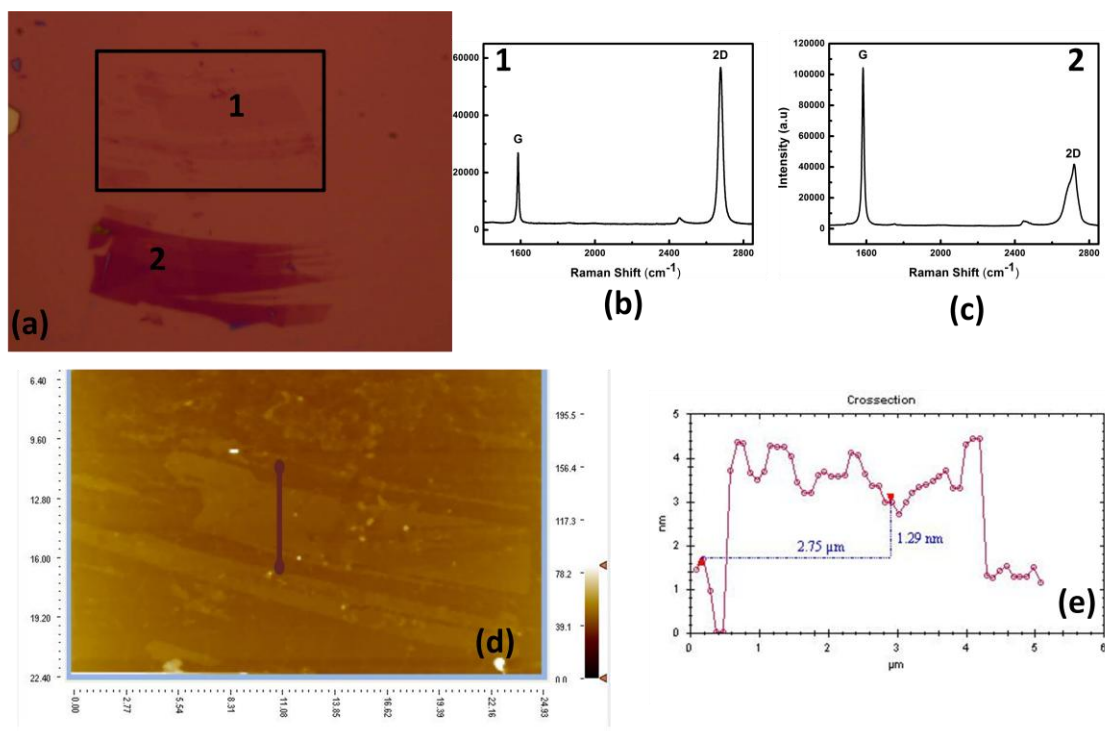


Figure 5.4: (a) Optical microscope image of graphene sheets produced via mechanical exfoliation method. Raman spectrum of (b) single and (c) multi layer graphene film. (d) AFM topography of single layer graphene sheet.

5.5 Graphene Hall Sensor

5.5.1 Fabrication of GHP

Throughout this work, graphene produced by both mechanical exfoliation and CVD growth method are used for fabrication of graphene Hall sensor. In the earlier stage of this study, mechanical exfoliated graphene is used for device fabrication. Optical microscope images of each step are given in Figure 5.5. Process flow of fabrication as follows:

1. Once graphene to be fabricated is determined, pattern consists of contact pads and markers are defined for EBL step by implementing image reversal photolithography and lift-off process (Figure 5.5(a)).
2. The sample is spin-coated with 950 K PMMA-C2 at 6,000 rpm (45 s) and baked at 180° C for 5 minutes before HSQ coating as protective layer. Because, it is difficult to remove HSQ from graphene surface after e-beam and oxygen plasma process. HSQ is baked with two steps: first, it is baked at 150° C for 2 min subsequently, at 220° C for 5 min.
3. The sample exposed to 300 $\mu\text{C}/\text{cm}^2$ dose at 30 kV for Hall cross definition by using NPGS system and exposed sample is developed with AZ 726 MIF for 70 s.
4. PMMA and graphene layers are etched by oxygen plasma and the sample is dipped in ACE to remove both HSQ and PMMA layers.
5. Metal pads between graphene Hall cross and contact pads are defined by EBL and metal evaporation (3nm Cr/ 30 nm Au).
6. Mesa of the sensor is patterned by positive photolithography and etched by SF_6/O_2 plasma.

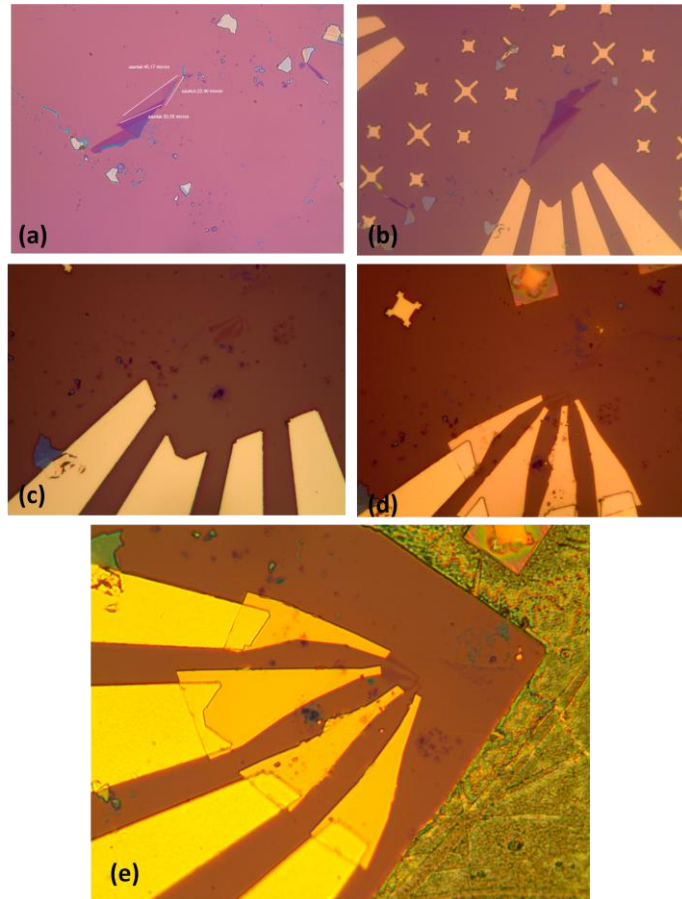


Figure 5.5: The optical microscope images of (a) mechanical exfoliated graphene (b) after contact pad metallization, (c) O₂ plasma etching of graphene (d) taking contact from graphene to contact pads by implementing EBL and (e) mesa step formation.

Although graphene produced by mechanical cleavage method has superior electronic properties than CVD growth graphene, in each time only one sensor can be manufactured due to small sized graphene flake. Fabrication yield was increased by using large area graphene. For this purpose, Graphene Hall probes have been fabricated using commercially available 1×1 cm CVD single layer graphene on 285 nm SiO₂/Si wafers supplied by Graphene Supermarket. Approximately, 50 individual chips were successfully fabricated by using this size of graphene covered substrate. Fabrication process flow is described as following:

1. Fabrication starts with positive photolithography in order to define Hall cross patterns which were protected by photoresist (Figure 5.6 (a)). This was followed by oxygen gas plasma RIE (20 sccm O₂ flow, in a 100 W

RIE power, 37.5 mTorr, for 9 s) in order to etch the unprotected parts of CVD-graphene sheet. Next, the sample is immersed into ACE to remove photoresist. Figure 5.6 (b) presents patterned graphene.

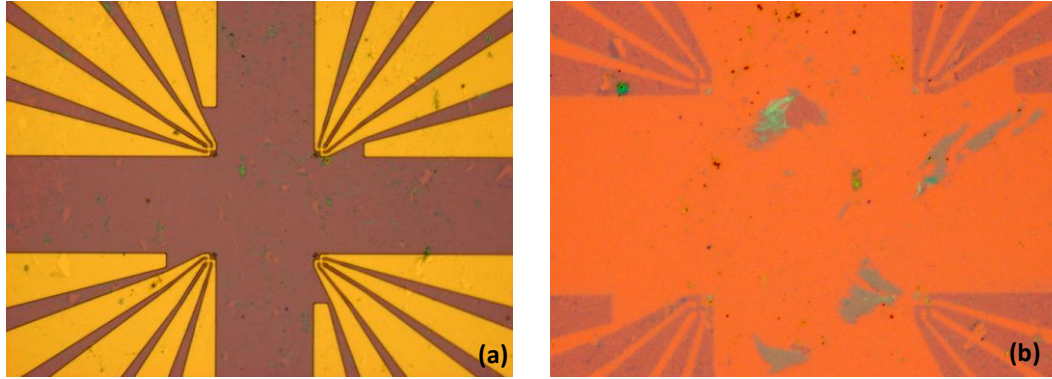


Figure 5.6: The optical microscope images of after (a) Hall cross definition by implementing positive photolithography and (b) after O₂ plasma process and removing photoresist.

2. Entire surface of purchased 1 cm × 1 cm substrate is covered by graphene. Although it is an advantage for high yield fabrication, it can cause adhesion problem after metal evaporation. To prevent this, mask pattern normally utilized for recess etch process is used in order to etch graphene region to be used for wire bonding process. Optical microscope image of the developed sample with AZ 726MIF after positive photolithography by using recess mask pattern is given in Figure 5.7 (a). This step plays crucial role in bonding. Because, if organic residue left under metal structure, it can cause peeling off contact pads from the surface during wire bonding step.
3. Optical lithography was used to pattern for contact pads on graphene, and it was followed by thermal evaporation of 10 nm Cr/200 nm Au evaporation and lift-off (Figure 5.7 (b)).

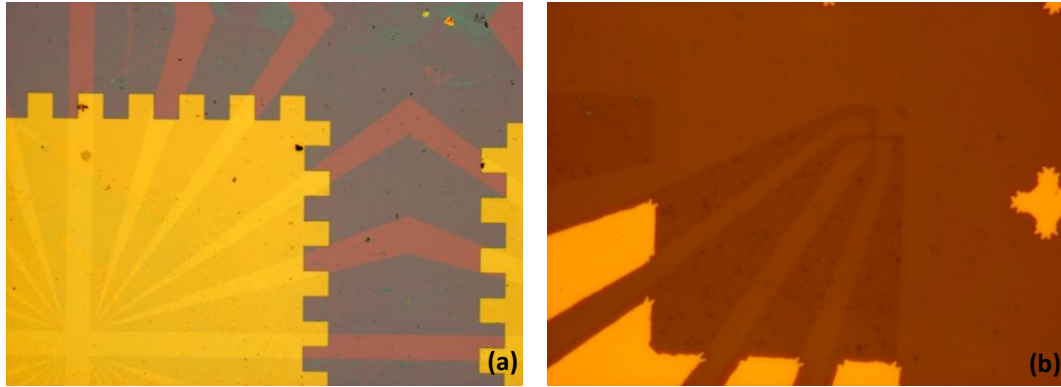


Figure 5.7: The optical microscope images (a) of the developed sample with AZ 726MIF after positive photolithography by using recess mask pattern (b) after contact pads metallization.

4. The mesa which serves as AFM tip was obtained by etching SiO_2/Si wafer ~ 830 nm in an inductively coupled plasma reactive ion etching (ICP–RIE) system (Figure 5.8 (a)). The dry etching parameters are given in previous chapter.
5. GHP patterns on the wafer were diced into individual chips and glued with low temperature epoxy on one of the tines of the QTF which is used as a force sensor in a wide temperature range. Next, QTF was glued to the ceramic plate on non–magnetic PCB and electrical connections of GHP to PCB were established with $25\ \mu\text{m}$ gold wires using wedge wire bonder (Figure 5.8 (b)).

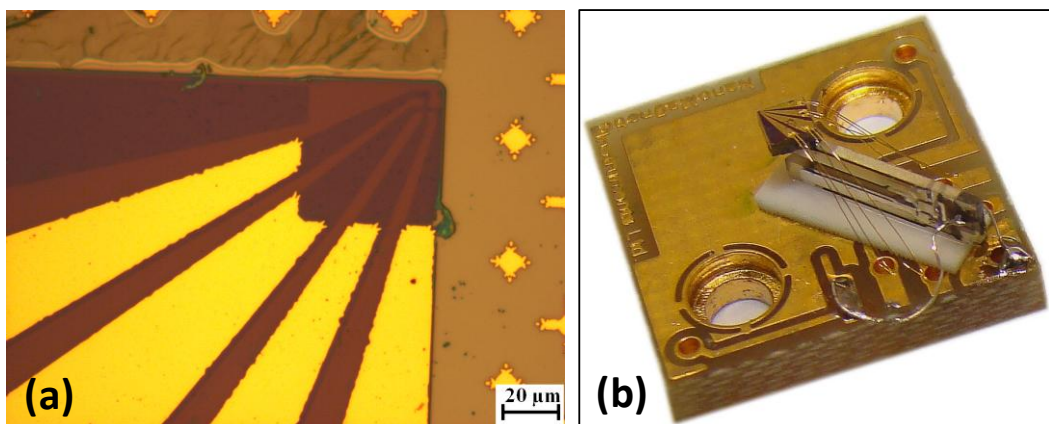


Figure 5.8: Optical microscope images of GHP. (a) After mesa formation by etching 830 nm SiO₂/Si layer. (b) Side view of Hall sensor glued on 1 × 1 cm PCB.

5.5.2 Characterization of GHP

Optical microscope is the simplest and quickest way for graphene characterization. It is particularly important for mechanical exfoliated graphene as scanning graphene sheet is initially done with it. Nowadays, it is very reliable tool which distinguish mono and multilayer graphene accurately for all production methods. Optical microscope is almost used in each step of Hall sensor fabrication from CVD growth graphene film to understand how process proceeds. On the other hand, Raman spectrum which provides obtaining quantitative measurements determines the number of graphene layers and uniformity of graphene thickness over the GHP surface. Before the fabrication we have checked graphene substrate not only by using optical microscope but also Raman spectrum (Figure 5.9). After fabrication is completed Raman spectrum of the center of Hall Cross which is shown on bottom right of Figure 5.10 verifies that the GHP was fabricated from single layer graphene and the left of this figure shows optical microscope image of fabricated sensor. Moreover, it was reported that $I_{2D}/I_G \geq 2$ is associated with the presence of monolayer graphene⁹⁰. In top right of Figure 5.10, large scale (14×14 μm) Raman map of intensity ratio gives further evidence.

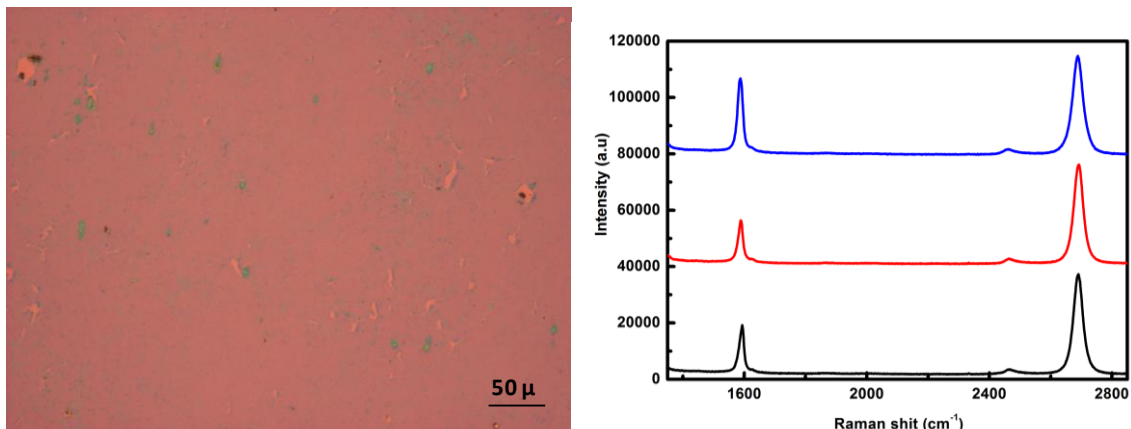


Figure 5.9: (a) The optical microscope images of as received CVD growth graphene on 285 nm SiO₂/Si wafers. (b) The Raman spectrum of as received CVD growth graphene from different three points.

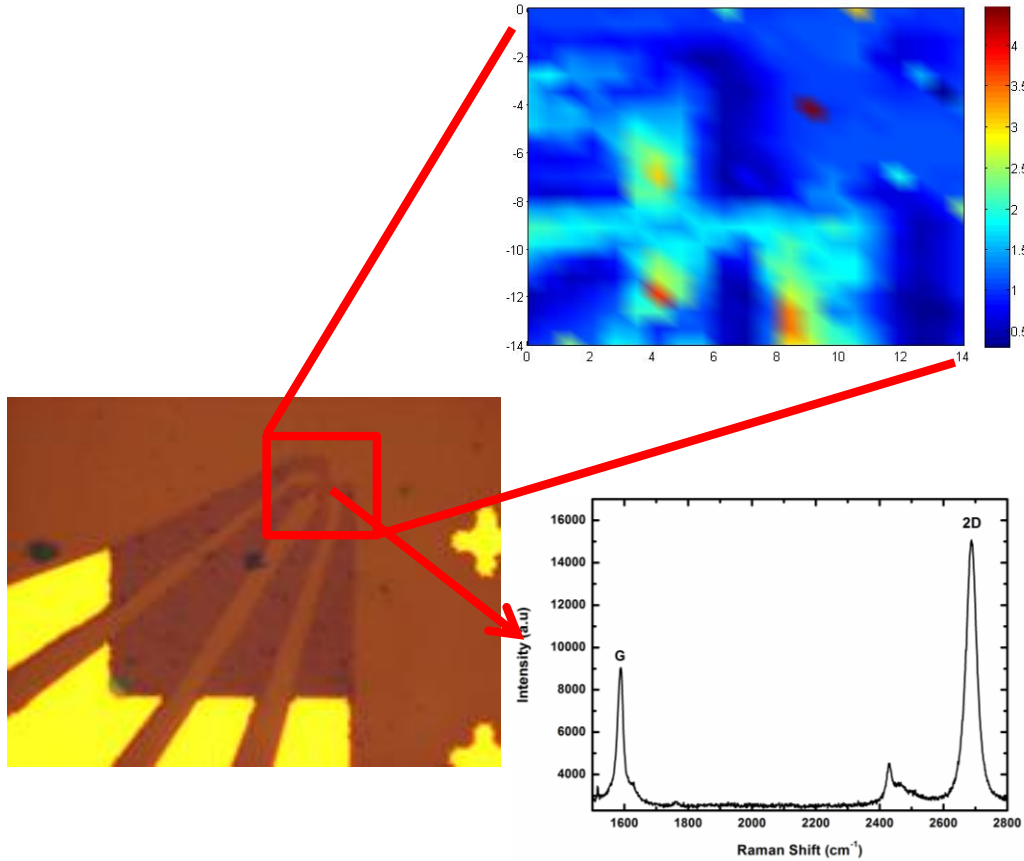


Figure 5.10: Optical microscope image of GHP (left). Raman map of ($I_{2D}/I_G \geq 2$) intensity ratio measured in a $14 \mu\text{m} \times 14 \mu\text{m}$ area of GHP (right-top). Single Raman spectrum taken from center of the GHP (right-bottom).

Electrical and magnetic characterization of GHP was performed in Helium exchange gas and vacuum conditions by using LT-SHPM initially at room temperature. Graphene exhibits p-type behavior due to environmental effects and water absorption when it is exposed to air and resist residues from fabrication process^{91, 92, 93, 94}. This results in a high charge carrier density and low Hall coefficient. Thereby, we tried to overcome this problem by performing magnetic imaging and characterization in vacuum condition as we did not have a back gate contact. Most of the experimental data for electrical characterization is performed in NanoMagnetics Instruments Ltd by using cryostat supplied by Cryogenic Limited. All experimental results, which will be

presented following parts, belong to a specific GHP which has been utilized for magnetic imaging. A uniform external magnetic field (B_{ext}) was applied to GHP up to 5,000 G and the generated Hall voltage (V_{Hall}) was simultaneously measured under constant driving current. Figure 5.11 shows the linear relationship between V_{Hall} and B_{ext} for a 2 μA driving current at room temperature.

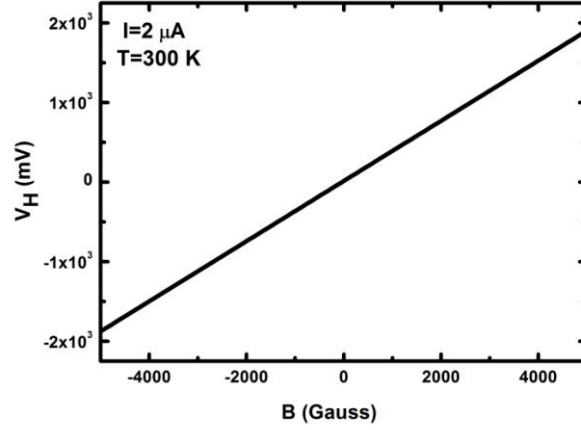


Figure 5.11: Hall voltage response of GHP to applied magnetic field at room temperature.

Room temperature series resistance and Hall coefficient of GHP were measured to be 82.20 k Ω and 0.18 Ω/G respectively in vacuum condition for 3 μA drive current. A spectrum analyzer was used to obtain a noise spectrum of the single layer graphene Hall probe. We determined minimum detectable magnetic field (B_{min}) from voltage noise spectrum, which is defined as equation:

$$B_{\text{min}} = \frac{V_{\text{Noise}}}{R_H I_H G} \quad (5.2)$$

where V_{Noise} , R_H , I_H and G are the total measured voltage noise, Hall coefficient, Hall current, and Hall probe pre-amplifier gain respectively⁹⁵. The Hall probe pre-amplifier gain was 1001 for the system used in this experiment. Figure 5 (a) represents B_{min} as a function of frequency for different Hall currents in zero magnetic field and zero back gate voltage⁹⁶.

$$V_n = \sqrt{4k_B T R_s \Delta f} \quad (5.3)$$

In this equation, k_B is Boltzmann's constant, T is temperature, R_s is the resistance of the sensor and Δf is measurement bandwidth⁹⁶.

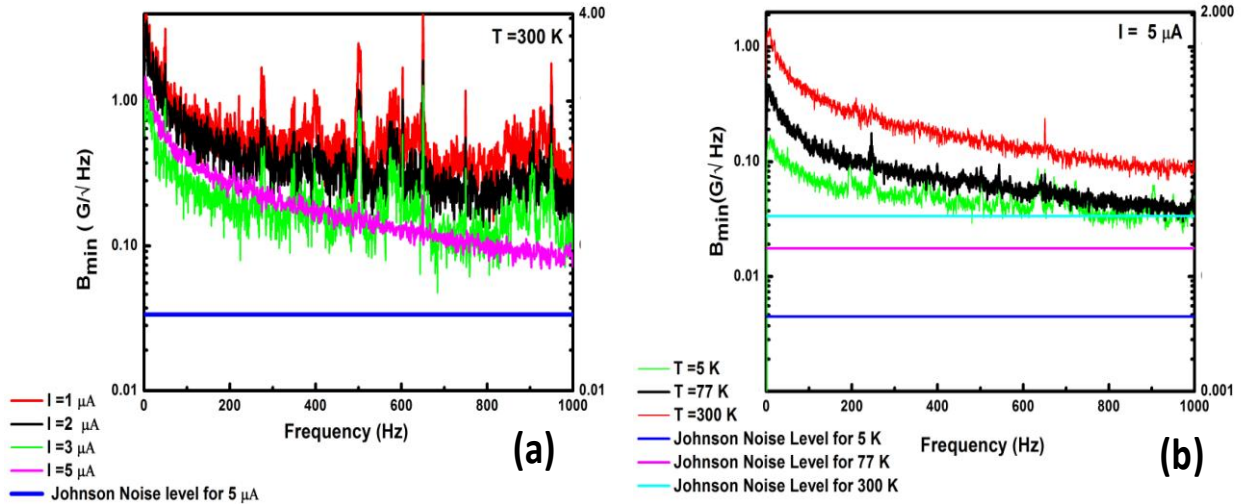


Figure 5.12: (a) B_{min} for different drive current as a function of frequency at 300 K. (b) B_{min} for different temperature as a function of frequency for $5\ \mu\text{A}$ Hall current

The graphs in Figure 5.13 (a), (b) and (c) compare the B_{min} in vacuum and in exchange gas (He) for different current values. As seen from these graphs, for $1\ \mu\text{A}$ and $2\ \mu\text{A}$ current values, B_{min} is slightly better than in exchange gas condition whereas B_{min} for $3\ \mu\text{A}$ driving current in vacuum condition can detect clearly smaller magnetic field which provides better magnetic field resolution. Temperature characterization of GHP is performed in exchange gas by Teslatron PT cryostat located in SUNUM. The variation of serial resistance of two arms of Hall crosses as a function of temperature has been shown in Figure 5.13 (d). As seen from this figure, resistance is decreasing with increasing temperature. This result is consistent with previous work⁹⁷.

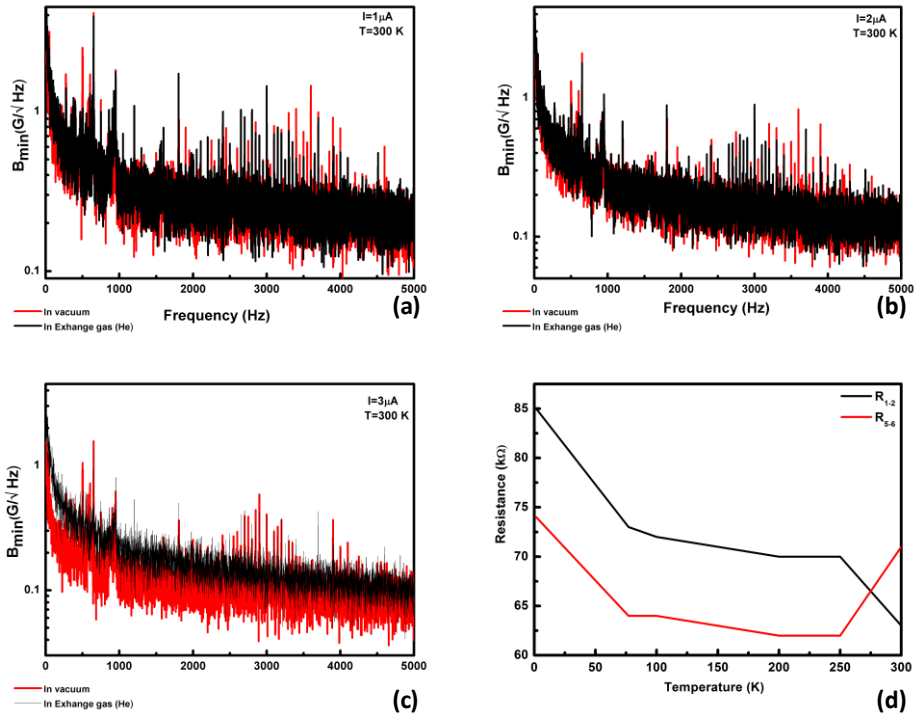


Figure 5.13: Comparison of B_{\min} in vacuum and in Helium exchange gas for different current values. (d) Serial resistance of two arms of Hall crosses as a function of temperature.

Temperature dependency of RH is also investigated. For this purpose, 2 T external magnetic fields and $\pm 2\ \mu\text{A}$ driving current are applied to GHP in exchange gas. Generated V_{Hall} out is measured by SPM electronic unit and software. RH is calculated for different temperature ranging from 1.5 K to 300K. As is seen from graphs in Figure 5.14, R_{Hall} is slightly increased by increasing temperature. After 100 K it is almost constant with increasing temperature and current with positive polarity cause obtaining slightly higher R_{Hall} .

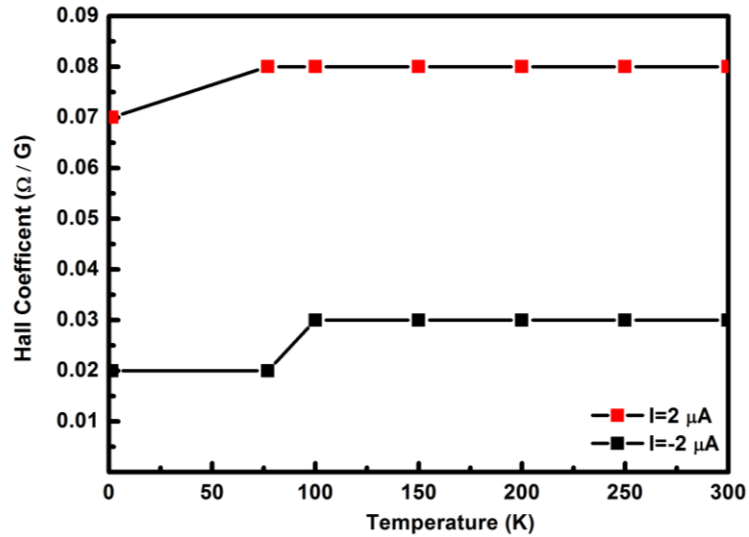


Figure 5.14: The variations of R_{Hall} as a function of temperature for $\pm 2 \mu\text{A}$ driving current.

5.5.2 Imaging NdFeB Demagnetized Magnet by GHP

We operated a LT-SHPM system manufactured by NanoMagnetics Instruments Ltd. in AFM tracking mode, in order to acquire topography and magnetic image of a NdFeB demagnetized magnet surface in a wide range of temperature (3–300K). Resonance frequency of QTF used in this experiment was around 31.9 kHz when one prong is free and the other is fixed to the ceramic plate on top of sensor holder PCB. After GHP was glued on top of QTF, this resonance frequency decreased to approximately 17 kHz due to mass of chip and glue (Figure 516).

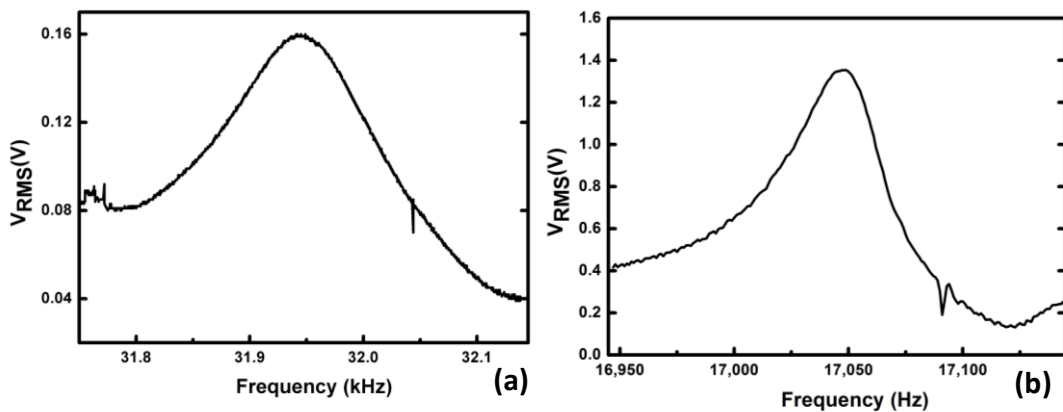


Figure 5.15: Measured resonance frequency at 300 K (a) before and (b) after GHP was glued on QTF.

The sample is tilted $\sim 1^\circ$ with respect to GHP to ensure that the corner of Hall sensor mesa is the closest point to the sample surface, which is used as an AFM tip. The sample was brought in to close proximity of GHP by means of slip-stick coarse approach mechanism. The tip-sample interaction results in a shift in resonance frequency of the QTF which is measured by a PLL for AFM feedback⁴⁵. Figures 5.16 (a) and (c) show the SHPM images of magnetic domains of NdFeB demagnetized magnet at room temperature. The magnetic field variations along a horizontal line of these images are also shown in Figure 5.16 (b) and (d). The scan parameters are 5 $\mu\text{m}/\text{s}$ scan speed, 50 $\mu\text{m} \times 50 \mu\text{m}$ scan area (Figure 5.16 (a)) and 40 $\mu\text{m} \times 40 \mu\text{m}$ scan area (Figure 5.16 (c)), 512 pixels \times 512 pixels resolution and 2 μA drive current for measured 0.22 Ω/G R_H .

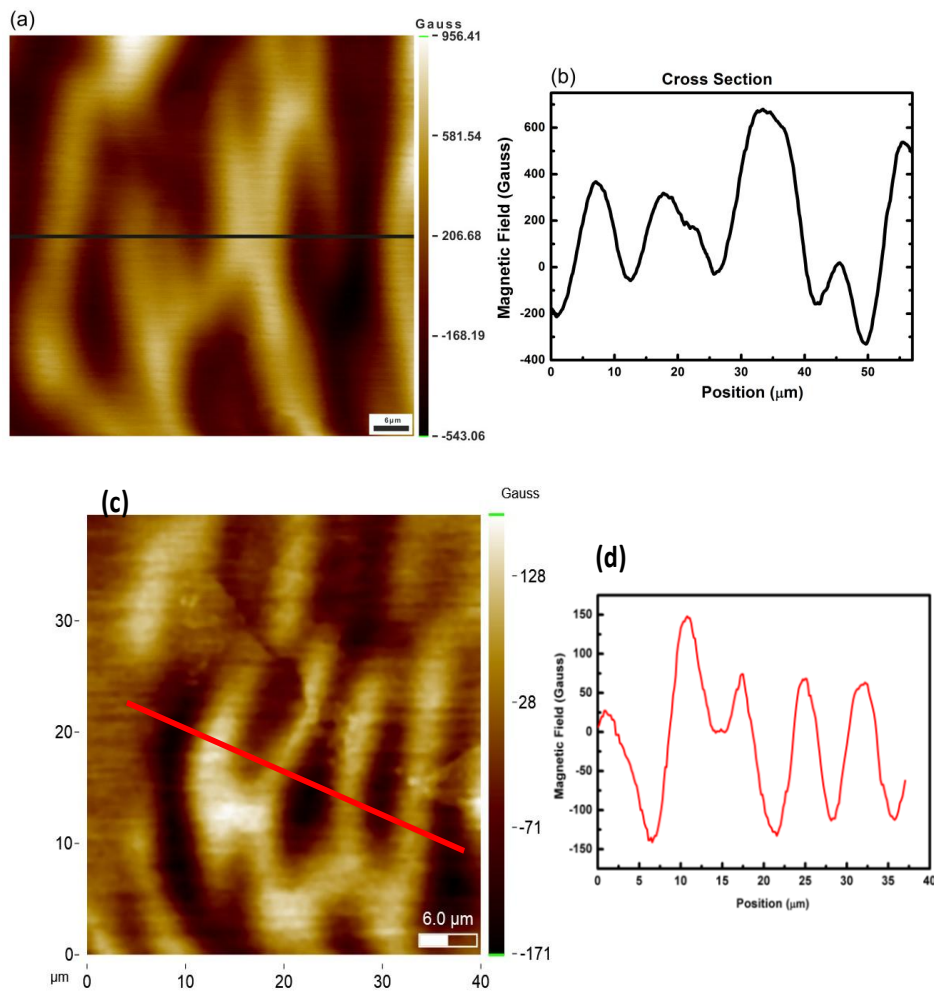


Figure 5.16: (a) and (c) magnetic images of NdFeB demagnetized magnet by using GHP at 300 K. (b) and (d) magnetic field variations along the line drawn on images.

We have also investigated the performance of GHP at cryogenic temperatures. Surface topography and magnetic image of NdFeB sample for $I_{\text{Hall}} = 2 \mu\text{A}$ at 126 K are shown in Figure 5.17 (a) and (b), respectively. Figure 5.17 (c) and 5.17 (d) show the SHPM image of the same sample at 3 K for $I_{\text{Hall}} = 2 \mu\text{A}$ and $I_{\text{Hall}} = -2 \mu\text{A}$.

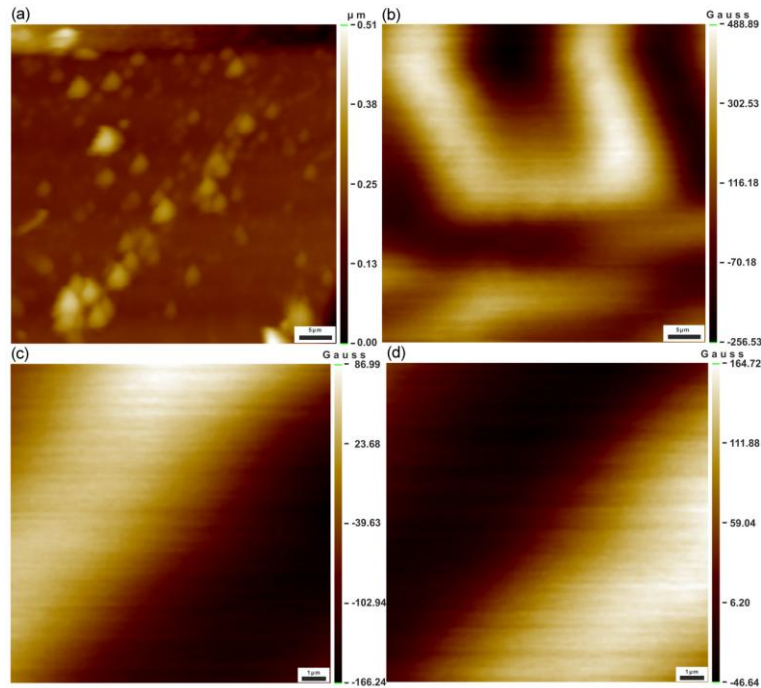


Figure 5.17: (a) Topographic image of NdFeB. (b) $50 \mu\text{m} \times 50 \mu\text{m}$ LT-SHPM magnetic image of NdFeB at 126 K. $14 \times 14 \mu\text{m}$ LT-SHPM magnetic image of the same sample for (c) $I_{\text{Hall}} = +2 \mu\text{A}$ (d) $I_{\text{Hall}} = -2 \mu\text{A}$ at 3 K.

5.6 Conclusion and Discussion

In this work, Graphene Hall sensor produced, fabricated, characterized and used for magnetic imaging. Initially, mechanical exfoliated graphene is used for fabrication.

Because not only has it high mobility, but also it is very easy to produce. Even though mechanically exfoliated graphene provides superior properties than CVD in terms of both mechanically and electronically, fabrication yield is very low with this method. We manufacture a few of Hall sensors produced via mechanical cleavage method. Due to the contact problems arising from several reasons (residual resist between contact pads and patterned graphene or fabrication process issues), resistance of Hall cross was measured drastically high around $M\Omega$ order. Therefore, we preferred to use CVD growth graphene which provides large scale graphene film and high yield production.

Raman spectroscopy and optical microscopy is used for characterization of the sensor during manufacturing process. Raman spectrum results show as received CVD samples are graphene monolayer. However, on the surface of the graphene film (without employing any process) there are discontinuities and bilayer or multilayer graphene islands. White areas in SEM image of as received CVD graphene sheet show cracks on the films (Figure 5.18). Submicron sized cracks cannot be seen in optical microscope which cause electrical contact problem. Another problem is that there are a lot of Bismuth or multilayer graphene islands which is marked as red circles in the same figure. These multilayer graphene regions result from impurities on copper metal which act as nucleation sites⁹⁸. Since activation energy is higher on impurities, carbon atoms dissolve more on these regions and cause forming multilayer graphene regions⁹⁹.

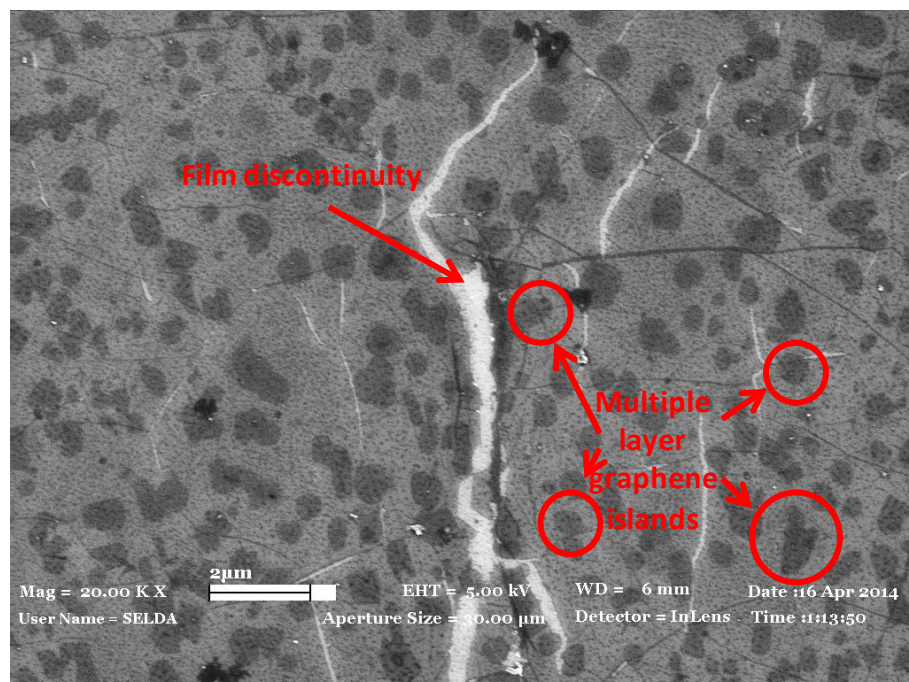


Figure 5.18: SEM image of as received CVD graphene sheet which shows cracks and discontinuity on the graphene film surface.

Once fabrication is completed, electrical characterization for different condition is done by using the SHPM. Voltage noise spectrum which limits B_{\min} is measured by spectrum analyzer. Effect of temperature and driving current on B_{\min} is investigated. According to magnetic flux noise spectrum results B_{\min} decreases with increasing drive current and it is found to be $0.20 \text{ G}/\sqrt{\text{Hz}}$ for a $3 \mu\text{A}$ drive current at 1 kHz (Figure 5.12 (a)). We also measured the magnetic field noise of GHP at 5 K, 77 K and 300 K for $I_H=5 \mu\text{A}$ and calculated Johnson noise levels for each temperature for the same current value. Smaller magnetic fields can be detected at lower temperatures by GHP, as shown in Figure 5.12 (b). Furthermore, serial resistances of Hall sensor change between 60–80 k Ω depending on temperature.

We have successfully used the Graphene Hall Probes for magnetic imaging in 3–300 K range for the first time in SHPM. This study has demonstrated that graphene is an alternative material to be used for magnetic imaging. Additionally, it is also possible to decrease Hall cross dimensions to a few tens of nanometer by employing electron beam lithography, so that spatial resolution of the sensor can potentially reach sub–100 nm resolution. Currently, we are working on the improvement of our results by reducing Hall cross area and removing residues arising from the fabrication process for both higher magnetic field and spatial resolution.

CHAPTER 6

BISMUTH HALL SENSOR for SHPM

6.1 Introduction

As a pentavalent metal, Bismuth has attracted much attention of researchers in sensing applications due to its remarkable electrical properties arising from its anisotropic Fermi level in surface, relatively large mean free path in the order of microns and small effective mass^{100, 101, 102}. The exact equal number of free electrons and holes on the surface, along with a low scattering rate gives rise to the magnetoresistance, which is known to be very high in semi–metals¹⁰³. In addition to its electrical and magnetic properties, Bismuth has an extremely low melting point of 271.3° C and its thermal conductivity is one of the lowest among the metals¹⁰⁴.

The most important element of an SHPM is the Hall sensor that is sensitive to perpendicular component of the magnetic field on surface of sample. This part can be fabricated by various materials. However, to achieve a high magnetic resolution, materials with high carrier mobility and low carrier density are preferred to help maximize the Hall coefficient and signal to noise ratio. On the other hand, size of the active area is the key factor that determines spatial resolution of microscope². As being a semimetal with a concentration of five orders of magnitude lower than metals and with negligible surface charge depletion effect, Bismuth is an alternative material for Hall probe in the area of magnetic field sensing elements⁹.

The first study of Bismuth thin film as Hall sensor was carried out by Broom *et al.* in 1962 where they scanned 1,000 or 2,000 Å thick 15 mm x15 mm superconducting thin and lead films using 100 µm Hall cross. By placing the probe 0.05 mm away from film surfaces, a current of 2 mA was applied through the probe producing a Hall voltage

of $0.6 \mu\text{V}/\text{G}$ at liquid Helium temperatures. The thermal noise was measured as $\pm 0.1 \text{ G}$ and the resolutions were 0.2 and 0.25 mm , respectively ¹⁰⁵.

The smallest fabricated Bismuth hall probe so far was reported in 2004 by Sandhu *et al.*, where nano-sized Bismuth sensor was used in a room temperature SHPM, and images of magnetic domains of low coercivity garnet thin film samples were recorded ⁹. This $50 \times 50 \text{ nm}$ nano-Bismuth hall probe fabricated by optical lithography and focused ion beam milling were 60 nm in thickness and was located about $4 \mu\text{m}$ away from the tip yielded a noise level of $0.85 \text{ G}/\sqrt{\text{Hz}}$. The logic behind employing FIB technique in here was to assure thicker hall crosses that allowed lower resistance values and hence less Johnson noise. Room temperature Hall coefficients of nano-Bismuth hall probes were measured as $4.0 \times 10^{-4} \Omega/\text{G}$. Feasibility of nano-Bismuth hall probes were tested on a 5 mm thick crystalline Bismuth substituted iron garnet thin film. Images were obtained with a drive current of $43 \mu\text{A}$ and at a tilt angle of 1.2° by measuring the changes in Hall voltages coming from stray magnetic fields. The SEM image of fabricate Hall sensor and magnetic imaging of iron garnet thin film taken by fabricated 50 nm Bismuth Hall sensor at room temperature are given in Figure 6.1.

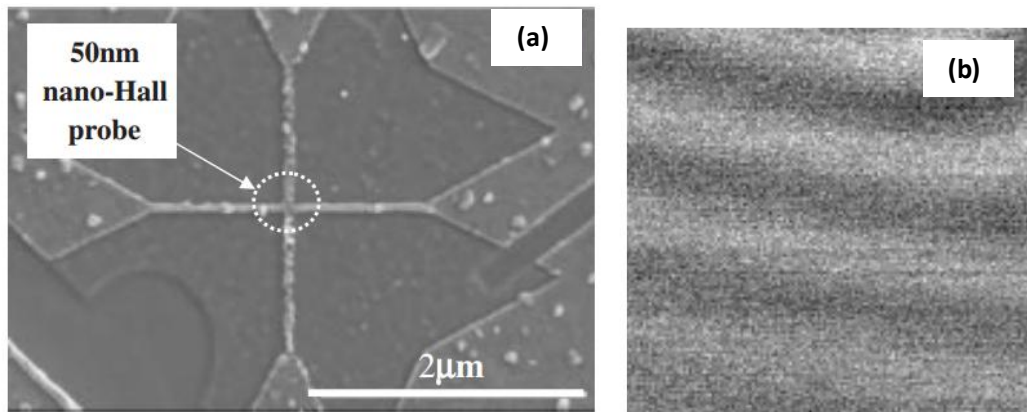


Figure 6.1: The SEM images of $50 \text{ nm} \times 50 \text{ nm}$ nano-Bismuth hall probe. SHPM image of crystalline Bismuth substituted iron garnet thin film taken by fabricated 50 nm Bismuth Hall sensor at room temperature.

By considering the studies mentioned above, the scope of this chapter is to enhance the spatial resolution of SHPM images by employing Bismuth hall sensors and

to observe its behavior at low temperatures. In this context, present chapter describes optimized fabrication process of Bismuth Hall sensor for SHPM applications in detail by covering all the fabrication steps, problems raised throughout the process and solutions developed. We have fabricated Hall crosses in three different sizes of 100 nm, 200 nm and 500 nm, respectively. Along with imaging of NdFeB demagnetized magnet using these sensors, temperature characterization was also carried out. Since the spatial resolution is directly proportional to cross size, we reduced the size of the probe fabricated was to 100 nm and gathered successful images at 300 K. To our knowledge, this study was the first reported imaging at low temperature using Bismuth hall sensor.

6.2 Bismuth Hall Sensor

6.2.1 Fabrication of Bismuth Hall Sensor

Two different optical mask pattern designs are used in the fabrication of Bismuth Hall sensors. One of them has $30\ \mu\text{m} \times 50\ \mu\text{m}$ active area with asymmetric contact pads whereas the other design has $10\ \mu\text{m} \times 10\ \mu\text{m}$ areas with symmetrically ordered pads (Figure 6.2). To reduce area shortens exposing time while EBL is employed. It is particularly important when NPGS system is used since it works with low current values.

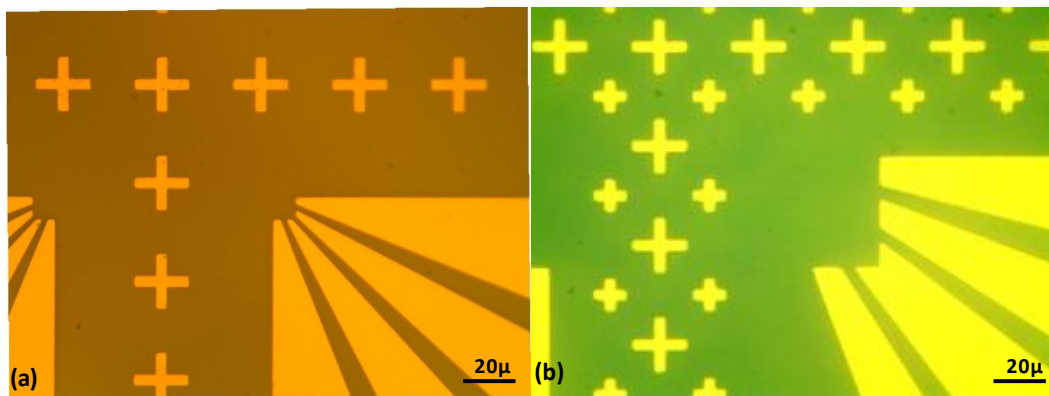


Figure 6.2: The optical microscope image of (a) symmetric (b) asymmetric ohmic contacts after 10 nm Cr and 100 nm Au evaporation and lift-off process.

Many problems have been encountered during fabrication process of Bismuth Hall sensor. Some of them with their solutions are discussed previously in Chapter 5. Optimized process recipe is given as following:

1. Fabrication of Bismuth Hall sensor starts with wafer cutting into 1.2 cm × 1.2 cm pieces. Then, pieces are cleaned by standard cleaning procedure as mentioned previous chapter.
2. After spin coating with AZ 5214E (4,000 rpm for 40 s), the sample is baked 105 ° C for 1 minute. Positive optical lithography is implemented by using recess etch mask with zigzag shapes for 2 s illumination by using Midas mask aligner. Then, the sample is developed with AZ 726 MIF and washed by DI water. Hard bake is done at 120 ° C for 2 minutes on a hot plate and the sample is etched in HCl:H₂O₂:H₂O solution at volume ratios of 4:7:55 for 90 s which provides around 1.5 μm etch thickness (Figure 4.12).
3. Contact pads are defined by image reversal recipe. First, the sample is spun at 6,000 rpm for 45 s. Then, it is baked at 90 ° C for 2 minutes (prebake). The sample is illuminated for 2 s by Midas mask aligner and post bake is done at 115° C for 2 minutes on a hot plate. Flood exposure (without mask) is employed for 11.6 s and the sample is developed with AZ 726 MIF for 25 s. Next, 10 nm Cr and 100 nm Au layer is evaporated by spin coater and lift off process is performed by immersing the sample in ACE solution (Figure 6.2).
4. Once contact pads are defined, oxygen plasma etching is performed to the samples in order to etch resist residue left from optical lithography steps. The oxygen plasma parameters are 20 sccm O₂ flow, in a 100 W RIE power, 37.5 mTorr pressure for 5 minutes. Then, bi-layer resist recipe is used (First layer is coated with 495 K PMMA-C2 at 5,000 rpm for 50 s and baked at 180 ° C for 40 minutes. The second layer is spun with 950 K PMMA-A2 at 4,000 rpm 50 and placed on a hot plate at 180 ° C for 40 minutes.) Patterns are designed by AutoCAD program and inserted in

Layout BEAMER to convert this design file into a readable format in Vistec machine and utilize from PEC function of this program. $500\mu\text{C}/\text{cm}^2$ base dose is used to obtain 50 nm Hall cross size (Hall cross area is exposed with $800\mu\text{C}/\text{cm}^2$) where specimen current is 180 pA beam current and step size and resolution are 1 nm. Development is done 1:3 MIBK:IPA solution for 60 s. After the sample is lifted-off and 3 nm chromium and 30 nm Bismuth are thermally evaporated. Figure 6.3 shows SEM images of 50 nm Bismuth Hall cross at different magnifications by using this recipe.

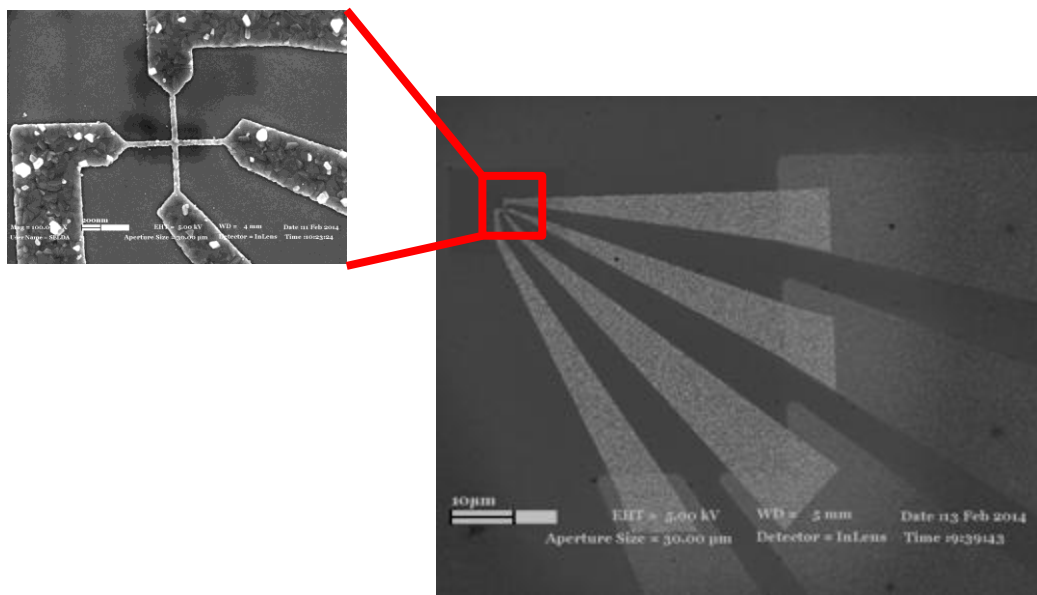


Figure 6.3: Then SEM images of 50 nm Bismuth Hall cross at different magnifications.

5. After Hall cross definition, the sample is characterized by SEM and successfully patterned elements are determined and their resistance are measured by multimeter in the probe station. Patterns that are in a magnitude of a few $\text{k}\Omega$ resistances are selected as suitable candidates for Hall sensor application. However, we sometimes measure drastically high resistance values around $\text{M}\Omega$ scale even though SEM images suggest that Hall cross area are successfully lifted-off. It has been realized that there occurs a gap between Au contact pads and legs of Bismuth Hall cross. As a solution, we apply a second EBL process in order to assure that there is a full contact. Further EBL processes can be required until contact problem

is completely resolved. Figure 6.4 (a) shows optical microscope images after the first time EBL is employed for connection problem (b), (c) and (d) show SEM images after third EBL process applied at different magnifications and different points of view.

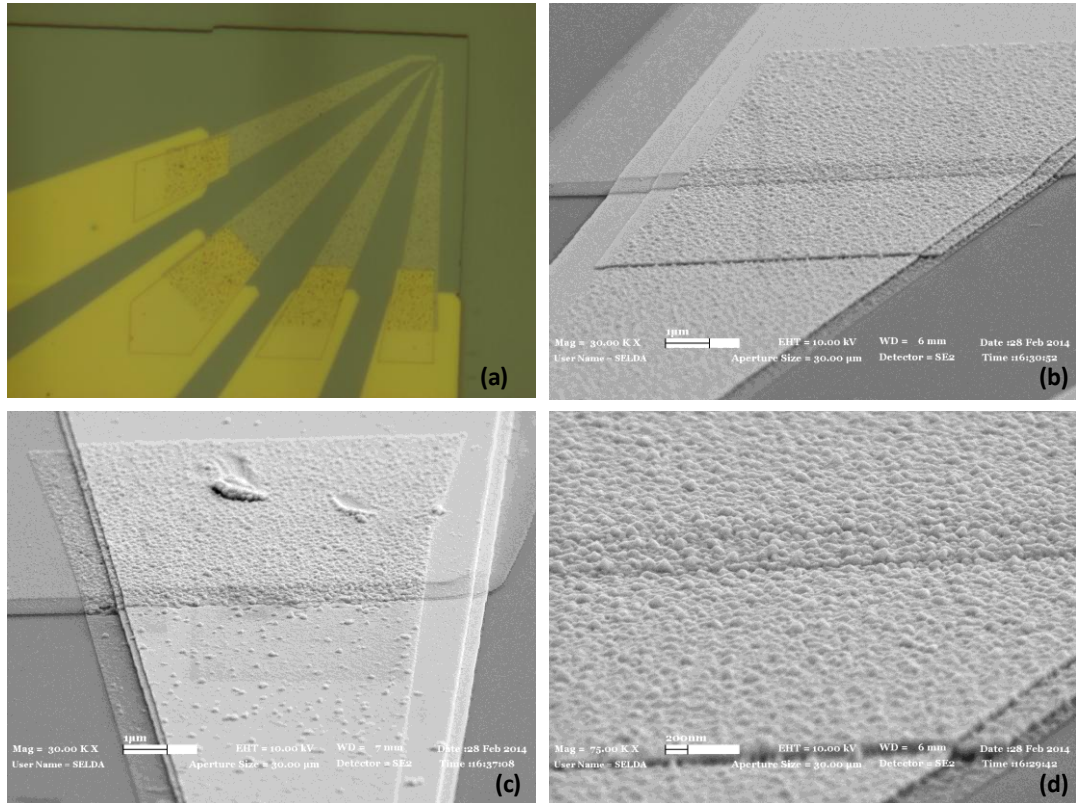


Figure 6.4: (a) The optical microscope images after the first time EBL is employed for connection problem (b), (c) and (d) show SEM images after third EBL process applied at different magnifications and different points of view.

1. For mesa step formation, the sample is spun with 950 K PMMA–A2 and its copolymer MMA (8.5) EL11. Then, EBL is employed with $550 \mu\text{C}/\text{cm}^2$ base dose. Development is performed with 1:3 MIBK:IPA solution for 60 s and post bake is done at 100°C on a hot plate. Etching solution is prepared with $\text{H}_2\text{S}_4\text{O}_4:\text{H}_2\text{O}_2:\text{H}_2\text{O}$ at volume ratios of 1:8:40 for 60 s. by using this recipe around $1.5 \mu\text{m}$ etch thickness is obtained successfully (Figure 6.5).

- The sample is diced by Disco dicer and glued on top of QTF which has been already attached to PCB. Finally electrical connection is taken by wedge bonding process with 25 μm gold wire.

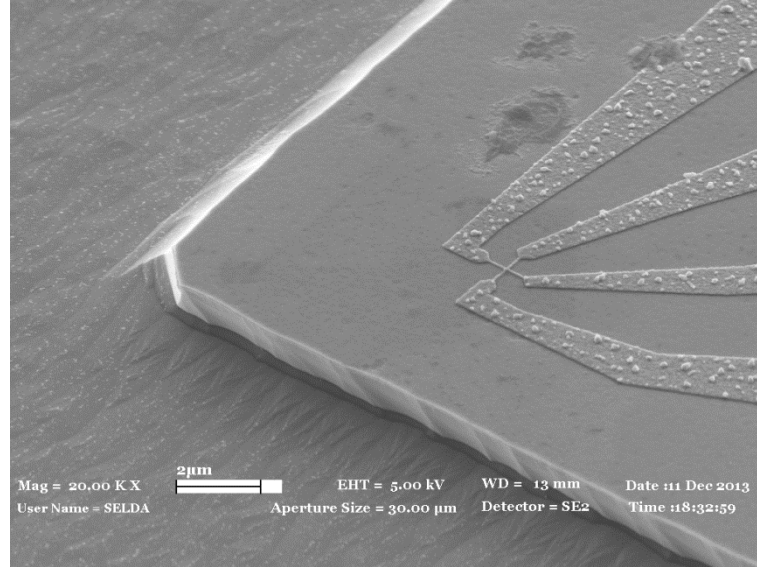


Figure 6.5: The SEM images of 50 nm Bismuth Hall sensor after mesa formation.

6.2.2 Characterization of Bismuth Hall Sensor

We carried out electrical characterization of Bismuth Hall probes with different sized (200 nm and 500 nm) at various temperatures and driving current. The SEM image of fabricated 500 nm Bismuth Hall sensor is given in Figure 6.6 (a). Room temperature serial resistance and R_H of 500 nm Bismuth Hall sensor are measured as 18.8 k Ω and 3.2×10^{-4} Ω/G respectively. Noise spectrum of fabricated sensors are measured by spectrum analyzer and converted into magnetic field unit in order to determine B_{\min} at different conditions. Figure 6.6 (b), (c) and (d) compare B_{\min} as a function of frequency for different driving currents at 300 K, 77 K and 4 K temperature respectively. The graphs in Figure 6.6 show that B_{\min} decreases as driving current is increased for each temperature. This is correlated with theory since B_{\min} is inversely proportional with driving current as is shown equation 5.2. Same trend is observed for 200 nm Bismuth Hall sensor by means of relation between B_{\min} and drive current (Figure 6.7). Room temperature serial resistance and R_H of 200 nm Bismuth Hall sensor are measured as 13.8 k Ω and 4.2×10^{-4} Ω/G respectively.

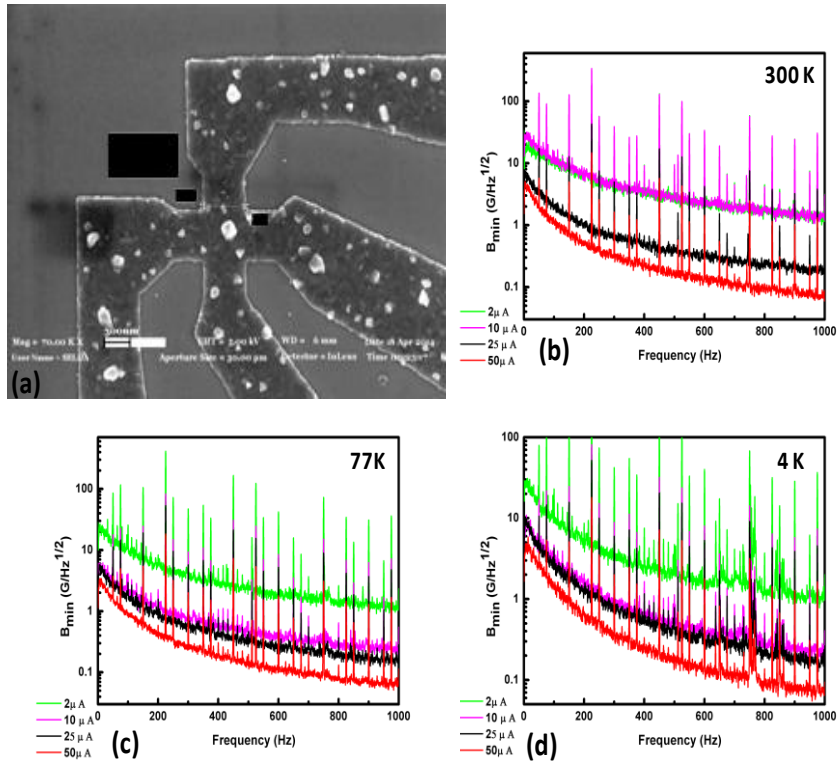


Figure 6.6: (a) The SEM image of 500 nm Bismuth Hall sensor. B_{\min} as a function of driving current at different temperature values (b) 300 K (c) 77 K and (d) 4 K.

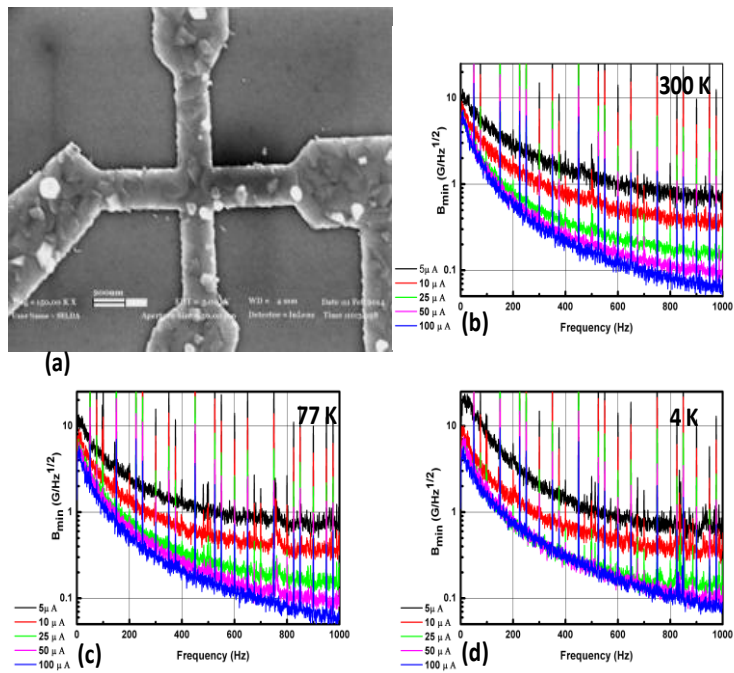


Figure 6.7: (a) The SEM image of 200 nm Bismuth Hall sensor. B_{\min} as a function of driving current at different temperature values (b) 300 K (c) 77 K and (d) 4 K.

6.2.3 Imaging NdFeB Demagnetized Magnet by Bismuth Hall Sensor

NdFeB demagnetized magnet is scanned with 500 nm, 200 and 100 nm Bismuth Hall sensors at different temperatures by using QTF AFM feed-back mode. For this purpose, fabricated Hall sensor is attached to the microscope and NdFeB is tilted around 1° with respect to Hall sensor in order to use mesa corner as AFM tip. Figure 6.8 shows SHPM images of NdFeB demagnetized magnet at 300 K, 77 K and 4 K for 50 μ A acquired by using 500 nm Bismuth Hall sensor. Resonance frequency and quality factor of QTF are measured as 10,170 Hz and 80 at room temperature. Δf is set to 10 Hz during scan. The scan areas of images are 30 μ m \times 30 μ m for 300 K and 77 K whereas it is set to 20 μ m \times 20 μ m for 4 K.

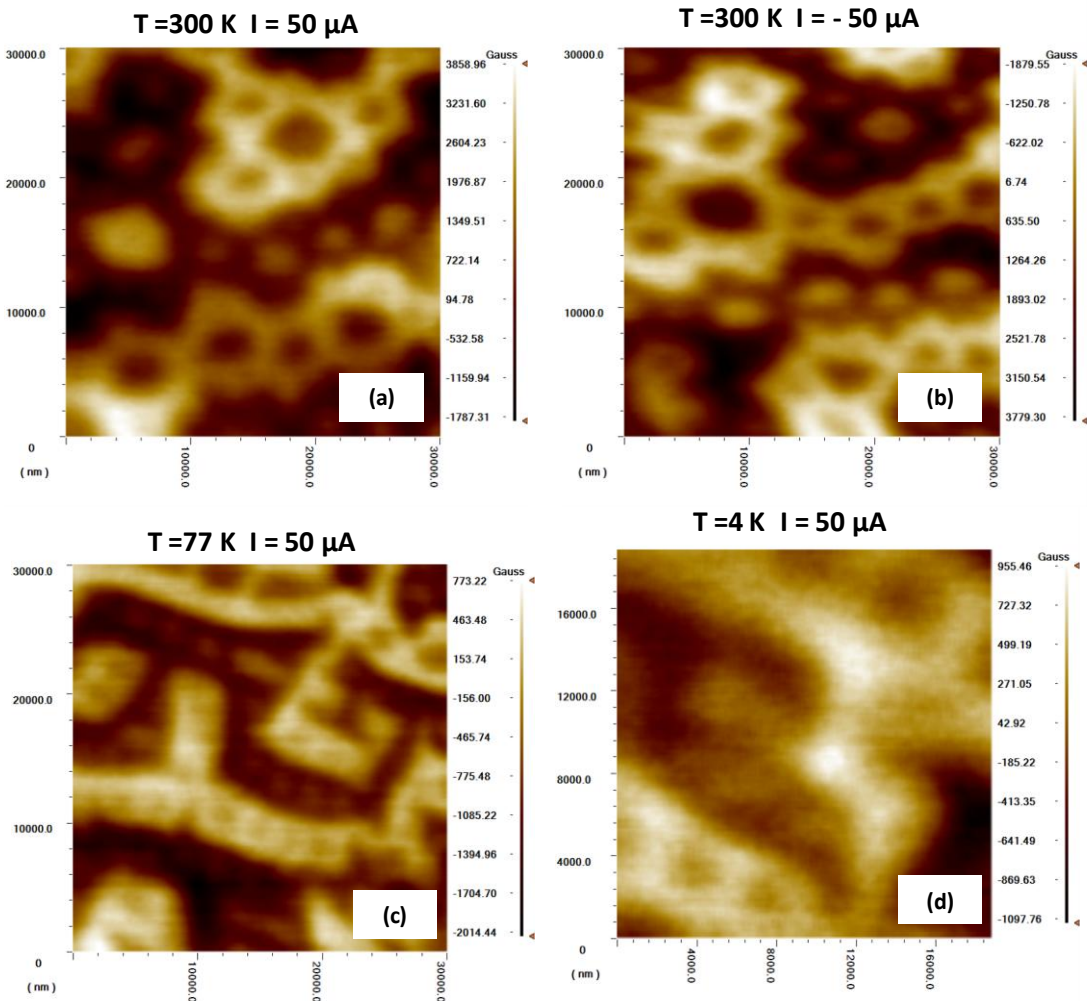


Figure 6.8: SHPM images of NdFeB demagnetized magnet at (a) 300 K, (b) 77 K, (c) 4 K taken by using 500nm Bismuth Hall sensor for 50 μ A driving current and at (d) 4 K for -50μ A driving current.

Figure 6.9 shows magnetic image and cross sections taken from the same image of NdFeB demagnetized magnetic sample at room temperature by using Bismuth Hall sensor with 200 nm cross sized. The sample is tilted 1.25° in this scan and room temperature serial resistance of the sensor is measured as 13.86 k Ω . Topography and SHPM image ($30 \mu\text{m} \times 30 \mu\text{m}$ scan area) of NdFeB sample at 77 K are given in Figure 6.10.

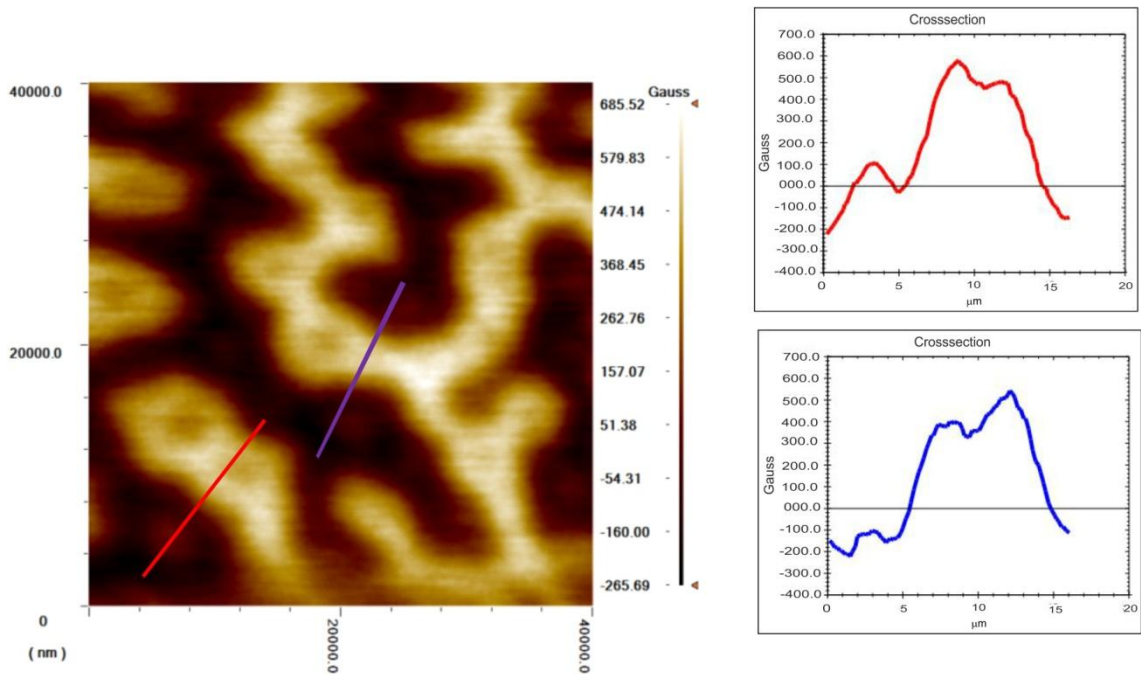


Figure 6.9: SHPM images of Nd,FeB demagnetized magnet at 300 K (left) by using 200 nm Bismuth Hall sensor for 500 μ A drive current and graph of cross sections (right top and bottom).

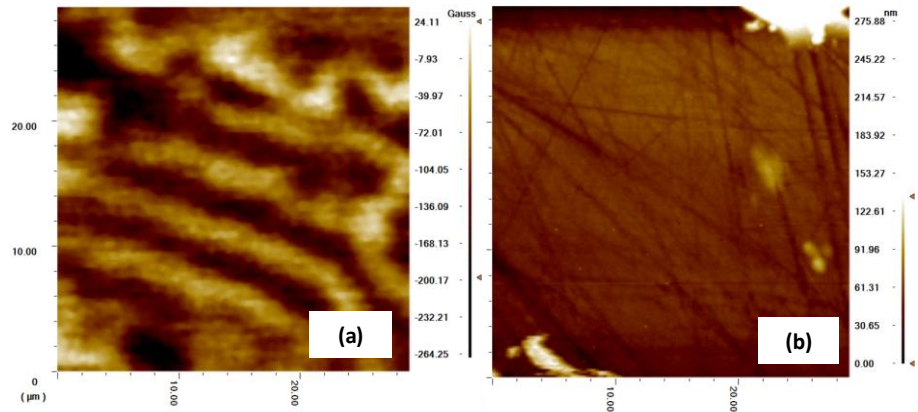


Figure 6.10: (a) Topography and (b) SHPM image of NdFeB sample at 77 K by using 200 nm Bismuth Hall sensor for 500 μ A drive current.

Magnetic image of NdFeB with scan area 20 μ m \times 20 μ m at 4 K is also obtained by using 200 nm Bismuth Hall sensor (Figure 6.11). Serial resistance of the probe at 4 K is measured as 13.86 k Ω .

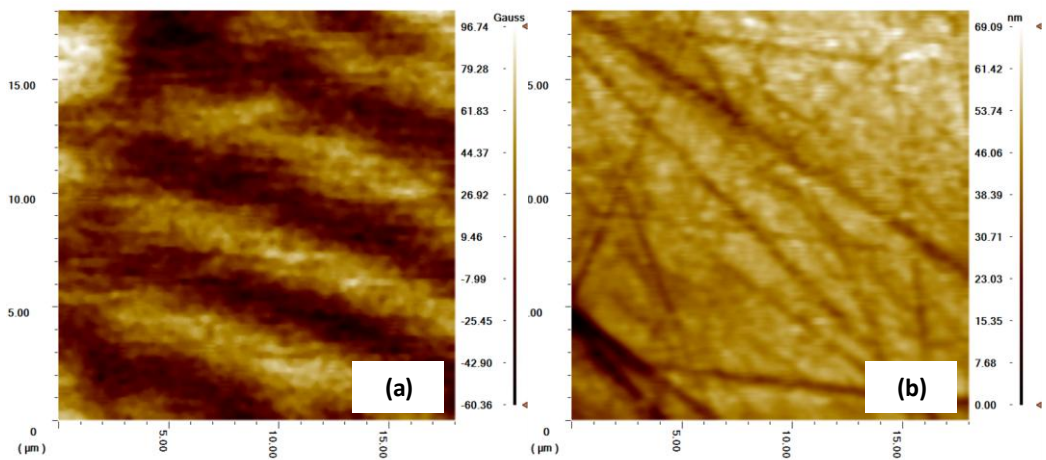


Figure 6.11: (a) Topography and (b) SHPM image of NdFeB sample at 4 K by using 200 nm Bismuth Hall sensor for 500 μ A drive current.

Finally, fabricated 100 nm Bismuth Hall sensor which has 13.86 k Ω series resistance are used for magnetic imaging of NdFeB demagnetized magnet at room temperature (Figure 6.12).

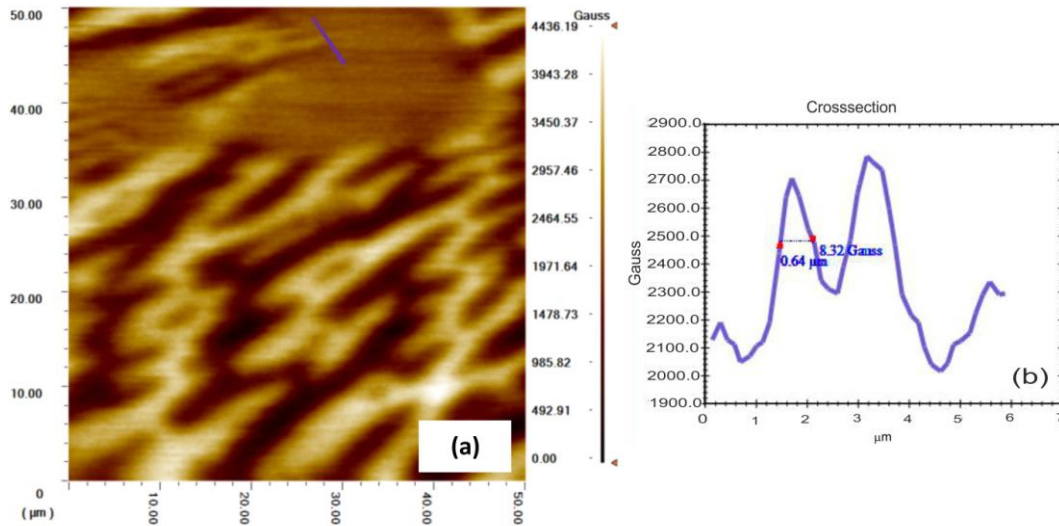


Figure 6.12: (a) SHPM image of NdFeB sample at 300 K by using 100 nm Bismuth Hall sensor for 500 μA drive current.(b) Magnetic field variations along the line drawn on images.

5.2 Conclusion

In this chapter, fabrication, electrical characterization and temperature dependency of Bismuth Hall sensor is explained in detail. Hall crosses with 100 nm, 200 nm and 500 nm in sizes were fabricated and SHPM images of NdFeB demagnetized magnet were recorded using these sensors with QTF AFM feedback mode. B_{\min} as a function of frequency is deduced from voltage noise spectrum for different temperatures and various driving currents. The smallest Hall sensor used in SHPM was 100 nm. We could obtain magnetic imaging with this Hall sensor only at room temperature.

CHAPTER 7

CONCLUSION AND FUTURE WORK

There are two novel outcomes of this thesis. The first one is that GHP was used in SHPM application for the first time. Although GHP is very well characterized in the literature in terms of its electrical properties, our study has moved graphene a step further in its applications. To achieve this, we fabricated GHP by implementing conventional lithographic techniques. Temperature dependence of electrical characteristics was determined and an increasing trend in B_{\min} is observed with increasing temperature and decreasing driving current. R_H of GHP was measured as $0.18 \Omega/\text{G}$ for $3 \mu\text{A}$ Hall current at room temperature in vacuum, whereas B_{\min} was found to be $0.20 \text{ G}/\sqrt{\text{Hz}}$ at 1 kHz. These results show that graphene has become a promising candidate as Hall sensor material in SHPM application. We have fabricated GHP by using graphene produced by two different methods; mechanical exfoliation and CVD growth. However, due to contact problems arising from fabrication process, we could not obtain expected results using exfoliated graphene. By using CVD graphene we could overcome this problem. Although CVD graphene increased the sensor production yield, the noise levels in the sensors were relatively high, as the CVD graphene is polycrystalline. Electrical properties can be further improved by using large flake, single crystal graphene with minimal defects. To retain better electrical properties of CVD graphene, one can use CVD graphene growth on platinum and transferred by bubbling transfer method.

We have also fabricated Bismuth nano Hall sensors by EBL and lift-off process and imaged NdFeB demagnetized magnet at wide range temperature range 4–300K. – During the fabrication of Bismuth Hall sensor, in spite of many difficulties in

fabrication process, we were successful to fabricate the devices down to 100 nm by using advanced lithographic techniques and obtained SHPM images. By using EBL, we were able to reduce Hall cross size down nanometer scale which resulted in obtaining better spatial resolution of SHPM images. It might be possible to produce Hall probes with less than 25 nm sizes by using EBL, which might allow obtaining images with higher spatial resolution.

BIBLIOGRAPHY

- 1 G. Binning, H. Rohrer, C. Gerber, and E. Weibel, "Surface Studies by Scanning Tunneling Microscopy," *Phys Rev Lett* **49** (1), 57-61 (1982).
- 2 A. Oral, M. Kaval, M. Dede, H. Masuda, A. Okamoto, I. Shibasaki, and A. Sandhu, "Room-temperature scanning Hall probe microscope (RT-SHPM) imaging of garnet films using new high-performance InSb sensors," *Ieee T Magn* **38** (5), 2438-2440 (2002).
- 3 M. Dede, Doctoral Dissertation, Bilkent University, 2008.
- 4 R. Akram, M. Dede, and A. Oral, "Imaging capability of pseudomorphic high electron mobility transistors, AlGaIn/GaN, and Si micro-Hall probes for scanning Hall probe microscopy between 25 and 125 degrees C," *J Vac Sci Technol B* **27** (2), 1006-1010 (2009).
- 5 A. Sandhu, H. Masuda, A. Oral, and S. J. Bending, "Direct magnetic imaging of ferromagnetic domain structures by room temperature scanning hall probe microscopy using a bismuth micro-hall probe," *Jpn J Appl Phys* **2** **40** (5B), L524-L527 (2001).
- 6 A. K. Geim and K. S. Novoselov, "The rise of graphene," *Nat Mater* **6** (3), 183-191 (2007).
- 7 V. Panchal, K. Cedergren, R. Yakimova, A. Tzalenchuk, S. Kubatkin, and O. Kazakova, "Small epitaxial graphene devices for magnetosensing applications," *J Appl Phys* **111** (7) (2012).
- 8 A. Sandhu, H. Masuda, K. Kurosawa, A. Oral, and S. J. Bending, "Bismuth nano-Hall probes fabricated by focused ion beam milling for direct magnetic imaging by room temperature scanning Hall probe microscopy," *Electron Lett* **37** (22), 1335-1336 (2001).
- 9 A. Sandhu, K. Kurosawa, M. Dede, and A. Oral, "50 nm Hall sensors for room temperature scanning Hall probe microscopy," *Jpn J Appl Phys* **1** **43** (2), 777-778 (2004).
- 10 H. A. Mohammed and S. J. Bending, "Fabrication of nanoscale Bi Hall sensors by lift-off techniques for applications in scanning probe microscopy," *Semicond Sci Tech* **29** (8) (2014).
- 11 A.F.J. Levi, *Applied Quantum Mechanics*. (Cambridge University Press, 2012).
- 12 K. Sergei and G. Alexei, *Scanning Probe Microscopy : Electrical and Electromechanical Phenomena at the Nanoscale* (Springer, 2007).
- 13 D. S. Klaus, *Handbook of Nanophysics: Principles and Methods*. (CRC Press, 2010).

- 14 G. Binnig, C. F. Quate, and C. Gerber, "Atomic Force Microscope," *Phys Rev Lett* **56** (9), 930-933 (1986).
- 15 Y. Seo and W. Jhe, "Atomic force microscopy and spectroscopy," *Rep Prog Phys* **71** (1) (2008).
- 16 X. Ning and L. King, *Nano Optoelectronic Sensors and Devices: Nanophotonics from Design to Manufacturing* (William Andrew, 2011).
- 17 H. Peter, *Advances in Imaging and Electron Physics*. (Academic Press, 2003).
- 18 L. Luan, Doctoral Dissertation, Stanford University, 2011.
- 19 P. Grutter, T. Jung, H. Heinzelmann, A. Wadas, E. Meyer, H. R. Hidber, and H. J. Guntherodt, "10-Nm Resolution by Magnetic Force Microscopy on Fendb," *J Appl Phys* **67** (3), 1437-1441 (1990).
- 20 G. Han, Y. H. Wu, and Y. K. Zheng, "Dual-synthetic magnetic force microscopy tip and its imaging performance," *J Magn Magn Mater* **315** (1), 46-52 (2007).
- 21 Ü. Koray, The Master of Science, Bilkent University, 2005.
- 22 S. J. Bending, "Local magnetic probes of superconductors," *Advances in Physics* **48** (4), 449-535 (1999).
- 23 S. Morita, *Roadmap of Scanning Probe Microscopy*. (Springer, 2007).
- 24 "<http://www.nanomagnetics-inst.com/tr>".
- 25 A. Sandhu, H. Masuda, A. Oral, and S. J. Bending, "Room temperature sub-micron magnetic imaging by scanning Hall probe microscopy," *Jpn J Appl Phys* **1** **40** (6B), 4321-4324 (2001).
- 26 B. Aktaş, L. Tagirov, and F. Mikailov, *Magnetic Nanostructures*. (Springer, 2007).
- 27 S. Mouaziz, G. Boero, R. S. Popovic, and J. Brugger, "Polymer-Based Cantilevers With Integrated Electrodes," *J. Microelectromech. Syst* **15** (4), 890-895 (2006).
- 28 T. Schweinbock, D. Weiss, M. Lipinski, and K. Eberl, "Scanning Hall probe microscopy with shear force distance control," *J Appl Phys* **87** (9), 6496-6498 (2000).
- 29 A. J. Brook, S. J. Bending, J. Pinto, A. Oral, D. Ritchie, H. Beere, M. Henini, and A. Springthorpe, "Integrated piezoresistive sensors for atomic force-guided scanning Hall probe microscopy," *Appl Phys Lett* **82** (20), 3538-3540 (2003).

- 30 B. K. Chong, H. Zhou, G. Mills, L. Donaldson, and J. M. R. Weaver, "Scanning Hall probe microscopy on an atomic force microscope tip," *J Vac Sci Technol A* **19** (4), 1769-1772 (2001).
- 31 A. J. Brook, S. J. Bending, J. Pinto, A. Oral, D. Ritchie, H. Beere, A. Springthorpe, and M. Henini, "Micromachined III-V cantilevers for AFM-tracking scanning hall probe microscopy," *Journal of Micromechanics and Microengineering* **13** (1), 124-128 (2003).
- 32 J. Curie and P. Curie, "Development, via compression, of electric polarization in hemihedral crystals with inclined faces," *Bull. Soc. minéral. Fr* **3** (90), 383-386 (1880).
- 33 M. Shahinpoor and H. J. Schneider, *Intelligent Materials*. (Royal Society of Chemistry, Cambridge, 2008).
- 34 V. Medved, *Measurement of Human Locomotion*. (CRC Press, 2000).
- 35 A. A. Kosterev, F. K. Tittel, D. V. Serebryakov, A. L. Malinovsky, and I. V. Morozov, "Applications of quartz tuning forks in spectroscopic gas sensing," *Rev Sci Instrum* **76** (4) (2005).
- 36 P. Gunther, U. Fischer, and K. Dransfeld, "Scanning near-Field Acoustic Microscopy," *Applied Physics B-Photophysics and Laser Chemistry* **48** (1), 89-92 (1989).
- 37 K. Karrai and R. D. Grober, "Piezoelectric Tip-Sample Distance Control for near-Field Optical Microscopes," *Appl Phys Lett* **66** (14), 1842-1844 (1995).
- 38 M. Todorovic and S. Schultz, "Magnetic force microscopy using nonoptical piezoelectric quartz tuning fork detection design with applications to magnetic recording studies," *J Appl Phys* **83** (11), 6229-6231 (1998).
- 39 F. D. Callaghan, X. Yu, and C. J. Mellor, "Variable temperature magnetic force microscopy with piezoelectric quartz tuning forks as probes optimized using Q-control," *Appl Phys Lett* **87** (21) (2005).
- 40 F. J. Giessibl, "High-speed force sensor for force microscopy and profilometry utilizing a quartz tuning fork," *Appl Phys Lett* **73** (26), 3956-3958 (1998).
- 41 F. J. Giessibl, "Atomic resolution on Si(111)-(7x7) by noncontact atomic force microscopy with a force sensor based on a quartz tuning fork," *Appl Phys Lett* **76** (11), 1470-1472 (2000).
- 42 Y. Qin, Doctoral Dissertation, Purdue University, 2007.
- 43 T. Ludwig, "Casimir force experiments with quartz tuning forks and an atomic force microscope (AFM)," *Journal of Physics a-Mathematical and Theoretical* **41** (16) (2008).

- 44 R. Oria, J. Otero, L. Gonzalez, L. Botaya, M. Carmona, and M. Puig-Vidal, "Finite Element Analysis of Electrically Excited Quartz Tuning Fork Devices," *Sensors* **13** (6), 7156-7169 (2013).
- 45 R. Akram, M. Dede, and A. Oral, "Variable Temperature-Scanning Hall Probe Microscopy With GaN/AlGaN Two-Dimensional Electron Gas (2DEG) Micro Hall Sensors in 4.2-425 K Range Using Novel Quartz Tuning Fork AFM Feedback," *Ieee T Magn* **44** (11), 3255-3260 (2008).
- 46 G. E. Moore, "Cramming more components onto integrated circuits (Reprinted from *Electronics*, pg 114-117, April 19, 1965)," *P Ieee* **86** (1), 82-85 (1998).
- 47 Y. Nishi and R. Doering, *Handbook of Semiconductor Manufacturing Technology*. (CRC Press, 2007).
- 48 H.S. Nalwa, *Deposition and Processing*. (Academic Press, 2002).
- 49 Z. Zalevsky and I. Abdulhalim, *Integrated Nanophotonic Devices*. (Elsevier, 2010).
- 50 A. E. Grigorescu, M. C. van der Krogt, C. W. Hagen, and P. Kruit, "10 nm lines and spaces written in HSQ, using electron beam lithography," *Microelectron Eng* **84** (5-8), 822-824 (2007).
- 51 Z. Cui, *Nanofabrication: Principles, Capabilities and Limits* (Springer, 2010).
- 52 M. T. Moneck, Doctoral Dissertation, Carnegie Mellon University, 2008.
- 53 V. K. Varadan, K. J. Vinoy, and S. Gopalakrishnan, *Smart Material Systems and MEMS*. (WILEY, 2006).
- 54 A. Oral, S. J. Bending, and M. Henini, "Scanning Hall probe microscopy of superconductors and magnetic materials," *J Vac Sci Technol B* **14** (2), 1202-1205 (1996).
- 55 G. D. Howells, A. Oral, S. J. Bending, S. R. Andrews, P. T. Squire, P. Rice, A. de Lozanne, J. A. C. Bland, I. Kaya, and M. Henini, "Scanning Hall probe microscopy of ferromagnetic structures," *J Magn Magn Mater* **196**, 917-919 (1999).
- 56 A. Sandhu, H. Masuda, A. Oral, S. J. Bending, A. Yamada, and M. Konagai, "Room temperature scanning Hall probe microscopy using GaAs/AlGaAs and Bi micro-hall probes," *Ultramicroscopy* **91** (1-4), 97-101 (2002).
- 57 A. Sandhu, A. Okamoto, I. Shibusaki, and A. Oral, "Nano and micro Hall-effect sensors for room-temperature scanning hall probe microscopy," *Microelectron Eng* **73-4**, 524-528 (2004).
- 58 K. S. Novoselov, A. K. Geim, S. V. Morozov, D. Jiang, Y. Zhang, S. V. Dubonos, I. V. Grigorieva, and A. A. Firsov, "Electric field effect in atomically thin carbon films," *Science* **306** (5696), 666-669 (2004).

- 59 C. Berger, Z. M. Song, X. B. Li, X. S. Wu, N. Brown, C. Naud, D. Mayou, T. B. Li, J. Hass, A. N. Marchenkov, E. H. Conrad, P. N. First, and W. A. de Heer, "Electronic confinement and coherence in patterned epitaxial graphene," *Science* **312** (5777), 1191-1196 (2006).
- 60 C. C. Tang, M. Y. Li, L. J. Li, C. C. Chi, and J. C. Chen, "Characteristics of a sensitive micro-Hall probe fabricated on chemical vapor deposited graphene over the temperature range from liquid-helium to room temperature," *Appl Phys Lett* **99** (11) (2011).
- 61 S. Sonusen, O. Karci, M. Dede, S. Aksoy, and A. Oral, "Single layer graphene Hall sensors for scanning Hall probe microscopy (SHPM) in 3-300 K temperature range," *Appl Surf Sci* **308**, 414-418 (2014).
- 62 S. Das Sarma, S. Adam, E. H. Hwang, and E. Rossi, "Electronic transport in two-dimensional graphene," *Rev Mod Phys* **83** (2), 407-470 (2011).
- 63 J. Irudayaraj, *Biomedical Nanosensors*. (CRC Press, 2012).
- 64 D. Dragoman, M. Dragoman, and A. A. Muller, "Graphene - A One-Atom-Thick Material for Microwave Devices," *Rom J Inf Sci Tech* **11** (1), 29-35 (2008).
- 65 D. Dragoman and M. Dragoman, "Negative differential resistance of electrons in graphene barrier," *Appl Phys Lett* **90** (14) (2007).
- 66 Z. Liu and X. Zhou, *Graphene: Energy Storage and Conversion Applications*. (CRC Press, 2015).
- 67 Y. M. Lin, C. Dimitrakopoulos, K. A. Jenkins, D. B. Farmer, H. Y. Chiu, A. Grill, and P. Avouris, "100-GHz Transistors from Wafer-Scale Epitaxial Graphene," *Science* **327** (5966), 662-662 (2010).
- 68 K. I. Bolotin, K. J. Sikes, Z. Jiang, M. Klima, G. Fudenberg, J. Hone, P. Kim, and H. L. Stormer, "Ultrahigh electron mobility in suspended graphene," *Solid State Commun* **146** (9-10), 351-355 (2008).
- 69 K. Nagashio, T. Nishimura, K. Kita, and A. Toriumi, "Mobility Variations in Mono- and Multi-Layer Graphene Films," *Appl Phys Express* **2** (2) (2009).
- 70 C. S. S. R. Kumar, *Raman Spectroscopy for Nanomaterials Characterization*. (Springer, 2012).
- 71 E. Elhajjar, V. L. Saponara, and A. Mulaiana, *Smart Composites: Mechanics and Design*. (CRC Press, 2014).
- 72 J. C. Charlier, P. C. Eklund, J. Zhu, and A. C. Ferrari, "Electron and phonon properties of graphene: Their relationship with carbon nanotubes," *Top Appl Phys* **111**, 673-709 (2008).

- 73 I. W. Frank, D. M. Tanenbaum, A. M. Van der Zande, and P. L. McEuen, "Mechanical properties of suspended graphene sheets," *J Vac Sci Technol B* **25** (6), 2558-2561 (2007).
- 74 F. Bonaccorso, A. Lombardo, T. Hasan, Z. P. Sun, L. Colombo, and A. C. Ferrari, "Production and processing of graphene and 2d crystals," *Mater Today* **15** (12), 564-589 (2012).
- 75 J. H. Chen, C. Jang, S. D. Xiao, M. Ishigami, and M. S. Fuhrer, "Intrinsic and extrinsic performance limits of graphene devices on SiO₂," *Nat Nanotechnol* **3** (4), 206-209 (2008).
- 76 R. Munoz and C. Gomez-Aleixandre, "Review of CVD Synthesis of Graphene," *Chem Vapor Depos* **19** (10-12), 297-322 (2013).
- 77 Y. Zhang, L. Y. Zhang, and C. W. Zhou, "Review of Chemical Vapor Deposition of Graphene and Related Applications," *Accounts Chem Res* **46** (10), 2329-2339 (2013).
- 78 G. X. Ni, Y. Zheng, S. Bae, C. Y. Tan, O. Kahya, J. Wu, B. H. Hong, K. Yao, and B. Ozyilmaz, "Graphene-Ferroelectric Hybrid Structure for Flexible Transparent Electrodes," *Acs Nano* **6** (5), 3935-3942 (2012).
- 79 R. Yakimova, C. Virojanadara, D. Gogova, M. Syvajarvi, D. Siche, K. Larsson, and L. I. Johansson, "Analysis of the Formation Conditions for Large Area Epitaxial Graphene on SiC Substrates," *Silicon Carbide and Related Materials 2009, Pts 1 and 2* **645-648**, 565-568 (2010).
- 80 F. Dulot, L. Mansour, A. Leycuras, W. Wulfhekel, D. Sander, F. A. d'Avitaya, and M. Hanbucken, "Structure and morphology of concave-shaped surfaces on 6H-Si(0001) after H₂ etching," *Appl Surf Sci* **187** (3-4), 319-325 (2002).
- 81 J. Hass, W. A. de Heer, and E. H. Conrad, "The growth and morphology of epitaxial multilayer graphene," *J Phys-Condens Mat* **20** (32) (2008).
- 82 P. Blake, E. W. Hill, A. H. Castro Neto, K. S. Novoselov, D. Jiang, R. Yang, T. J. Booth, and A. K. Geim, "Making graphene visible," *Appl Phys Lett* **91** (6) (2007).
- 83 A. C. Ferrari, J. C. Meyer, V. Scardaci, C. Casiraghi, M. Lazzeri, F. Mauri, S. Piscanec, D. Jiang, K. S. Novoselov, S. Roth, and A. K. Geim, "Raman spectrum of graphene and graphene layers," *Phys Rev Lett* **97** (18) (2006).
- 84 Y. M. You, Z. H. Ni, T. Yu, and Z. X. Shen, "Edge chirality determination of graphene by Raman spectroscopy," *Appl Phys Lett* **93** (16) (2008).
- 85 F. Han, *A Modern Course in the Quantum Theory of Solids*. (World Scientific Publishing Company, 2012).
- 86 V.V. Tuchin, *Handbook of Optical Sensing of Glucose in Biological Fluids and Tissues*. (CRC Press, 2009).

- 87 J. P. Dakin and R. G. W. Brown, *Handbook of Optoelectronics*. (CRC Press, 2006).
- 88 A. A. Green and M. C. Hersam, "Solution Phase Production of Graphene with Controlled Thickness via Density Differentiation," *Nano Lett* **9** (12), 4031-4036 (2009).
- 89 M. Ishigami, J. H. Chen, W. G. Cullen, M. S. Fuhrer, and E. D. Williams, "Atomic structure of graphene on SiO₂," *Nano Lett* **7** (6), 1643-1648 (2007).
- 90 S. A. Dyakov, T. S. Perova, C. Q. Miao, Y. H. Xie, S. A. Cherevkov, and A. V. Baranov, "Influence of the buffer layer properties on the intensity of Raman scattering of graphene," *J Raman Spectrosc* **44** (6), 803-809 (2013).
- 91 O. Kazakova, T. L. Burnett, J. Patten, L. Yang, and R. Yakimova, "Epitaxial graphene on SiC(000(1)over-bar): functional electrical microscopy studies and effect of atmosphere," *Nanotechnology* **24** (21) (2013).
- 92 Z. G. Cheng, Q. Y. Zhou, C. X. Wang, Q. A. Li, C. Wang, and Y. Fang, "Toward Intrinsic Graphene Surfaces: A Systematic Study on Thermal Annealing and Wet-Chemical Treatment of SiO₂-Supported Graphene Devices," *Nano Lett* **11** (2), 767-771 (2011).
- 93 D. W. Shin, H. M. Lee, S. M. Yu, K. S. Lim, J. H. Jung, M. K. Kim, S. W. Kim, J. H. Han, R. S. Ruoff, and J. B. Yoo, "A Facile Route To Recover Intrinsic Graphene over Large Scale," *Acs Nano* **6** (9), 7781-7788 (2012).
- 94 T. T. Feng, D. Xie, Y. X. Lin, H. Tian, H. M. Zhao, T. L. Ren, and H. W. Zhu, "Unipolar to ambipolar conversion in graphene field-effect transistors," *Appl Phys Lett* **101** (25) (2012).
- 95 M. Bando, T. Ohashi, M. Dede, R. Akram, A. Oral, S. Y. Park, I. Shibusaki, H. Handa, and A. Sandhu, "High sensitivity and multifunctional micro-Hall sensors fabricated using InAlSb/InAsSb/InAlSb heterostructures," *J Appl Phys* **105** (7) (2009).
- 96 A. Oral, S. J. Bending, and M. Henini, "Real-time scanning hall probe microscopy," *Appl Phys Lett* **69** (9), 1324-1326 (1996).
- 97 V. Skakalova, A. B. Kaiser, J. S. Yoo, D. Oberfell, and S. Roth, "Correlation between resistance fluctuations and temperature dependence of conductivity in graphene," *Phys Rev B* **80** (15) (2009).
- 98 S. M. Kim, A. Hsu, Y. H. Lee, M. Dresselhaus, T. Palacios, K. K. Kim, and J. Kong, "The effect of copper pre-cleaning on graphene synthesis," *Nanotechnology* **24** (36) (2013).
- 99 W. Liu, H. Li, C. Xu, Y. Khatami, and K. Banerjee, "Synthesis of high-quality monolayer and bilayer graphene on copper using chemical vapor deposition," *Carbon* **49** (13), 4122-4130 (2011); I. Vlassiuk, P. Fulvio, H. Meyer, N. Lavrik, S. Dai, P. Datskos, and S. Smirnov, "Large scale

- atmospheric pressure chemical vapor deposition of graphene," *Carbon* **54**, 58-67 (2013).
- 100 X. Du, S. W. Tsai, D. L. Maslov, and A. F. Hebard, "Metal-insulator-like behavior in semimetallic bismuth and graphite," *Phys Rev Lett* **94** (16) (2005).
- 101 C. M. B. Hincapie, M. J. P. Cardenas, J. E. A. Orjuela, E. R. Parra, and J. J. O. Florez, "Physical-Chemical Properties of Bismuth and Bismuth Oxides: Synthesis, Characterization and Applications," *Dyna-Colombia* **79** (176), 139-148 (2012).
- 102 A. Kumar and O. P. Katyal, "Thickness Dependence of Temperature-Coefficient of Resistivity of Polycrystalline Bismuth-Films," *Appl Phys a-Mater* **52** (4), 265-267 (1991).
- 103 S. G. Bompadre, C. Biagini, D. Maslov, and A. F. Hebard, "Unambiguous determination of the g factor for holes in bismuth at high B/T," *Phys Rev B* **64** (7) (2001).
- 104 J. Puthussery, T. H. Kosel, and M. Kuno, "Facile Synthesis and Size Control of II-VI Nanowires Using Bismuth Salts," *Small* **5** (10), 1112-1116 (2009).
- 105 R. F. Broom and E. H. Rhoderick, "Studies of the Intermediate State in Thin Superconducting Films " *PROC. PHYS. SOC.* **79** (1962).